AD-A170 363 STUDIES IN HIGH CURRENT BEAM PROPAGATION AT REDUCED PRESSURES.. (U) SCIENCE APPLICATIONS INTERNATIONAL CORP LOS ALTOS CA E R PARKINSON ET AL. 31 JAN 85 1/2

UNCLASSIFIED SAIC-U-75-PA AFOSR-TR-86-0494 F/G 20/9 NL

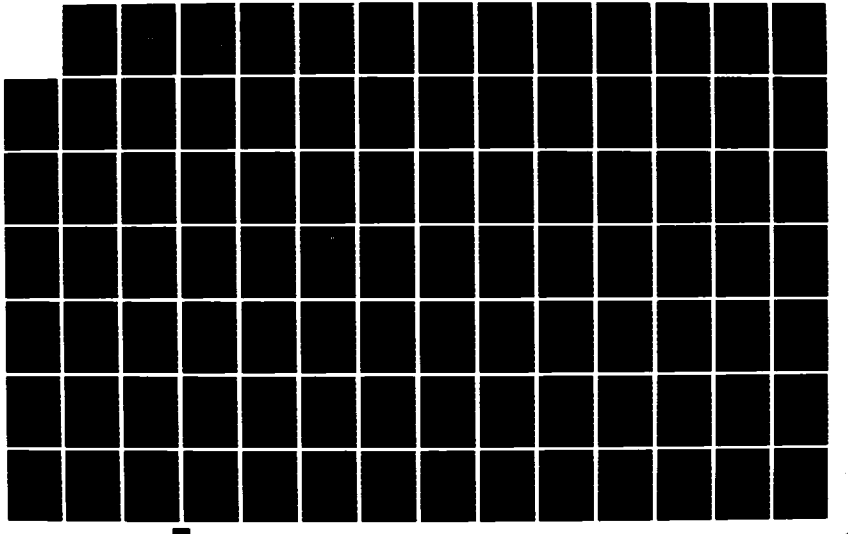

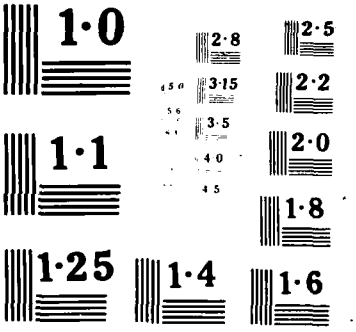
1·0
1·1
1·25
1·4
1·6
1·8
2·0
2·2
2·5
2·8
3·15
3·5
4·0
4·5
5·0
5·6

(2)

STUDIES IN HIGH CURRENT BEAM PROPAGATION AT REDUCED PRESSURES

SAIC™
Science Applications International Corporation

(2)

SAIC-U-75-PA

STUDIES IN HIGH CURRENT BEAM PROPAGATION AT REDUCED PRESSURES

31 January 1985

E.R. Parkinson
D. A. Reeley, Chief Technical Information Division

Annual Report (0002AC)

Contract F49620-81-C-0012

prepared for

Air Force Office of Scientific Research
Bolling Air Force Base
Washington, D.C. 20332

SAIC
Science Applications International Corporation

UNCLASSIFIED

SECURITY CLASSIFICATION OF THIS PAGE (When Data Entered)

REPORT DOCUMENTATION PAGE		READ INSTRUCTIONS BEFORE COMPLETING FORM
1. REPORT NUMBER AFOSR-TR- 86-0494	2. GOVT ACCESSION NO. ADA170363	3. RECIPIENT'S CATALOG NUMBER
4. TITLE (and Subtitle) STUDIES IN HIGH CURRENT BEAM PROPAGATION AT REDUCED PRESSURES		5. TYPE OF REPORT & PERIOD COVERED Annual Report 3/15/81 - 11/30/84
		6. PERFORMING ORG. REPORT NUMBER SAIC-U-75-PA
7. AUTHOR(s) E.R. Parkinson D.A. Keeley		8. CONTRACT OR GRANT NUMBER(s) F49620-81-C-0012
9. PERFORMING ORGANIZATION NAME AND ADDRESS SCIENCE APPLICATIONS INTERNATIONAL CORPORATION 5150 El Camino Real, Suite B-31 Los Altos, CA 94022		10. PROGRAM ELEMENT, PROJECT, TASK AREA & WORK UNIT NUMBERS 61103F 2301A7
11. CONTROLLING OFFICE NAME AND ADDRESS Director, Physical & Geophysical Sciences, NP Air Force Office of Scientific Research Building 410, Bolling AFB, DC 20332		12. REPORT DATE 31 January 1985
		13. NUMBER OF PAGES 115
14. MONITORING AGENCY NAME & ADDRESS(if different from Controlling Office)		15. SECURITY CLASS. (of this report) UNCLASSIFIED
		15a. DECLASSIFICATION/DOWNGRADING SCHEDULE n/a

16. DISTRIBUTION STATEMENT (of this Report)

DISTRIBUTION STATEMENT A
Approved for public release;
Distribution Unlimited

17. DISTRIBUTION STATEMENT (of the abstract entered in Block 20, if different from Report)

18. SUPPLEMENTARY NOTES

19. KEY WORDS (Continue on reverse side if necessary and identify by block number)

Hall Currents
High-Current Stability
Low Density Conductivity
Beam Propagation
Electromagnetic Field Solution Methods

20. ABSTRACT (Continue on reverse side if necessary and identify by block number)

Hall-current effects in the redistribution of plasma currents and possible stability enhancement in electron beams were explored in a range of pressure regimes Improved e.m. algorithms and conductivity models were developed as part of the studies. Substantial effects were found below a low-pressure threshold, where nonlocal effects, non-Ohmic conductivity, and a highly non-Maxwellian distribution of plasma electron energies were all found to contribute significantly to the magnitude of Hall-current phenomena. Several e.m. field algorithms were developed for application to the nonlinear hose-

DD FORM 1 JAN 73 1473 EDITION OF 1 NOV 65 IS OBSOLETE UNCLASSIFIED CONTINUED---

SECURITY CLASSIFICATION OF THIS PAGE (When Data Entered)

20. ABSTRACT (continued)

displacement regime. An iterative approach to the solution of the modally-expanded field equations was found to yield fast and accurate solutions.

TABLE OF CONTENTS

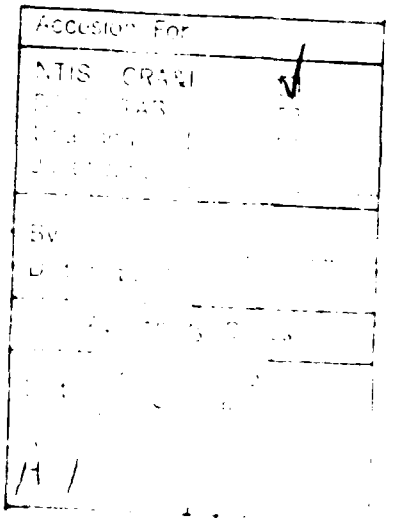

1.0 INTRODUCTION

This document is a final report on studies of high current beam propagation in low density gases. The study has extended over several years and has resulted in two informal interim topical reports -- resummarized herein. Three topics have been addressed: Ohmic Hall currents, non-local non-Ohmic conductivity modelling, and non-linear electromagnetic algorithms. The Hall and non-local conductivity studies are important primarily for high beam currents in low density gases; the non-linear electromagnetic field solvers are important for studying beams in low density channels.

Our initial studies of Hall current effects were motivated by the observation that the $\vec{E}x\vec{B}$ drift of plasma electrons would tend to expand the radial distribution of plasma current and reduce the normal axial current. The initial supposition was that these stabilizing effects would be most important for high currents and low channel densities, since the Hall currents scale directly with the Larmor frequency, ω_L, and inversely with the collision frequency, ν_m. Countervailing effects, however, include:

- o The high level of current neutralization characteristic of high-current beams,
- o Saturation of Hall-current effects by their associated potential buildup, and
- o Transition in the high-current regime to Spitzer conduction in the beam core, enhancing on-axis conductivity relative to neutral-collision-dominated conductivity in the wings of the beam's profile.

Further complexities in the actual situation include the interplay between E_r- and E_z-fields in the progress of avalanche breakdown at the head of the beam, the effects of air chemistry processes (especially recombination), and the role of radiative cooling in determining the onset of Spitzer conduction. Progress in modelling these effects included the development of a dependable electromagnetic algorithm; the algorithm included forward-time differencing and an iterative approach to find fields in the highly nonlinear situation created by the presence of tensor conductivity effects.

Studies of the effects of Hall currents in a local, Ohmic approximation are reported in Section 2. No consequences significant to beam propagation or stability are seen for gas pressures greater than 76 torr. At lower pressures, however, the usual local, Ohmic air conductivity models employed in the study are inappropriate. Significant effects which must be considered include:

- o Time-dependent (delayed) and nonlocal ionization production, in contrast to the usual local, instantaneous production models,
- o Contributions to the total current from the delta-ray components of the beam-driven ionization cascade,
- o Non-Ohmic conductivity effects,
- o Transport of electrons from their local volume of creation, and
- o Non-Maxwellian energy distribution of the conduction electrons, notably in the "runaway" regime; low effective collision frequency, in comparison to ω, could especially enhance the contributions of a high energy conduction group.

A conductivity model incorporating the above-noted effects has been developed and is reported in Section 3. The model treats three electron-energy groups: a relativistic (delta) group, and high- and low-energy conduction groups. The beam, as well as each group, populate lower-energy groups via ionization energy loss; E-field acceleration can move low-energy electrons upward to the intermediate group. Fluid models represent the dynamics of the two lower-energy groups, and a detailed air-chemistry reaction scheme also modifies the population of the low-energy group. The air chemistry was calibrated against the detailed HICHEM code in an applicable regime.

Calculations with the phenomenological model sketched above showed considerably enhanced and broadened effective current profiles at times between 1 and 10 nsec for high-current beams. All of the features of improvement appeared to make significant contribution to the results obtained.

In the most recent portions of our work, reported in Section 4, several electromagnetic field algorithms for beam-propagation work were developed and compared. The aim of the work was to find solution methods appropriate to extend phenomenological models of beam dynamics (especially

those relevant to hose stability) into the nonlinear regime -- i.e., to be applicable for displacements comparable to beam radii. Several fast and accurate algorithms were found. All were based on a modal expansion of the transverse spatial dependence of the fields, and all used an iterative procedure to simplify the solution for the mode amplitudes. (The modes are all coupled through the non-axisymmetry of the conductivity, and require, in principle, simultaneous solution for all modes.) Formulations involving explicit consideration of fields as well as potentials in Lee's approximation (an important simplification of the frozen-field approximation) and a frozen-field formulation were used. The simplified approaches were found to agree well with one another, and with the few-point data available from other nonlinear field-solver algorithms. Moderate differences -- especially in electric fields -- were seen in the frozen-field formulation results for a standard test case. Substantial improvements in speed for the algorithms developed over direct-solution methods for the fully-coupled-mode equations appear to have been realized.

2.0 HALL CURRENT EFFECTS IN A LOCAL CONDUCTIVITY MODEL

2.1 Introduction

This section summarizes our studies of the effects of Ohmic Hall currents on the propagation of high current beams in low density gases. Non-Ohmic, non-local Hall effects are discussed in Section 3. Beams of very high current have attracted increased attention recently due to potential stability and application advantages (Refs. 1, 2).

The Hall currents derive from the $\vec{E}x\vec{B}$ drift of the plasma electrons. Thus, due to the pinching azimuthal magnetic field B_ϕ, plasma electrons driven by the inductive longitudinal electronic field will drift toward larger radii, and those driven by the Coulombic radial electric field will tend to cancel the axial plasma current. Initial estimates of the resulting redistribution of plasma currents relative to beam currents suggested potentially significant consequences to beam stability and propagation. The purpose of the study herein reported was to substantiate the initial estimates and to explore some of the consequences.

Hall currents enter Maxwells equations through terms proportional to the Larmor frequency ω_L divided by the collision frequency ν_m.

$$\chi = \omega_L / \nu_m$$

Thus, Hall effects vary directly with <u>net</u> current and inversely with gas density. One anticipates Hall effects to become important at very high currents and low densities. In the Ohmic approximation, however, these two requirements tend to be mutually exclusive; high current beams in low density gases tend to be strongly current neutralized and develop very small net current - χ remains small.

In the body of the pulse, Hall effects achieve a quasi-stationary state and all quantities important to beam dynamics become nearly independent of χ, no matter how large χ may become. Thus, Hall-dependent consequences require that current neutralization be substantially less than complete in the very early portions of the pulse.

For a realistic range of high current beam parameters - assuming Bennett beam profiles and local conductivity models - Hall current effects remain small. Near complete current neutralization obtains near the pulse head and remains small. Only by artifically constraining the conductivity profile evolution have we demonstrated important Hall current sensitivities. Results are thus very sensitive to non-local conductivity effects, described in Section 3.

In Section 2.2 the general development of Hall currents is presented, including monopole and dipole decomposition, and Section 2.3 describes some numerically stable algorithms for monopole Hall currents effects. Results are in Section 2.4 and our conclusions to date are in the concluding section.

2.2 Theory

In this section we derive the relevant electromagnetic field equations as employed in this study, and discuss some important properties of tensor conductivity. We begin with Maxwell equations in free space (Gaussian units):

$$\vec{\nabla}\times\vec{B} = \frac{1}{c}\frac{\partial\vec{E}}{\partial t} + \frac{4\pi}{c}\vec{J} \quad : \quad \text{Ampere's Law} \tag{2.1}$$

$$\vec{\nabla}\times\vec{E} = -\frac{1}{c}\frac{\partial B}{\partial t} \quad : \quad \text{Faraday's Law} \tag{2.2}$$

where the net-current $\vec{J}$ consists of both the primary beam-current $\vec{J}_b$ and the plasma-current $\vec{J}_p$,

$$\vec{J} = \vec{J}_b + \vec{J}_p \quad . \tag{2.3}$$

For the purposes of discussion, a simple model of the Hall current effects may be obtained as follows. We assume that the plasma electrons obey the Lorentz equation of motion with a phenomenological momentum transfer frequency ν_m

$$m_e \frac{d\vec{v}}{dt} = e\vec{E} + \frac{e}{c}\vec{v}\cdot\vec{B} - m_e \nu_m \vec{v} \quad . \tag{2.4}$$

In the local approximation, the inertial term may be ignored, $d\vec{v}/dt \approx 0$. With this approximation, we obtain the generalized ohmic relation for the plasma-current density:

$$\vec{J}_p = e\, n_e\, \vec{v} = \sigma\vec{E} - \frac{\vec{\omega}}{\nu_m}\times\vec{J}_p \tag{2.5a}$$

with

$$\sigma = \frac{e^2 n_e}{m_e \nu_m} \tag{2.5b}$$

$$\vec{\omega} = \frac{e\vec{B}}{m_e c} \quad . \tag{2.5c}$$

σ is the usual scalar conductivity and $|\vec{\Omega}|$ is the electron gyrofrequency. It is the cross-product on the right side of Eq. (2.5a) that produces the Hall current. Later in this section we discuss a more rigorous treatment where the "momentum transfer frequency" in Eq. (2.4) is itself a function of the plasma electron distribution.

Solving for $\vec{J}_p$ in Eq. (2.5a), we find

$$\vec{J}_p = \frac{\sigma}{(1 + |\Omega|^2/\nu_m^2)} \left[\vec{E} - \frac{\vec{\Omega}}{\nu_m} \times \vec{E} + \frac{\vec{\Omega}}{\nu_m} \frac{(\vec{\Omega}\cdot E)}{\nu_m} \right] \tag{2.6}$$

In cylindrical coordinates (r,ϕ,z), Eq. (2.6) becomes

$$J_{pr} = \frac{\sigma}{(1 + |\Omega|^2/\nu_m^2)} \left\{ E_r - \frac{\Omega_\phi}{\nu_m} E_z + \frac{\Omega_z}{\nu_m} E_\phi + \frac{\Omega_r}{\nu_m} \frac{(\vec{\Omega}\cdot\vec{E})}{\nu_m} \right\} \tag{2.7a}$$

$$J_{p\phi} = \frac{\sigma}{(1 + |\Omega|^2/\nu_m^2)} \left\{ E_\phi - \frac{\Omega_z}{\nu_m} E_r + \frac{\Omega_r}{\nu_m} E_z + \frac{\Omega_\phi}{\nu_m} \frac{(\vec{\Omega}\cdot\vec{E})}{\nu_m} \right\} \tag{2.7b}$$

$$J_{pz} = \frac{\sigma}{(1 + |\Omega|^2/\nu_m^2)} \left\{ E_z - \frac{\Omega_r}{\nu_m} E_\phi + \frac{\Omega_\phi}{\nu_m} E_r + \frac{\Omega_z}{\nu_m} \frac{(\vec{\Omega}\cdot\vec{E})}{\nu_m} \right\} \tag{2.7c}$$

This form for $\vec{J}_p$ may now be substituted back into Maxwell equations (2.1 and 2.2) to provide a closed set of equations for generating $(\vec{E},\vec{B})$ from $\vec{J}_b$.

To make the problem computationally tractable, we decompose Maxwell equations into monopole-dipole subsets. We assume the following form for $\vec{E}$, $\vec{B}$ and $\vec{J}$:

$$\begin{aligned} E_r &= E_r^o + E_r' e^{i\phi} \\ E_\phi &= E_\phi^o + E_\phi' e^{i\phi} \\ E_z &= E_z^o + E_z' e^{iz} \\ B_r &= B_r^o + B_r' e^{iz} \quad , \quad \text{etc.} \end{aligned} \tag{2.8}$$

where we have made the dependence on ϕ explicit. Furthermore, we introduce the retarded variable $x = c\,t - z$ which we define to measure the distance back from the pulse head (in the laboratory frame of reference) for a beam moving along the z-axis with $v_z \sim c$. Finally, we make the frozen field assumption; all dependent variables are functions only of the independent variables (x,r), achieved by the following transformation on the partial derivatives in Eqs. (2.1) and (2.2):

$$\left.\frac{\partial}{\partial t}\right|_z \Rightarrow c \left.\frac{\partial}{\partial x}\right|_z \quad , \quad \left.\frac{\partial}{\partial z}\right|_t \Rightarrow - \left.\frac{\partial}{\partial x}\right|_z \tag{2.9}$$

The monopole equations reduce to three equations relating E^o_r, B^o_ϕ, and E^o_z and a second set of three equations relating B^o_r, E^o_ϕ, and B^o_z. We may ignore the second set for $J^o_{b\phi} = 0$ ($B^o_r = E^o_\phi = B^o_z = 0$). We are left with the set of equations for the axi-symmetric beam:

$$\frac{1}{r}\frac{\partial}{\partial r}\, r\, B^o_\phi = \frac{\partial E^o_z}{\partial x} + \frac{4\pi}{c}\,(J^o_{bz} + J^o_{pz}) \tag{2.10a}$$

$$\frac{\partial}{\partial x}\, B^o_\phi = \frac{\partial E^o_r}{\partial x} + \frac{4\pi}{c}\,(J^o_{br} + J^o_{pr}) \tag{2.10b}$$

$$\frac{\partial E^o_r}{\partial x} + \frac{\partial E^o_z}{\partial r} = \frac{\partial B^o_\phi}{\partial x} \tag{2.10c}$$

For the dipole fields, we have

$$\frac{1}{r}\frac{\partial}{\partial r}\, r\, B'_\phi - \frac{B'_r}{r} = \frac{\partial E'_z}{\partial x} + \frac{4\pi}{c}\,(J'_{bz} + J'_{pz}) \tag{2.11a}$$

$$-\frac{\partial B'_r}{\partial x} - \frac{\partial B'_z}{\partial r} = \frac{\partial E'_\phi}{\partial x} + \frac{4\pi}{c}\,(J'_{b\phi} + J'_{p\phi}) \tag{2.11b}$$

$$\frac{B'_z}{r} + \frac{\partial B'_\phi}{\partial x} = \frac{\partial E'_r}{\partial x} + \frac{4\pi}{c}\,(J'_{br} + J'_{pr}) \tag{2.11c}$$

$$\frac{1}{r}\frac{\partial}{\partial r}\, r\, E'_\phi + \frac{E'_r}{r} = -\frac{\partial B'_z}{\partial x} \tag{2.11d}$$

$$\frac{\partial E'_r}{\partial x} + \frac{\partial E'_z}{\partial r} = \frac{\partial B'_\phi}{\partial x} \tag{2.11e}$$

$$-\frac{E'_z}{r} + \frac{\partial E'_r}{\partial x} = -\frac{\partial B'_r}{\partial x} \tag{2.11f}$$

Note that the $\vec{\nabla}\cdot\vec{B} = 0$ condition is treated as an initial condition which is preserved by both the monopole and dipole equations.

From Eq. (2.7) we find

$$J^o_{pr} = \frac{\sigma^o}{(1 + \Omega^{o2}_\phi/\nu^{o2}_m)}\left[E^o_r - \frac{\Omega^o_\phi}{\nu^o_m} E^o_z\right] = \sigma^o_{\parallel} E^o_r - \sigma^o_{\perp} E^o_z \tag{2.12a}$$

$$J^o_{p\phi} = 0 \tag{2.12b}$$

$$J^o_{pz} = \frac{\sigma^o}{(1 + \Omega^{o2}_\phi/\nu^{o2}_m)}\left[E^o_z + \frac{\Omega^o_\phi}{\nu^o_m} E^o_r\right] = \sigma^o_{\parallel} E^o_z + \sigma^o_{\perp} E^o_r \tag{2.12c}$$

with

$$\sigma^o_{\parallel} \equiv \frac{\sigma^o}{(1 + \Omega^{o2}_\phi/\nu^{o2}_m)} \quad , \quad \sigma^o_{\perp} \equiv \frac{\sigma^o\,(\Omega^o_\phi/\nu^o_m)}{(1 + \Omega^{o2}_\phi/\nu^{o2}_m)} \tag{2.12d}$$

The dipole plasma current-density J'_p also follows from Eq. (2.7). After linearizing with respect to the dipole variables, we find

$$J'_{pr} = \sigma^o_{\parallel} E'_r + \sigma'_{\parallel} E^o_r - \sigma^o_{\perp} E'_z - \sigma'_{\perp} E^o_z \tag{2.13a}$$

$$J'_{p\phi} = \left[\sigma^o + \sigma^o_{\perp}\frac{\Omega^o_z}{\nu^o_m}\right] E'_\phi + \left[\sigma^o\frac{\Omega'_r}{\nu^o_m} + \sigma^o_{\perp}\frac{\Omega'_z}{\nu^o_m}\right] E^o_z - \left[\sigma^o\frac{\Omega'_z}{\nu^o_m} - \sigma^o_{\perp}\frac{\Omega'_r}{\nu^o_m}\right] E^o_r \tag{2.13b}$$

$$J'_{pz} = \sigma^o E'_z + \sigma' E^o_z + \sigma^o_{\perp} E'_r + \sigma'_{\perp} E^o_r \tag{2.13c}$$

with

$$\sigma'_{\parallel} = \frac{\sigma'}{(1 + \Omega_\phi^{0^2}/\nu_m^{0^2})} - \frac{2\,\sigma^0}{(1 + \Omega_\phi^{0^2}/\nu_m^{0^2})^2}\left(\frac{\Omega_\phi^0}{\nu_m^0}\right)^2\left[\frac{\Omega'_\phi}{\Omega_\phi^0} - \frac{\nu'_m}{\nu_m^0}\right] \tag{2.13d}$$

$$\sigma'_{\perp} = \frac{\sigma'}{(1 + \Omega_\phi^{0^2}/\nu_m^{0^2})}\frac{\Omega_\perp^0}{\nu_m^0} + \frac{\sigma^0(1 - \Omega_\phi^{0^2}/\nu_m^{0^2})}{(1 + \Omega_\phi^{0^2}/\nu_m^{0^2})^2}\left(\frac{\Omega_\phi^0}{\nu_m^0}\right)\left[\frac{\Omega'_\phi}{\Omega_\phi^0} - \frac{\nu'_m}{\nu_m^0}\right] \tag{2.13e}$$

where

$$\vec{\Omega}' = \frac{e}{m_e c}(B'_r,\ B'_\phi,\ B'_z) \tag{2.13f}$$

This completes the specification of the tensor plasma currents in terms of the electromagnetic field variables.

In the presence of the Hall current terms, the radial plasma current J^0_{pr} (2.12a) flows until $E^0_r \sim \sigma^0_\perp E^0_z/\sigma^0_\parallel$, in contrast to scalar calculations where the condition for $J^0_{pr} \sim 0$ is $E^0_r \sim 0$. Thus E^0_r actually reverses in sign from its original value set up by the Coulomb field of the beam particles. When E^0_r reaches this "quasi-equilibrium" value, the expression for the axial plasma current J^0_{pz} as given by Eq. (2.12c) becomes

$$J^0_{pz} \sim \sigma^0\, E^0_z \tag{2.14}$$

which is exactly the same as the scalar result without Hall currents. Similarly, for the Ohmic heating term $\vec{J}^0_p \cdot \vec{E}^0$, we find

$$\vec{J}^0_p \cdot \vec{E}^0 \sim \sigma^0\, E^{0^2}_z \tag{2.15}$$

for $J^0_{pr} \sim 0$, which is the usual scalar relation. Thus, the non-zero equilibrium value of E^0_r in the tensor case exactly compensates for the fact that $\sigma^0 < \sigma^0$ in Eq. (2.12). $E^0_r \neq 0$ effectively describes a polarization of the plasma.

We might conclude from this cancellation of terms that the Hall current effects on an axi-symmetric beam are negligible when the radial plasma currents are small. This would apply to the body of a beam pulse where charge neutralization is complete and the beam envelope has settled down to some quasi-static equilibrium profile. However, if the Hall effects are sufficient to alter the evolution of the conductivity channel and EM-fields near the beam head, where the condition $J^o_{pr} \sim 0$ is <u>not</u> satisfied, we might still expect to see a residue of the tensor conductivity effect further back in the beam where $J^o_{pr} \sim 0$. In other words, both σ^o and E^o_z would be noticeably different in both Eq. (2.14) and (2.15) in the body of the pulse due to Hall current effects in the pulse head. It has been the purpose of the present study to explore the non-equilibrium evolution of tensor conductivity near the beam head.

The tensor conductivity contribution to the plasma current in Eq. (2.12) relies on the parameter Ω/ν_m. Initial estimates of tensor effects were based on the observation that Ω/ν_m varies roughly as ρ^{-1} where ρ is the ambient gas density due to the basic density dependence of ν_m. However, the gyrofrequency Ω depends linearly on the net current which in turn depends indirectly (but strongly) on the channel density and channel profile. Hence, there is no simple or unique relationship between Ω/ν_m and density .

For a high intensity beam in a low density medium, a further complication results from the fact that the dominant contribution to the momentum transfer frequency ν_m shifts from electron-neutral collisions to Coulomb collisions. Two important changes occur at this point: (1) The conductivity becomes independent of electron density (in fact decreases if multiply-charged ions contribute a substantial fraction of the electrons); and (2) σ scales as $T_e^{3/2}$ instead of roughly $T_e^{-1/2}$. The transition to the Coulomb regime on-axis sharpens the conductivity profile, allows more plasma current to flow near the axis, and tends to decrease the net current flowing in this region. This sensitivity to electron temperature points up the importance to radiative cooling effects -- only roughly modeled here.

We conclude this section be noting that the exact cancellation of the tensor effects in Eq. (2.12) for $J^0_{pr} \sim 0$ is a model dependent result. Its validity requires that

$$\sigma_{\parallel}\left(1 + \left(\frac{\sigma_{\cdot}}{\sigma_{\parallel}}\right)^2\right) = \sigma^0 \tag{2.16}$$

for all values of B. A more general theory in which the random motion of the electrons is taken into account does not satisfy this requirement. For example, if electron-electron scattering is neglected (Ref. 3),

$$\sigma - i\sigma_{\cdot} = \frac{N_e e}{m\,\Gamma\left(\frac{5}{2}\right)} \int_0^{\infty} \frac{x^{3/2} \exp(-x)\, dx}{\nu(v) + i\Omega} \tag{2.17}$$

where

$$x \equiv \frac{1}{2} m v^2/kT$$

and $\nu(v)$ is the electron collision frequency with neutrals or ions. Only if ν is independent of velocity v, or for other very special cases, can the relation (Eq. 2.16) be satisfied exactly.

2.3 Monopole Tensor Electromagnetic Algorithm

2.3.1 Introduction

The basic monopole equations in the frozen approximation (Eq. 2.10) can be written in the form

$$\frac{\partial E_z}{\partial t} + 4\pi J_z = \frac{c}{r}\frac{\partial}{\partial r}(r B) - 4\pi J_B \tag{2.18a}$$

$$\frac{\partial E_r}{\partial t} + 4\pi J_r = \frac{\partial B}{\partial t} \tag{2.18b}$$

$$\frac{\partial E_z}{\partial r} = \frac{4\pi}{c} J_r \tag{2.18c}$$

where the superscript "o" has been dropped through this entire section. [Note that in the frozen approximation, the step Δx along the pulse length is equivalent to a timestep Δt as the beam passes a given fixed spatial point.] The plasma current densities J_z and J_r take the form

$$J_z = \sigma_{\parallel} E_z + \sigma_{\perp} E_r$$

$$J_r = \sigma_{\parallel} E_r - \sigma_{\perp} E_z.$$

If $\sigma_{\perp} \equiv 0$ (no Hall current) the equations are much less strongly coupled together, and are linear except for the indirect dependence of σ on $\vec{E}$ through the ohmic heating. However, if Hall effects are included a more explicit non-linearity enters because $\sigma_{\perp}$ is roughly proportional to B.

Several different numerical treatments of these equations have been investigated in this work. The algorithm currently in use is described below, followed by discussions of some other methods which were tried and the reasons they were found to be unsatisfactory.

A major difficulty with standard electromagnetic algorithms in the charged particle beam context is that the conductivity becomes so large that it is impractical to adhere to the timestep constraint $4\pi\ \sigma_{\parallel}\Delta t \ll 1$ which arises in the usual difference treatment of these equations. Although forward centering can eliminate the numerical constraint, it can also prejudice the solution. This is an uncertainty which has yet to be completely resolved satisfactorily. In at least one case, however, our forward-centered methods have been checked by choosing the time step to satisfy $\Delta t \ll \frac{1}{4\pi}\Delta$; no significant difference was observed.

2.3.2 The Present Algorithm

Equation (2.18a) is written in the time-integrated form

$$E_z = E_{zo}\exp(-4\pi\sigma_{\parallel}\Delta t) + \left|\frac{c}{r}\frac{\partial}{\partial r}(rB) - 4\pi J_B - 4\pi\sigma_{\parallel}E_r\right|\left|\frac{(1-\exp(4\pi\sigma_{\parallel}\Delta t))}{4\pi\ \sigma_{\parallel}}\right| \qquad (2.19)$$

where E_{zo} is the value of E_z at the beginning of the timestep Δt, but all other quantities are evaluated at the end of the timestep. Although the centering is not perfect when $4\pi\ \sigma_{\parallel}\Delta t \lesssim 1$, the forward centering is found to contribute significantly to stability and is simpler. When $4\pi\ \sigma_{\parallel} \gg \partial/\partial t$, as is usually the case in the spatial region occupied by the beam, the centering used above gives the correctly-centered result

$$\frac{4\pi}{c}(c\ E_z + \sigma_{\perp}E_r) + \frac{4\pi}{c}J_B = \frac{1}{r}\frac{\partial}{\partial r}(r\ B). \qquad (2.20)$$

In this equation all quantities are evaluated at the forward time. It is exactly the same result as is obtained by neglecting displacement current in Eq. (2.18a), and requiring that the resulting equation hold at $t + \Delta t$.

Equation (2.18b) is written as

$$\frac{\partial E_r}{\partial t} + 4\pi\ \sigma_{\perp}\ E_r = \frac{\partial B}{\partial t} + 4\pi\ \sigma_{\perp}\ E_z \qquad (2.21)$$

from which

$$E_r(1 + 4\pi\sigma_{\parallel}\Delta t) = \left(\frac{\partial B}{\partial t} + 4\pi\sigma_{\perp} E_z\right)\Delta t + E_{ro} \tag{2.22}$$

or

$$E_r = \frac{\Delta t\left(\frac{\partial B}{\partial t} + 4\pi\sigma_{\perp} E_z\right)}{1 + 4\pi\sigma_{\parallel}\Delta t} + \frac{E_{ro}}{1 + 4\pi\sigma_{\parallel}\Delta t} \tag{2.23}$$

In this equation, E_{ro} is the value at time t, and all other quantities are to be evaluated at $t + \Delta t$. In practice, $\partial B/\partial t$ is evaluated as $(B(t+\Delta t) - B(t))/\Delta t$, a possible weakness to the method because of the centering. Note that the exponential method as used for the E_z equation could have been used here also.

Equation (2.23) is then substituted into Eq. (2.18c), written in the form

$$\frac{\partial E_z}{\partial r} = \frac{4\pi}{c}(\sigma_{\parallel} E_r - \sigma_{\perp} E_z) \quad , \tag{2.24}$$

and interpreted as being at time $t + \Delta t$. The result is

$$\frac{\partial E_z}{\partial r} = \frac{4\pi}{c}\left[\frac{\sigma_{\parallel}}{1 + 4\pi\sigma_{\parallel}\Delta t}\left(\Delta t\left(\frac{\partial B}{\partial t} + 4\pi\sigma_{\perp} E_z\right) + E_{ro}\right) - \sigma_{\perp} E_z\right] \tag{2.25}$$

When this equation is simplified a very important cancellation occurs in the coefficient of $\sigma_{\perp} E_z$, which takes it from being of order unity to order $(1+4\pi\sigma_{\parallel}\Delta t)^{-1}$, a small number when $4\pi\sigma_{\parallel}\Delta t >> 1$. An analogous cancellation occurs if the exponential form is used. The resulting equation is

$$c\frac{\partial E_z}{\partial r} = \frac{4\pi\sigma_{\parallel}}{1 + 4\pi\sigma_{\parallel}\Delta t}\left[\Delta t\frac{\partial B}{\partial t} + E_{ro}\right] - \frac{4\pi\sigma_{\perp} E_z}{1 + 4\pi\sigma_{\parallel}\Delta t} \tag{2.26}$$

The final form used for differencing is

$$\frac{\partial E_z}{\partial r} = \frac{4\pi\,\sigma_{\parallel}}{c}\;\frac{1}{1 + 4\pi\sigma_{\parallel}\Delta t}\left(B - \frac{\sigma_{\perp} E_z}{\sigma_{\parallel}} - (B - E_r)_o\right) \qquad (2.27)$$

where again the subscript "o" indicates terms evaluated at time t. All other terms are evaluated at t + Δt.

The two Equations (2.19) and (2.27) must be solved simultaneously. Since neither is linear because of the strong and direct dependence of $\sigma_{\perp}$ on B, an iterative procedure is used. The $\sigma_{\perp} E_z/\sigma_{\parallel}$ term in Eq. (2.27) is written as

$$\frac{\sigma_{\perp} E_z}{\sigma_{\parallel}} \equiv \frac{\dot{\sigma}_{\perp} B}{\sigma_{\parallel}}$$

and $\dot{\sigma}_{\perp}/\sigma_{\parallel}$ is adjusted during the course of the iteration process. Thus the coefficient of B in Eq. (2.27) becomes

$$\left(1 - \frac{eE_z}{mc\bar{\nu}}\right)$$

in the simple theory of the Hall effect. This quantity is > 1 except when $E_z > 0$ at the end of the pulse. In Eq. (2.19) the term in $\sigma_{\perp} E_r$ is updated during the course of the iteration process, but is regarded as given for each iteration. Also the weaker dependence of $\sigma_{\parallel}$ on B (for most situations encountered) is ignored within each iteration step.

With these approximations, Eqs. (2.19) and (2.27) can be combined into a single equation for B

$$\frac{\partial}{\partial r}\left[\frac{c\Delta t}{r}\frac{\partial}{\partial r}(rB) - \right] - B\left(1 - \frac{\dot{\sigma}_{\perp}}{\sigma_{\parallel}}\right)\frac{4\pi\,\sigma_{\parallel}}{c(1 + 4\pi\sigma_{\parallel}\Delta t)}$$

$$= -\frac{(B-E_r)_o}{c}\;\frac{4\pi\,\sigma_{\parallel}}{(1 + 4\pi\sigma_{\parallel}\Delta t)} + \frac{\partial}{\partial r}\left(4\pi\Delta t(J_B + \sigma_{\perp} E_r)_o - E_{zo}\right) \qquad (2.28)$$

in which $\chi \equiv \exp(-4\pi\sigma_\perp \Delta t)$

and $\psi \equiv (1 - \chi)/(4\pi\sigma_\perp \Delta t)$.

[Note that the $\sigma_\perp E_r$ term in Eq. (2.19) could be rewritten as $\sigma_\perp E_r \equiv B\hat{\sigma}_\perp$, in analogy to the treatment of the $\sigma_\perp E_z$ term in Eq. (2.27). However, the explicit B-dependence introduced in that way would spoil the diagonal-dominant nature of the final equation for B. Also, E_r itself has a strong B dependence which would be ignored by the procedure in any case.] With $\sigma_\perp E_r$, $\hat{\sigma}_\perp/c$, and $\sigma_\parallel$ regarded as fixed, this equation is solved for B as a tridiagonal difference system. The values of $\sigma_\perp E_r$, $\hat{\sigma}_\perp/c_\perp$, and $\sigma_\parallel$ are then updated and the iteration procedure is continued until the values of the fields stabilize. Although there is no guarantee that this iteration procedure will converge, it has been found to converge well in the cases studied.

This algorithm has been installed and used in the HICHEM air chemistry code (Ref. 4) and in the HIGAP monopole-envelope code (Ref. 5). It appears to be numerically stable whether or not $\sigma_\perp/\sigma_\parallel$ is large. If $\sigma_\perp$ is set = 0, this algorithm (and minor variations of it) yields results essentially identical (within reasonable limits for numerical studies) to the previous scalar algorithms used in HIGAP and HICHEM. The latter two algorithms are different from each other and from the one described above in some aspects of the time centering. The agreement of numerical results for the scalar case does not guarantee the tensor results. Some aspect of the centering or differencing method could tend to suppress or enhance the potential non-linear evolution of the tensor solutions away from the scalar solutions.

2.3.3 Alternative Numerical Approaches

In the treatment discussed in Section 2.3.2 above it was necessary to split up the $\perp$ and $\parallel$ parts of the plasma current, treating the $\perp$ part as a source term on the right hand side of the equation. An alternative treatment which avoids the problem is to define

$$\mathcal{E} \equiv E_z + i\, E_r$$

$$\mathcal{J} \equiv J_z + i\, J_r,$$

then multiply Eq. (2.18b) by i and add to (2.18a). The result is

$$\frac{\partial}{\partial t} + 4\pi\mathcal{J} = \frac{c}{r}\frac{\partial}{\partial r}(rB) - 4\pi J_B + \frac{i\partial B}{\partial t} \tag{2.29}$$

Now $\mathcal{J} \equiv \sigma^*\mathcal{E}$, with the definition

$$\sigma^* \equiv \sigma_r - i\sigma_i .$$

Then the exponential treatment, or full forward centering as indicated below, can be used to perform the time integration:

$$\mathcal{E} = \frac{\Delta t}{1 + 4\pi\sigma^*\Delta t}\left[\frac{c}{r}\frac{\partial}{\partial r}(rB) - 4\pi J_B + i\frac{\partial B}{\partial t}\right] + \frac{\mathcal{E}_0}{1 + 4\pi\sigma^*\Delta t} \tag{2.30}$$

This result is a more parallel treatment of E_z and E_r, treating only the magnetic field and the beam current J_B as source terms. The exponential treatment has the advantage of eliminating the initial value $\mathcal{E}_0$ faster, but has the added complication of $\binom{\cos}{\sin}(4\pi\sigma_i\Delta t)$ appearing, which can lead to sign changes in various terms where $4\pi\sigma_i\Delta t$ is not small. Note that in Eq. (2.30) $\partial B/\partial t$ acts directly as a source of E_z, and $\frac{\partial}{\partial r}(rB)$ acts directly as a source of E_r, unlike the situation in the formulation described in Section 2.3.2 above.

The attractiveness of this approach degrades when the next step is examined. Since Eq. (2.18) cannot be written in terms of $\mathcal{E}$ and $\mathcal{J}$ only, it is necessary to split (2.30) into its real and imaginary parts. In principle both E_r and E_z separately from (2.30) can be inserted in Eq. (2.24), yielding a single equation for B. However, because of the $\partial B/\partial t$ term in the expression for E_z and the spatial derivative in the expression for E_r, the resulting equation does not

involve B in a diagonally-dominant form, and thus is much less convenient to solve accurately. In addition it is much more complicated than Eq. (2.28) because of the splitting of $(1 + 4\pi\sigma^*\Delta t)^{-1}$ into real and imaginary parts.

A variation of this approach was actually tried prior to beginning the present study. This consisted of using E_r from Eq. (2.30) to eliminate E_r from Eq. (2.24), which was written in the form

$$\frac{\partial E_z}{\partial r} + \frac{4\pi}{c}\sigma_{\perp}E_z = \frac{4\pi}{c}\sigma_{\parallel}E_r \tag{2.31}$$

This equation was solved simultaneously with the E_z equation from (2.30) for E_z and B. Several minor variations of this were tried. In one case Eq. (2.31) was centered as

$$\frac{E_{zk+1} - E_{zk}}{\Delta r} + \frac{2\pi}{c}\left|(\sigma_{\perp}E_z)_k + (\sigma_{\perp}E_z)_{k+1}\right| = \frac{4\pi}{c}(\sigma_{\parallel}E_r)_{k+\frac{1}{2}} \tag{2.32}$$

Since all field variables were to be defined on the same spatial grid, the $k+\frac{1}{2}$ centering of the E_r expression from Eq. (2.30) is not inconvenient because of the appearance of the spatial derivative of B. However, the E_z equation from (2.30) is awkward to center with E_z and B on the same grid. The most direct way would involve B at three successive grid points. This was avoided by writing the left hand side of (2.30) as

$$\frac{1}{2}(E_{zk} + E_{zk+1})$$

and using the natural centering on the right hand side. It was found that this method of solution was highly unstable and totally unreliable.

Another variation tried involved writing (2.31) as

$$E_{zk+1}\left(1 + \frac{4\pi}{c}\sigma_{\perp}\Delta r\right) - E_{zk} = (\text{r.h.s.})_{k+\frac{1}{2}} \tag{2.33}$$

(in which r.h.s. is a function of B only), when $\sigma_\perp > 0$, and the analogous thing with centering in the other direction when $\sigma_\perp < 0$. The E_z equation from (2.30) was treated as described above. This system of two equations gave reasonable-looking solutions most of the time, provided that $\sigma_\perp$ was large, although it sometimes went unstable even in that situation. For cases where $\sigma_\perp/\sigma \ll 1$ it frequently exhibited unstable behavior. Thus it was impossible to do a study on the transition from small to large $\sigma_\perp$ using this one algorithm.

Apart from the occasionally unstable behavior, this algorithm has a more serious problem associated with the spatial centering of Eq. (2.33). That spatial centering is seriously biased if

$$\frac{4\pi\sigma_\perp \Delta r}{c} \gg 1 \quad .$$

It was not always possible to avoid this situation with a reasonable number of smoothly-distributed spatial grid points extending to large radius. This problem could have been avoided by a more complicated treatment of the right hand side. The basis for such a treatment can be seen by writing the solution to Eq. (2.31) in the form:

$$E_{zk+1} = E_{zk} \exp\left(-\frac{4\pi\sigma_\perp \Delta r}{c}\right) + \int_{r_k}^{r_{k+1}} \left(\frac{\sigma_\perp E_r}{\sigma}\right) \exp\left(\frac{4\pi\sigma_\perp (r-\Delta r)}{c}\right) dr \qquad (2.33)$$

in which r-dependence of $\sigma_\perp$ has been ignored for simplicity of exposition. Even the simple assumption that $\sigma_\perp E_r/\sigma$ varies linearly with r over Δr would allow a formulation in which the obvious bias of Eq. (2.33) is avoided. However, the cost involved is that the magnetic field at as many as four points rather than two would appear in the analogue of Eq. (2.33) because of the unnatural centering required in Eq. (2.30) for E_r.

There is another more fundamental objection to any simple implementation of Eq. (2.33). For sake of discussion assume that it is further developed by assuming $\sigma_{\perp} E_r/\sigma_{\perp}$ is linear over Δr. Then it is clear that when

$$\frac{4\pi\sigma_{\perp}\Delta r}{c} \gg 1$$

it will enforce the relationship

$$(\sigma_{\perp} E_z)_{k+1} \rightarrow (\sigma_{\parallel} E_r)_{k+1}$$

on the fields. Thus it is equivalent to forcing $J_r \rightarrow 0$, but is independent of the time-evolution of the solution and is therefore not physical. The resolution of this paradox is that $\sigma_{\parallel} E_r/\sigma_{\perp}$ must be allowed to have exponential behavior in r. Only then can a physically-consistent treatment be developed along these lines.

The bad behavior of the scheme using the correctly centered Eq. (2.32) can be identified by recalling the cancellation that occurred in going from Eq. (2.25) to (2.26). If the fields from Eq. (2.30) were <u>both</u> inserted in the right hand side of Eq. (2.24) and the cancellation done analytically, the remaining equation could then be centered as in Eq. (2.32). Although this procedure has not been tried, it is likely that much of the bad behavior of the system based on Eq. (2.32) would be eliminated.

As in the method discussed in Section 2.3.2, there remains the problem of the non-linearity introduced by the strong dependence of $\sigma_{\perp}$ on B. All of the methods discussed in the present section 2.3.3 involve $\sigma_{\perp}$ in many more places and in more complicated ways than in Eq. (2.28). No attempt has been made to iterate them because of the general success of the method discussed in Section 2.3.2.

2.4 Computational Results

2.4.1 Introduction

Two different SAI codes, HICHEM and HIGAP, were used to perform the calculations described below. Both incorporated the same basic electromagnetic algorithm which was described in Section 2.3.2. The tensor cases were iterated until the magnetic field changed by less than 1% between consecutive iterations. The simple model of the Hall current described in Section 2.2 was used for all the case studies. One comparison case was repeated using the full theory as described in Ref. 1.

The HICHEM code (Ref. 4) is a radially-resolved air chemistry code specifically designed to follow the air chemistry processes generated by an electron beam. It follows the non-equilibrium time evolution of up to 60 chemical species, and can account for radiative energy losses when these are important to the overall energetics. The conductivity calculation is also described in Ref. 1; it incorporates a very detailed model for electron collisions with neutral air species, ions, and other electrons, and computes the off-diagonal (Hall) component of the conductivity tensor in a consistent way. The electromagnetic field equations were solved on a grid of 290 radial points extending to 500 Bennett radii. The geometric grid spacing provided 18 points inside 1 Bennett radius, and 58 points inside 5 Bennett radii. Except as noted below, all the HICHEM calculations used the same 31 chemical species and 288 reactions. The cases which were followed out to 50 ns used 37 species and 337 reactions in order to account for substantial radiative cooling of the longer pulses.

The HIGAP code (Ref. 5) is a monopole propagation code designed to study monopole envelope evolution and nose erosion for axi-symmetric beams. The conductivity calculation in this code is provided by the BMCOND (Ref. 6) package of subroutines. This package uses a highly simplified model of the chemistry which has been calibrated against the more complicated HICHEM code. Several important

changes in these calculations were required to handle the high degree of ionization produced by high-current beams in low density air. The electromagnetic field equations were solved on a radial grid of 250 points extending to 20 cm from the beam axis.

Since the HIGAP code (in its non-propagating mode) is much less costly to run than the HICHEM code, it was used to investigate some more unusual or extreme cases for sensitivity to Hall effects.

For all calculations except Case 6, as noted below, the beam profile was assumed to be Bennett. The time-dependence of the beam current was given by

$$I = I_B \tanh\left(\frac{t}{\tau_1}\right) \tanh\left(\frac{\tau_1 - t}{\tau_1}\right) \quad . \tag{2.34}$$

The expanded nose of the beam was described by a time-varying Bennett radius specified by

$$a = a_o \left[1 + \frac{1}{2}\left(\frac{b}{a_o} - 1\right)\left(1 - \tanh\left(\frac{t - \tau_c}{\tau_R}\right)\right)\right] \quad , \tag{2.35}$$

in which a_o is the final radius as $t \to \infty$. The initial radius and the position and steepness of the pinch-down are controlled by the parameters b, τ_c, and τ_R.

2.4.2 Case Studies

Numerical results are discussed below for the cases described in Table 2-1 The beam current in each case was 100 kA. These cases were selected to provide a wide range of beam parameters and channel properties.

TABLE 2-1

Case	Beam Parameters		Nose Parameters				Channel Parameters		
	τ_1 (ns)	τ_2 (ns)	a_o (cm)	b (cm)	τ_c (ns)	τ_R (ns)	ρ/ρ_o	Width (Bennett radii)	T
1a	1	100	.2	1.4	0	4	.0363	3	6000
1b	.4	10	.2	.2	-	-	.0363	1	6000
2a	.4	10	.5	.5	-	-	.0363	1	6000
2b	.4	10	.5	.5	-	-	.0363	2	6000
2c	1	100	.5	2.5	0	4	.0363	3	6000
3a	.4	10	.2	.2	-	-	.1	uniform	288
3b	.4	10	.2	10	1	1	.1	uniform	288
4*	.4	10	.5	20	5	.5	.1	uniform	288
5*	.4	10	.5	.5	-	-	.1	uniform[1]	288
6*	.4	10	.5[2]	.5	-	-	.1	uniform	288
7a,b[3] Constrained	.5	50	.2	.2	-	-	.036	uniform	---

* HIGAP calculation

[1] Annular initial N_e distribution

[2] Hollow Profile

[3] Two cases with imposed conductivity radial profiles: (a) square root of Bennett and (b) Bennett

The basic model for the hot channel cases had a central temperature of 6000°K with the density chosen to give pressure equilibrium at 1 atmosphere. Three channel widths -- flat out to 1, 2, or 3 Bennett radii of the pinched beam (as in Eq. 2.35) -- were investigated. For cases 3 - 6, a cold uniform medium with density (and pressure) = 0.1 normal was used.

Nose parameters were chosen to simulate a variety of situations. For Cases 1a and 2c the parameters are interpreted as providing a tailored emittance which decreases significantly along the beam. Case 3b represents a beam with a moderately expanded nose, in contrast to Case 3a which is a cylindrical slug of charge. The parameters of Case 4 represent a very mature nose after considerable erosion of the beam-head has occurred.

Case 5 was chosen to investigate the effect of an initial distribution of electron density provided by an annular laser beam. This was expected to change the conductivity development in the wings and, hence, the distribution of plasma current.

Case 6 had a hollow beam current distribution, which resulted in significantly different conductivity and plasma current distribution from the conventional Cases 1 - 4. The beam current density on-axis was about .075 of the maximum, which occurred at about 0.5 Bennett radii.

In addition to the fully self-consistent calculations from the HICHEM and HIGAP codes (Cases 1 -6), two artifically constrained situations were studied in order to assess the sensitivity of the calculations to the conductivity profile. Conductivity profiles with (a) the square root of the beam profile and (b) the Bennett profile of the beam were imposed. The axial conductivity was taken to be proportional to the beam current, and there was no feedback to the conductivity from the rest of the calculation.

All the cases listed in Table 2-1 were calculated using both the scalar and tensor versions of the electromagnetic algorithm. Detailed discussions of the individual cases are given in Section 2.4.4 below, preceded by a general discussion of results in Section 2.4.3.

2.4.3 Discussion of Results

For a self-pinched beam the $\vec{J}\times\vec{B}$ force (Hall term) exerts an outward force on the backwards-flowing J_z plasma current. If this effect reduces the plasma current density near the beam axis, the net current density and local magnetic field increase. This in turn leads to an increased $\vec{J}\times\vec{B}$ force on the remaining plasma current. If this non-linear response is effective in expelling a significant amount of the J_z plasma current from the vicinity of the beam, the beam is more strongly pinched and its propagation characteristics are improved.

The calculations show that with or without Hall currents, the electromagnetic fields rapidly evolve toward the situation $J_r \sim 0$. The magnetic force term which pushes the J_z plasma current outward is then balanced by the radial electric field. Only a small residual J_r remains, generated by longer time-scale evolution of the magnetic field (due to conductivity profile evolution, for example, or continued evolution of the beam current or its radial distribution).

In none of the self-consistent cases investigated was there a large scale redistribution of the plasma current. Although ratios $\sigma_\perp/\sigma_\parallel \sim 0.25$ were achieved late in Case 1a, for example, $J_z(r)$ was essentially unchanged from the scalar case. This result is consistent with the simple theory discussed in Section 2.2, because the condition $J_r \sim 0$ was reached long before $\sigma_\perp/\sigma_\parallel$ reached a large value.

The constrained model with conductivity profile specified to be the square root of the Bennett beam profile was the only case to show significant differences between the scalar and tensor cases. The magnetic field at 1 Bennett radius increased steadily and essentially linearly with time from before 0.01 ns to beyond 10 ns. The scalar and tensor calculations even in this case did not differ significantly until about 1 ns. In contrast, the constrained model with a Bennett conductivity profile had a net current which was a factor 4 lower at 0.01 ns, and rose at a much slower rate initially. By 10 ns the ratio

$\sigma_\perp/\sigma_\parallel$ reached ~ 0.25, but the difference between scalar and tensor calculations was negligible, in accordance with the simple theory. For all the self-consistent cases, the early (before 1 ns) behavior of $\sigma_\perp/\sigma_\parallel$ was qualitatively similar to that of the Bennett profile constrained case; it increased relatively slowly in time, or even remained roughly constant.

It is tempting to conclude from the comparison of the two constrained cases that the conductivity profile determines whether or not Hall current effects can develop. For self-consistent calculations, several processes operate to determine the conductivity profile evolution. Initially, in a cold gas the ionization is produced by the beam and has a beam profile -- Bennett in all but Case 6 of the present study. As the Coulomb E_r field grows rapidly, it breaks down the air off-axis, causing a temporary (usually) off-axis peak in σ. Later the E_z field rises on-axis and dominates the air breakdown. The peak E_z field may occur as early as 0.05 ns if a broad nose is not present on the pulse. Usually the E_z field brings the peak of the conductivity profile back to the axis and gives it a shape roughly Bennett or even slightly narrower. As the conductivity grows rapidly near the axis the E_r field begins to short out and its peak moves outward beyond the main body of the beam. Conductivity in the far wings rises as the air is broken down by E_r. If the electron production on-axis is not too great, N_e begins to saturate due to dissociative recombination on molecular ions. In this situation a profile comparable to the square root of the Bennett can develop (but generally at $t \gtrsim 1$ ns). On the other hand, if the gas on-axis is ionized too quickly for recombination to keep up (or molecular ions are destroyed by the high temperatures) the Spitzer conductivity regime may be reached. As noted in Section 2.2 above, this generally sharpens the conductivity profile near the axis, although broad wings will persist. This entire sequence can be modified by providing a broad initial hot channel (as in Cases 1 and 2), an expanded nose, a long taper of the beam radius due to a variable emittance, or by a non-Bennett beam profile (Case 6) or a laser-prepared channel (Case 5). A very wide variety of profiles was provided by the self-consistent cases investigated, but in no instance did the qualitative behavior of the constrained broad-profile Case 7a emerge. The

feedback between the fields, net current, and conductivity is evidently more important than any of the modifications of conductivity profiles achieved by choice of channel parameters, beam parameters, nose parameters, etc., in the numerical calculations. For high current beams in low-density air the conductivity evolves rapidly enough, and the induced E_z is strong enough to allow very nearly complete current neutralization to be achieved early in the pulse, in the spatial region occupied by the beam itself rather than through large return currents in the wings.

As noted above, the constrained Case 7a did not develop large differences between the tensor and scalar calculations until after $\sim$ 1 ns, but both were qualitatively different in magnetic field behavior (as measured by $\sigma_\perp/\sigma_\parallel$) from Case 7b and the self-consistent cases. This suggests that it may be possible to identify, from scalar calculations only, situations in which significant tensor effects may arise.

2.4.4 Details of Case Studies

Case 1: 2 mm beam into a low density hot channel

Several different channel widths were investigated, as well as the effect of a variable emittance along the beam. Case 1a achieved the largest ratio of $\sigma_\perp/\sigma_\parallel$. The radial profiles of $\sigma_\parallel$ and $\sigma_\perp$ are shown in Figure 2.1 at several times late in the pulse, where $\sigma_\perp$ has grown to significant values $\sim$ 0.25 $\sigma_\parallel$ at 2 Bennett radii from the axis. In spite of the large $\sigma_\perp/\sigma_\parallel$, the difference in pinch function, net current, E_z filed, etc. between tensor and scalar calculations is negligible. Only the E_r field is substantially different from its value in the scalar case, and is closely given by the condition $J_r \sim 0$.

The net current integrated to radius r (including displacement current) is shown in Figure 2.2 as a function of radius and time. The specific volume relative to sea level air is also shown. It is clear that the plasma current density exceeds the beam current density in the region between about 2 Bennett radii and the channel wall at 4 Bennett radii. Even as late as 50 ns into the pulse, the net current inside 4 Bennett radii is only 2 kA, although inside 1 Bennett radius the net current is about 16 kA at that time. In the region $r < a$, the beam current is $\sim$ 84% neutralized by plasma current.

For Case 1b with channel walls moved inward by 2 Bennett radii, tensor effects are weaker still because the plasma current flow is even more strongly confined to the same spatial region as the beam current. Although an expanded nose and emittance tailoring could have improved the situation, it is unlikely they would have resulted in significant differences between the tensor and scalar calculations before $J_r \to 0$.

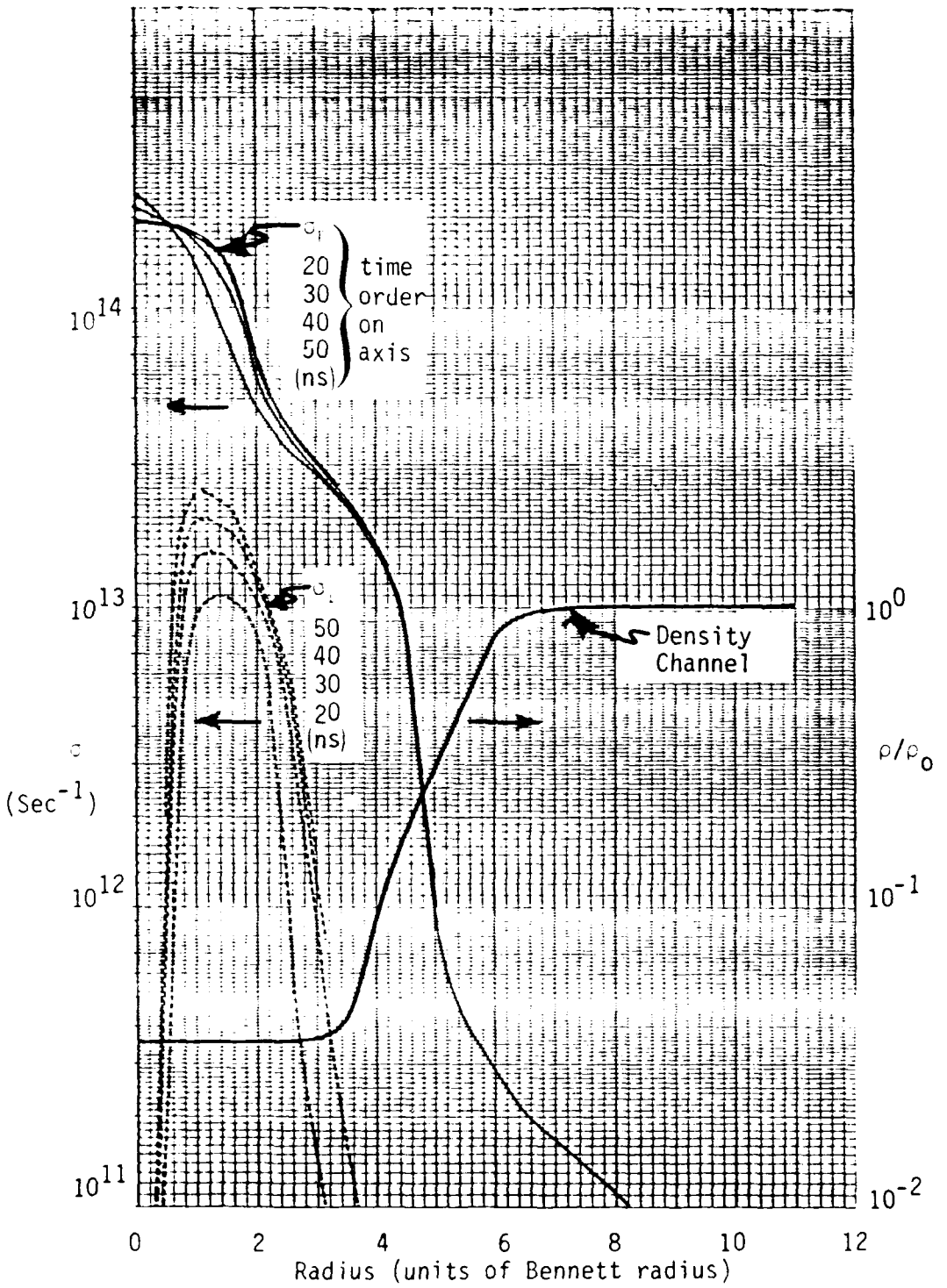

Figure 2.1. Case 1a: (Long Nose Tapering to 2mm. Radius) Conductivity (Sec^{-1}).

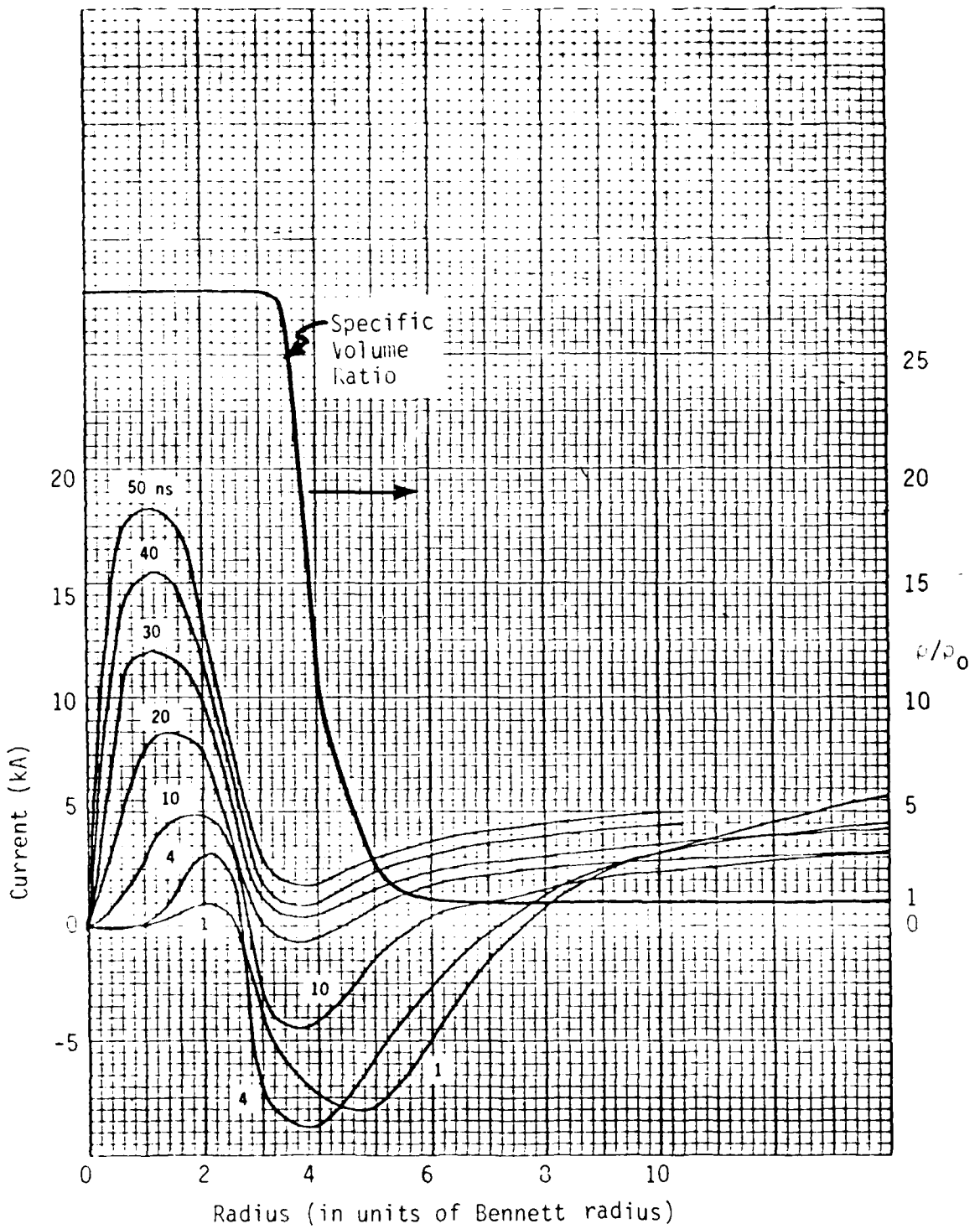

Figure 2.2. Case 1a: 2mm. (Long Nose Tapering to 2mm. Radius)
Net Current Integrated Out to Radius r.
$I_{net} = .005r\ B(r)$ (kA).

Case 2: 5 mm beam into three different hot channels

The conductivity is shown for this lower beam current density in Figure 2.3. The channel profile is the same as in Case 1a, Figure 2.1. In Case 2c the lower current density results in less strong plasma currents near the axis, but the magnetic field in the current distribution is weaker in general than in Case 1a. The ratio $\sigma_{\perp}/\sigma_{\parallel}$ barely exceeds .10 even late in the pulse. Again, this is long after the radial plasma current has approached zero, so there is essentially no difference between the tensor and scalar computational results except for the E_r field. As expected, the narrow channels (Cases 2a and 2b) were less favorable to the development of a strong magnetic field because of the confinement of the plasma current to the region near the beam.

Case 3: 2 mm beam into uniform density = 0.1 of sea level value

In some ways this case is like the extreme of a very wide channel, but with a very important qualitative difference. Since the Case 1-like channels are all chosen to be in pressure equilibrium, they have a significant initial conductivity $\sim 10^{12}$ sec $^{-1}$ in their low density (high initial temperature) regions. In Case 3, however, there is no initial conductivity channel because the temperature is taken to be uniform at 288°.

Conductivity results are shown in Figure 2.4. Because the beam itself is confined to a narrow region, it (and the accompanying ohmic heating) generates its own conductivity channel which is initially relatively confined within a few Bennet radii. Again, the plasma currents overlap the beam current substantially at early times, preventing it from establishing a strong magnetic field early in the pulse. Integrated plasma current profiles are shown as a function of radius at several times during the pulse in Figure 2.5.

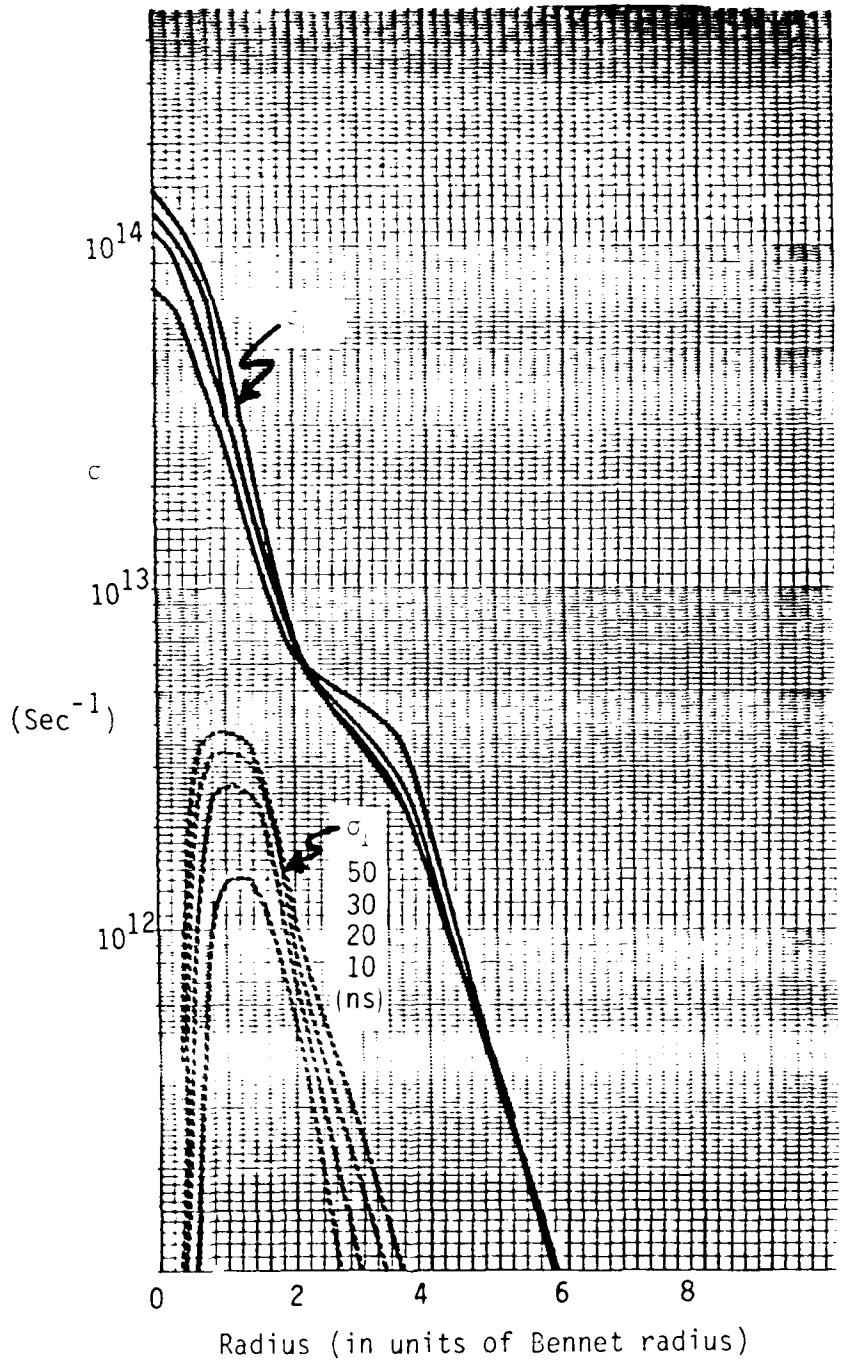

Figure 2.3. Case 2c: (Long Taper to 5mm. radius) Conductivity at Several Times in The Pulse (Sec^{-1}).

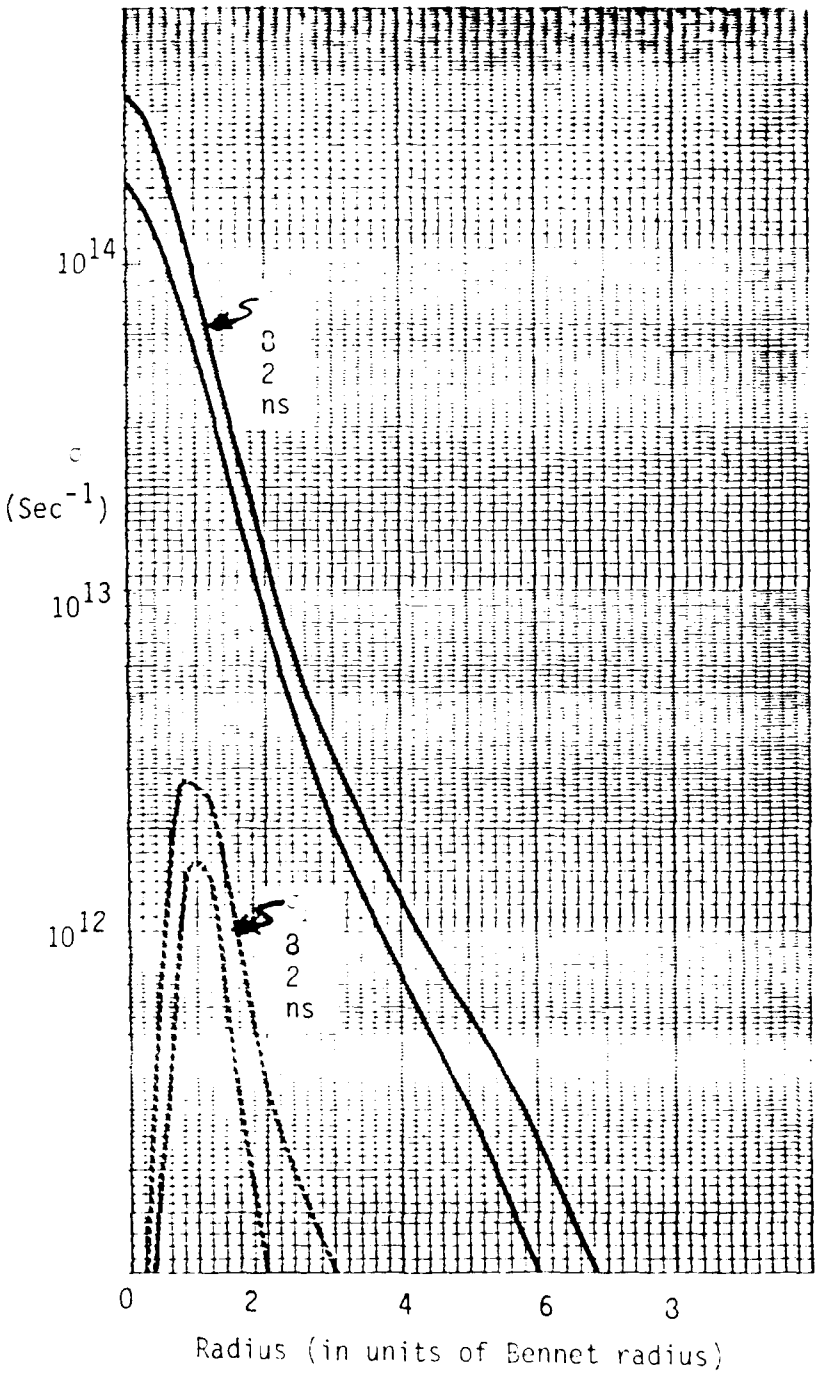

Figure 2.4. Case 3a: (2mm Radius, No Nose) Conductivity at Several Times During the Pulse (Sec^{-1}).

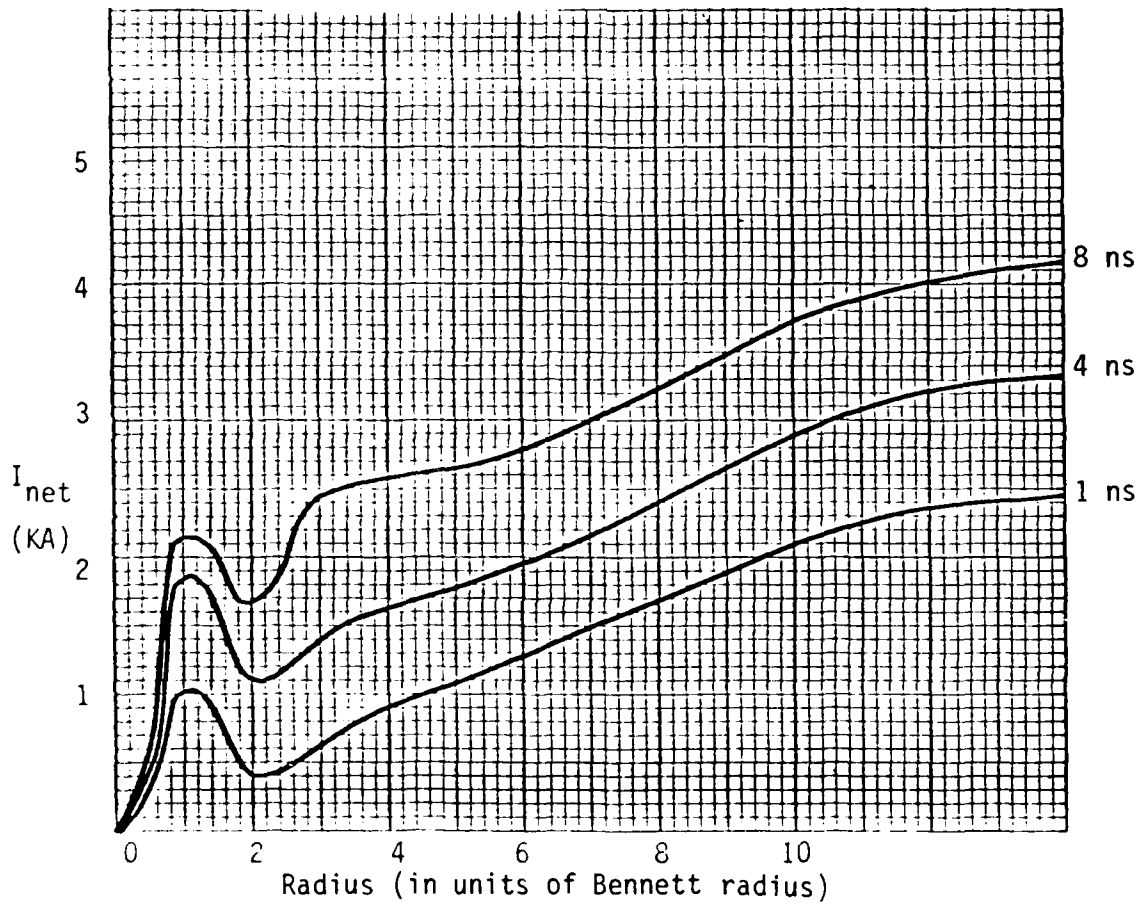

Figure 2.5. Case 3a: (2mm Radius No Nose)
Net current Integrated to Radius r.
$I_{net} = .005\ r\ B(r)$ (kA)

In Case 3b an expanded nose was added to the pulse of Case 3a. This resulted in somewhat earlier development of conductivity in the region outside the beam, but was still insufficient to prevent a high-density plasma current from cancelling much of the beam current.

Case 3a was repeated using the full tensor calculation of $\sigma_\perp$ rather than the simple model. In general this gave slightly larger values of $\sigma_\perp$, but still too small at early times to have any influence on the electric or magnetic fields before $J_r \to 0$. Out to 10 ns the non-cancellation of tensor effects in the more complex theory of the Hall current led to only small deviations from the earlier calculation.

Case 4: 5 mm into 0.1 normal density cold air; mature nose

This case models a very mature nose such as might exist after a considerable amount of erosion has occurred. The full 100 kA is flowing in the expanded region before the pinch-point. This initial broad beam generated before the rapid pinch-down an electron density of $\sim 5 \times 10^{13}$ and conductivity $\sim 5 \times 10^{10}$ sec^{-1} - much broader than the final beam radius of 5 mm. It was a further attempt to get the plasma return current to flow outside the beam. Some redistribution was achieved, as in Case 3b. However, the degree of current neutralization in the core of the pinched beam was not reduced sufficiently for Hall effects to be important in the pinch-down region. To some extent the generation of initial conductivity in the wings is also counterproductive to the generation of Hall effects early in the pulse. This same conductivity which allows the plasma current to move outside also shorts out the Coulomb E_r field, allowing the $J_r \to 0$ condition to be achieved more quickly. As noted before, this works against strong Hall effects.

Case 5: 5 mm beam in 0.1 normal density cold air

An initial electron density profile given by

$$N_e = \frac{10^{12}}{\left|\frac{r}{a_o} - 3\right|^7 + 1}$$

was used to simulate an annular ionized but cold channel provided by a laser. The peak N_e is at 3 Bennett radii from the beam axis, and drops off quickly inside 2 BR and outside 4 BR. This initial seeding with electrons provides a conductivity in the range 10^8-10^9 sec^{-1}, and changes the breakdown characteristics of the channel. However, it did not result in plasma current redistribution sufficient to promote significant Hall effects early in the pulse.

The electron density profile at 0.05 ns is shown in Figure 2.6 for Case 5 (the laser channel) and Case 6 (the hollow beam), along with a comparison profile for the same type of case with no channel or hollowing. For Case 5 the peak electron density on-axis was already three orders of magnitude greater than that in the initial laser channel and the E_r field had already reversed in sign out to $\sim$ 2 Bennett radii. The peak electron density and conductivity occurred at $\sim$ 0.3 Bennett radii, the result of earlier breakdown by the radial Coulomb field. Essentially no net current flowed in the region between 0.5 and 1.2 Bennett radii.

Case 6: 5 mm beam into 0.1 normal density cold air; hollow beam profile

The radial profile of beam current was calculated from

$$J_B = I_B \left[\frac{1+\varepsilon}{\pi a^2} \frac{}{\left(1 + \frac{r^2}{a^2}\right)^2} - \frac{\varepsilon}{\pi b^2} \frac{1}{\left(1 + \frac{r^2}{b^2}\right)^2} \right] \qquad (2.36)$$

instead of the usual Bennett formula. Parameters used were a = 0.5, b = 0.25, ε = 0.32. With this choice, the beam current had a hollowed profile, with the

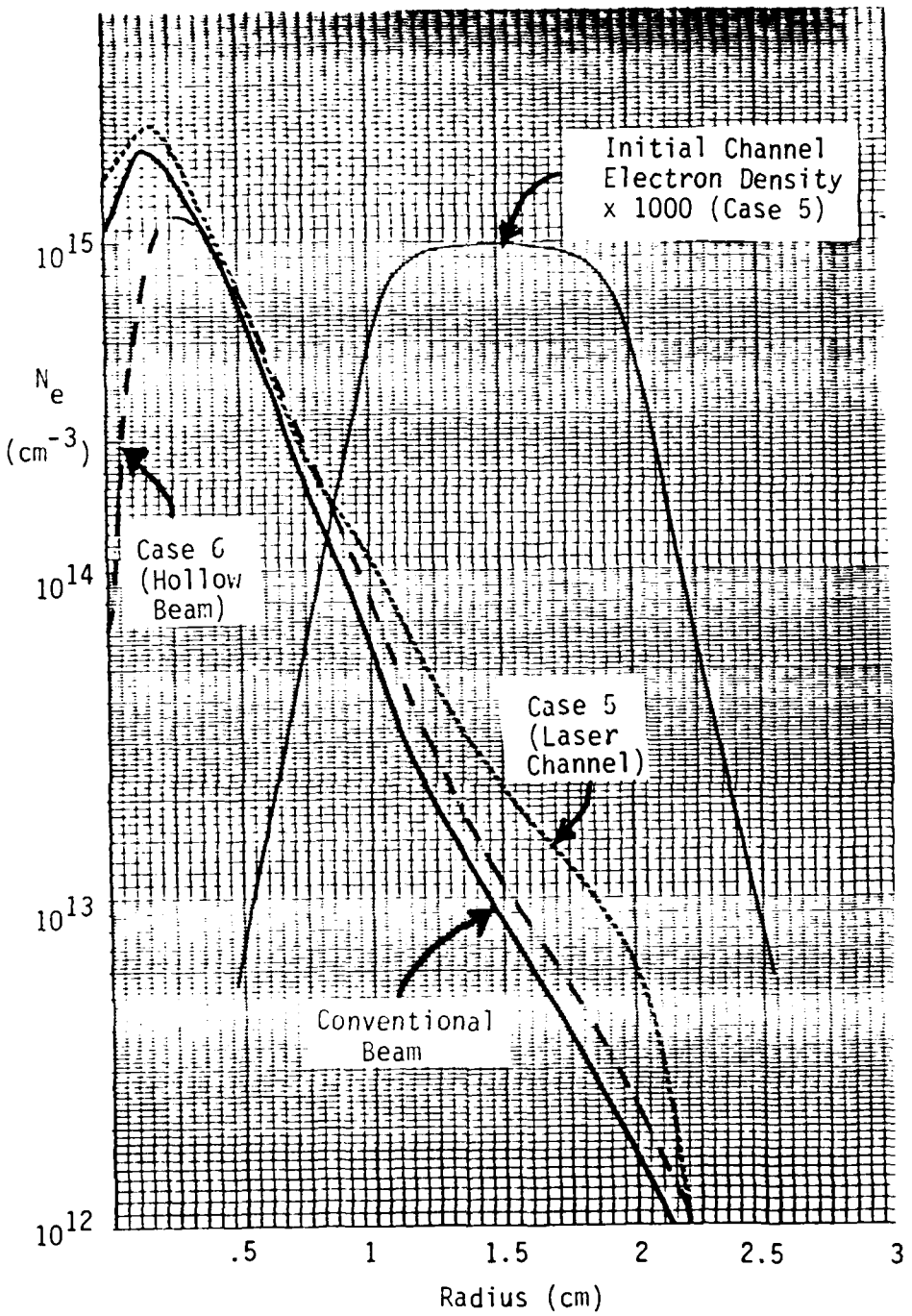

Figure 2.6. Cases 5 and 6: (5mm. Radius No Nose) Electron Density at .05 ns.

axial current density less than 1/10 the peak value which occurred near 0.5 Bennett radii. This profile function was chosen only as a crude representation of what a physical hollow beam profile might be like.

The distribution of plasma current was found to remain very similar to the distribution of beam current up to about 1 ns, with a high degree of current neutralization. By 1 ns the beam current density had reached its peak value, but the plasma current density on-axis continued to grow to about 50% higher than the beam current density; the magnetic field was reversed inside $\sim$ 0.25 Bennett radii. The conductivity profile remained peaked off-axis through the 10 ns of the calculation. The net current integrated out to large radius was a few percent higher than that for Case 5 at 10 ns, but a factor of about 2 lower than for Case 4. As in those cases, there was no significant difference between the tensor and scalar calculations.

Case 7: 2 mm into uniform low density channel; artifically-imposed conductivity profile

The purpose of this calculation was to assess the sensitivity of the electromagnetic fields to an artifically-imposed conductivity profile. This was done by decoupling the conductivity calculation completely from the fields. The beam current was calculated as described by Eq. (2.34) above, and the conductivity on-axis was simply chosen to be proportional to the beam current, with a peak value of 10^{14} sec^{-1} at I = 100 kA. (a) σ_o has a radial profile which is the square root of the Bennett beam profile and (b) σ_o has a radial profile the same as the beam current. The ratio σ/σ_o, and σ itself, were computed according to the simple Hall theory described above. The collision frequency ν_m was chosen to represent a uniform low density region with $\sim$ 0.036 of normal air density.

Tensor and scalar results for the two different profiles are shown in Figure 2.7. The axial electric field and axial plasma current density are shown. For the Bennett profile case, the beam current is very highly neutralized; the tensor and scalar results are virtually identical out to 20 ns. On the other hand, for the flatter conductivity profile, a significant reduction in E_z and plasma current occurred in the tensor case beyond 1 ns.

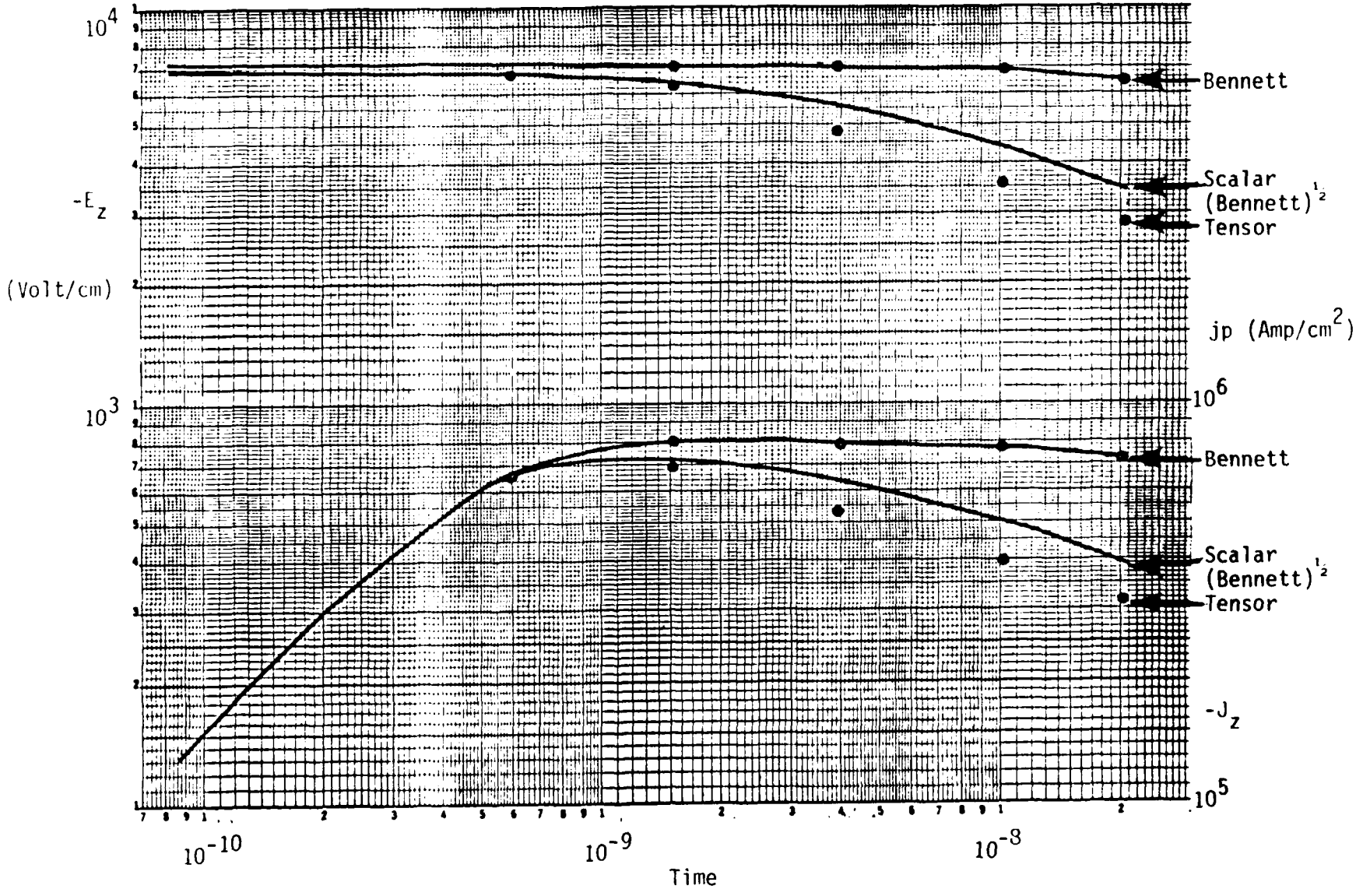

Figure 2.7. Electric Field and Plasma Current Density for Case 7 (Artificial Conductivity Profiles).

2.5 Conclusions

From the local conductivity studies described in this section, several conclusions emerge.

(1) In order for Hall effect to radially redistribute the plsams currents it is necessary that $\alpha \equiv (\omega_L/\nu_m)$ become significant very early in the pulse before the radial Coulomb field reverses and J_r vanishes, typically within the first few tenths of a nanosecond. If this condition can be achieved, on-axis plasma current decreases, net current increases, α increases, and the effect feeds on itself.

(2) At low gas density, ν_m decreases, but so does the net current-decreasing α. Faster avalanche breakdown or ambient ionization result in J_r tending to zero earlier in the pulse, allowing less time for Hall effect to act.

(3) The strong non-linearity of the field equations - including Hall terms - requires great care for their stable solution.

(4) To date, we have numerically studied a range of "realistic" cases, with conductivity evaluated self-consistently with the fields but always assuming <u>local</u> conductivity generation. In all these cases, the race is lost; current neutralization occurs so fast that α never becomes significant until well into the body of the pulse when Hall effects essentially cancel.

Critical to all these results is the conductivity and plasma response to the beam during the first few tenths of nanoseconds - a time-scale for which our local, instantaneous conductivity modelling is not appropriate, especially at low densities. More adequate non-local conductivity models are described in the next section.

3.0 NON-LOCAL CONDUCTIVITY EFFECTS

3.1 Introduction

This section summarizes results from an initial, simple non-local, non-Ohmic air chemistry model - including Hall effects and their impact on beam stability.

In Section 3.2 the results of modelling high current beams in low-density air are discussed. At low-densities, the standard simplifying assumptions usually employed in conductivity modelling no longer apply: scalar conductivity, Ohm's law; local-instantaneous energy deposition; Maxwellian distributed plasma electrons; no delta rays; and no inertial effects. These assumptions are <u>not</u> made in the present model. It is concluded that Hall currents do play a significant role at low enough densities and that the redistribution of plasma current can result in a significant but sudden increase in the magnetic pinch below a "critical" air density. The conductivity model described here is a simpified version of the LOCOND model described elsewhere (Ref. 7) and has been developed as an intermediate step toward a truly simple model for inclusion in beam stability codes.

3.2 High Current Beams in Low Density Air

3.2.1 Introduction

We report here the results of applying a phenomenological low-density chemistry code to high current beams. A brief account of the model has been given previously (Refs. 8 and 9). However, substantial modifications were necessary for application to high current beams. The model is not considered complete, and there are no independent calculations in the same parameter regime to which it can be compared; thus, the quantitative results are tentative.

Conclusions based on the calculations are:

1) Below a certain model-dependent density $\sim$ .01 normal, the electric field drives a bulk runaway which changes the distribution of plasma currents. The net result is a sudden significant increase in the pinch force as the density is decreased below the critical value.

2) If Hall currents are turned off, the enhanced pinch may be reduced by as much as a factor of two at one Bennett radius.

3) Significant amounts of plasma current are driven by the gradient in electron pressure.

4) Significant amounts of plasma current are carried by the high-energy non-Maxwellian part of the electron distribution.

This section is divided into three main topics: (1) a discussion of the physics requirements for low-density calculations, (2) an outline of the present status of the model, and (3) a discussion of the computational results for high current beams.

3.2.2 Beam-Driven Chemistry in the Low-Density Regime

Simple order-of-magnitude argments show that at background densities sufficiently lower than normal atmospheric density, several key assumptions built into standard beam chemistry codes are not justified. Among these inapplicable assumptions are:

1) The beam-initiated cascade results in local, instantaneous production of electrons and ions.

2) Currents associated with the cascade itself can be neglected.

3) Plasma currents can be calculated from Ohm's law.

4) The electron and ion densities are always almost equal, so transport effects can be ignored in the chemistry calculations.

5) The electron distribution remains close to Maxwellian, so that the high energy parts of the distribution are no more important than usual in determining currents, ionization rates, etc.

In addition, many beam chemistry codes use electromagnetic algorithms which ignore Hall current effects. This assumption can break down in two ways at low density: (a) the momentum transfer frequency goes down with the density, so that it may not exceed the Larmor frequency by a wide margin as in full-density air, and (b) the highly-overpopulated high energy tail of the electron distribution at low density may have a momentum transfer frequency considerably lower than that of the bulk of electrons, and thus make a larger contribution to the current.

In Section 2, we have investigated the effects of Hall currents in full and reduced density air, but did not address problem (b) above. In addition, we have made assumptions 1 - 5 in our chemistry codes. We have recently developed a multi-energy-group model which abandons assumptions 1 - 5 and addresses the non-Maxwellian aspects of Hall current calculations (Ref. 7). Recent calculations by Yu (Ref. 12) have confirmed the importance of Hall current effects for ATA-like beams when the electron energy distribution is treated in detail. The present work verifies their importance for high current beams.

3.2.3 Non-Local, Non-Ohmic Conductivity Model

The ultimate goal of the development program is to produce a relatively simple BMCOND-like model which can be incorporated into propagation codes. This requirement eliminates the possibility of doing a "first principles" calculation. The approach taken is to develop a phenomenological model which represents the most important physical processes in a simple way, and to adjust the "free" parameters associated with various simplifying assumptions to obtain agreement with more fundamentally-based calculations.

The model described below considers the electron distribution broken into three energy ranges. The lowest energy group represents basically the usual bulk of approximately-Maxwellian electrons. The next higher energy group represents those that in the presence of an electric field are in the runaway regime and thus behave very differently from the bulk of the electrons. The third group represents the relativistic particles produced directly by the beam.

The organization of the model is summarized in Fig. 3.1, in which the sources and sinks of particles for each group are shown schematically. The three energy ranges will be referred to by the names low-group, high-group, and δ-group, in order of increasing energy. The beam particles themselves constitute a fourth group which is treated in the usual way (e.g., no energy straggling).

The beam particles collisionally produce secondaries directly in each of the three groups, according to a Moller distribution (modified at low energy). The maximum δ-ray energy is one-half the beam energy, since the higher energy particle emerging from a primary interaction remains associated with the beam. Collisions by beam particles are the only source of electrons in the δ-group. A more detailed discussion of the δ-ray model is given below in Section 3.2.3.1.

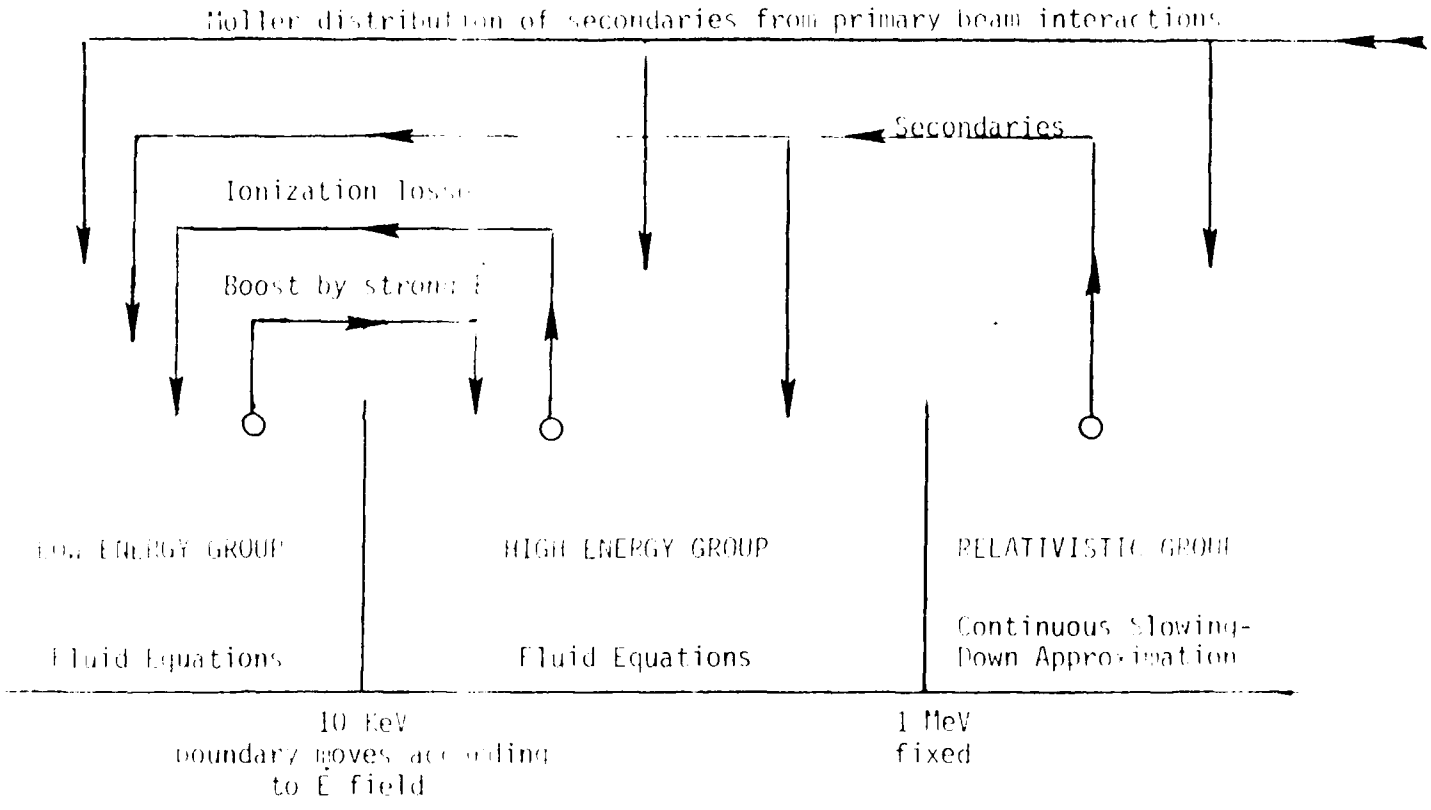

Figure 3.1. 3-Group Model.

The high-energy group extends downward from 1 MeV to a variable-energy boundary which at present goes no higher than 10 KeV. It is fed mainly by primary beam collisions and by the collisional degradation of the δ-group through its 1 MeV lower boundary. Under some conditions, electrons are also transferred up from the low group.

Both the high and low energy electron groups are represented by fluid equations for particle density, momentum and energy. The equations of motion provide the means for abandoning the ohmic representation of plasma current flow. The fluid equations are solved on an Eulerian grid which is the same grid used for the electromagnetic field calculation. It is assumed that everything is a function of the "retarded" time variable $\xi \equiv t - z/c$ only, so that the only independent variables are r, the radial position, and ξ, the distance back from the pulse head in seconds. The electromagnetic fields are obtained using the algorithm described in Section 2.

In principle it is necessary to solve the fluid equations and δ-group equations simultaneously with the electromagnetic field equations. Since the Maxwell equations themselves are explicitly non-linear when the Hall current terms are included and the fluid equations are also non-linear, an iterative procedure is required. In order to maintain maximum modularity under these circumstances, the procedure adopted involved solving first a linearized set of fluid equations, followed by the field equations, and then iterating to convergence.

In addition, the algorithm has been designed to allow differential comparisons between the three-group model and a model with the high energy and δ-groups eliminated and with the standard local-instantaneous approximations made. However, this latter "one-group model" still differs from standard chemistry codes in that it solves an equation of motion for the one group rather than using Ohm's law. It is also possible to turn off the pressure terms in the equations of motion and the Hall current effects.

3.2.3.1 Delta-Ray Group

In the present discussion, δ-rays will refer to the part of the beam-initiated cascade which has energy greater than 1 MeV. These particles are represented by a model essentially identical to that developed by Johnston (Refs. 7, 11). As applied here, the model has two main deficiencies: (1) it does not provide detailed information on the radial distribution and (2) it does not include the detailed effects of electric or magnetic fields on the δ-particles. With the assumption that everything depends on $\xi \equiv t - z/c$, the model gives an integral expression for the total δ-ray current as a function of distance ξ back from the beam head. (Particle energy distribution information is available but not used at present.)

It is assumed that most of the particles produced as secondaries by the δ-rays have very low energy. This is consistent with the continuous slowing down approximation which forms the basis of the model. In the present model, as the δ-rays lose energy, they produce low energy electrons at a rate of one particle per 33.73 eV of energy lost; these particles immediately enter the low-energy plasma electron group of the three-group model. The δ-rays themselves degrade in energy due to collisions. They reach the cutoff of 1 MeV at a rate given by the Johnston model, and at this point they are added to the high energy electron group.

The radial profile as a function of distance back from the beam head is estimated in a crude way, based on two pieces of information: (1) the δ's are produced with the beam profile and (2) they evolve from that profile to form a halo with radial dimension estimated by Johnston (Ref. 11) to be ~ 4 Bennett radii about a Bennett-profile beam (for particles above 1 MeV). It is assumed that at a given ξ, the profile towards which the δ's evolve is a weighted average of the beam profile and a specified halo profile. The relative weights are determined from the rate of local production as compared to the total instantaneous number density, and the rate of evolution towards the halo profile. This assumption is used in the following interpolation formula for the radial profile $f(r, \xi+\Delta\xi)$ in terms of $f(r, \xi)$:

$$f(r, \xi+\Delta\xi) = (f(r,\xi) + \Delta\xi F)/(1 + \nu_d \Delta\xi).$$

The function F is given by

$$F = (\frac{S}{N} h + g \nu),$$

where S is the local rate of δ-ray production by the beam, N is the total number of δ-rays present, and h is the beam profile, from which the δ-rays are produced. The profile g is the assumed halo profile, and ν is a characteristic rate at which the δ's evolve towards the profile g. The rate ν_d is set equal to S/N + ν. With this choice, $f(r,\xi+\Delta\xi)$ is normalized to unity if h, g, and $f(r,\xi)$ are. The rate ν is taken to be an average radial velocity of the δ's divided by the assumed halo characteristic radius.

3.2.3.2 The High-Energy Group

The schematic forms of the fluid equations for the high-group are:

$$\frac{\partial N}{\partial t} + \nabla\cdot(N\vec{v}) + \nu_1 N = S_B + S_\delta + S_L \qquad (3.1)$$

$$\frac{\partial \vec{J}}{\partial t} + \nabla\cdot(\vec{J}\vec{v}) + \frac{1}{m}\nabla P + \nu_2 \vec{J} = \vec{K}_B + \vec{K}_\delta + \vec{K}_L + \frac{Ne}{m}(\vec{E} + \frac{\vec{v}}{c}\times\vec{B}) \qquad (3.2)$$

$$\frac{\partial}{\partial t}(\frac{1}{2} Nmv^2 + \frac{3}{2} P) + \nabla\cdot[\vec{v}(\frac{1}{2} Nmv^2 + \frac{3}{2} P)] + \nabla\cdot(\vec{v}P) + \nu_1(\frac{1}{2} Nmv^2 + \frac{3}{2} P) = L + Ne\vec{E}\cdot\vec{v} \qquad (3.3)$$

The terms S_B, $\vec{K}_B$, etc. are the sources due to the beam, the δ-group, and upward transfer from the low-group, respectively. It is assumed that all collisional ionizations by high-group electrons produce a low energy secondary which goes directly into the low group. The energy equation (3.3) has been written with the total energy split into a drift part and a thermal part, represented by a pressure P. The term L includes energy deposited by the beam, energy brought in by transfer of particles from the low-group and δ-group, and energy losses due to ionization. Energy loss due to loss of particles from the high group is

represented by the ν_1 term on the left side of the equation. It has been assumed that the particles lost take with them the average energy of the high group. The momentum loss rate ν_2 includes the effect of particle losses, momentum loss due to ionizing collisions, and momentum loss due to elastic collisions.

The fluid equations are solved as a finite difference system on the Eulerian electromagnetic field grid. The outer boundary condition allows an outflow of particles. No explicit assumption is made concerning the distribution function of the high group electrons except at $\xi = 0^+$, when it is dominated by the Moller distribution from primary beam particle interactions. The average total energy and z-momentum are then used to give an initial "temperature" T, defined by P = NT, where P is the pressure from Eq. (3.3). At all subsequent times, the temperature, particle density, and drift velocity are obtained from the fluid equations.

For simplicity, ionization and momentum transfer rates are evaluated at the mean particle energy. An analytic formula given by Briggs and Yu (Ref. 12) is used for the ionization cross section. The momentum transfer frequency ν_m is given by the approximate formula

$$\nu_m = (1.08 \times 10^{-5} N_g \mathcal{E}^{1/2})/(178.89 + \mathcal{E}^{3/2}) + (1.46 \times 10^{-6} N^+ \log \Lambda)/T_{equiv}^{3/2} \qquad (3.4)$$

where $\mathcal{E}$ is the total electron energy in eV. The first term represents the effect of collisions with neutral particles and the second represents Coulomb collisions. The "equivalent" temperature is defined as $T_{equiv} = T + 1/3\ mv^2$, $\log \Lambda$ is the usual Coulomb logarithm, N_g is the total density of neutral atoms and molecules, and N^+ is the total density of positive ions.

The boundary between the high and low energy groups is set by finding the solution of the equation

$$e E = m \nu_m \bar{v} \qquad (3.5)$$

corresponding to the high energy side of the peak in ν_m. The average velocity $\bar{v}$ is related to the total energy $\mathcal{E}$ appearing in Eq. (2.4) by $\mathcal{E} = \frac{1}{2} m \bar{v}^2$. However, the boundary energy is not allowed to exceed 10 KeV even when the total electric field E is very small.

Another special case occurs when the field is so strong that there is no physical solution to (3.5); this corresponds to a bulk runaway, in which the field is capable of accelerating the electrons through the peak of the momentum transfer cross section. In this case, the choice of the lower boundary of the high group is somewhat arbitrary. The lower limit to be used for the boundary during a strong runaway condition can be specified as input data. Usually it is taken to be a few volts, so that essentially all the electrons produced directly by the beam go into the low end of the high energy group. The transfer of electrons from the low to the high group is discussed below.

3.2.3.3 The Low-Energy Group

The equations for the low energy group are similar in form to those given above for the high group with the exception that they contain loss terms due to recombination and to transfers to the high energy group, and input terms due to transfers from the high group and to collisional ionization by high group electrons. The main difference in the treatment of the low group is in the chemistry detail. At present, the abundance of N_2, O_2, N, $N(^2D)$, O, and a composite representative of the triplet states of N_2 are followed explicitly by differential equations. The system of equations used is essentially the same as in the chemistry code BMCOND (Ref. 13). This degree of complexity was found necessary to obtain reasonable agreement with the comprehensive code HICHEM at low air densities for high current calculations.

Ionization rates are given by tables identical to those in the HICHEM code up to 500 volts "equivalent" temperature ($T_{equiv} \equiv T_e + 1/3\ m\ v^2$). The collisional excitation rates from the BMCOND model are used. Ionization and excitation rates due to the beam are computed as in the HICHEM code, but with appropriate adjustment for the differences between time-delayed deposition model used here and the instantaneous deposition model in HICHEM and BMCOND.

It is very important to distinguish between the positive ion density and the electron density, since electron transport effects can be very large; thus a separate differential equation for the total rate of positive ion production is integrated. In addition it was found necessary to calculate a vibrational temperature because of significant sensitivity of computational results to the dissociative recombination rate; the HICHEM treatment was adopted for this calculation. The momentum transfer frequency used in BMCOND is used for low energies, with a smooth transition to the analytic formula (Eq. 3.4) used for the high group. The Coulomb term of Eq. (3.4) is used throughout.

Reassignment of electrons from the low group to the high group is a relatively arbitrary procedure. The goal is to remove electrons from a presumed high-energy non-Maxwellian tail of the low group and put them into the high group, which hopefully represents better their contribution to currents, ionization rates, etc. than does the assumed Maxwellian bulk of the low group electrons. However, there is no simple model of the super-thermal tail as generated by strong electric fields which vary rapidly in both time and space. Several different ad hoc procedures have been tried, but none is especially defensible in detail.

Qualitatively, what happens in a weak field (or high ambient density gas) is not very sensitive to the details of the transfer rate. Under strong runaway conditions, the entire low group is accelerated to high drift energy and heated to temperatures $\sim$ kilovolts on a very short timescale. During this time, the distinction between the two groups is not very meaningful, and again the behavior of the bulk plasma is not too sensitive to the details of the transfer

rate. However, after the fields which precipitate a strong runaway die out, the distribution of electrons between the two groups can be important; this does depend strongly on the transfer rate. Similarly, if conditions for a strong runaway are just barely achieved for only a short time, there may be some sensitivity to the transfer rate. These problems are continually being studied, both in the context of the model described here and through comparison with other, more comprehensive models being developed.

The transfer rate presently used is calculated as follows. A velocity v_o is defined by $v_o = \pm v_r + .5\ V_t$, where the + sign is taken if the radial drift velocity is parallel to E_r, and a negative sign is taken if it is opposed. The thermal velocity term V_t is added to account for the fact that, at high enough temperature, a substantial number of electrons may be able to run away even if the bulk drift is not large (or even parallel to the E_r field). The transfer rate of electrons is then given by

$$S_L = \min(.5,\ .1N_h/N_e)\ \min(1.,\ \exp(\frac{v_o - v_c}{V_t}))/\Delta\xi, \qquad (3.6)$$

in which v_c is the velocity corresponding to the energy boundary between the groups, N_h is the local density of high-group electrons, N_e is the local density of low-group electrons, and $\Delta\xi$ is the proposed timestep. The purpose of the first minimum function is to assure that the high-group density is not changed by more than 10 during the step. In actual computations, the transfer rate is usually very low, or else as high as permitted by the first factor of (3.6), even for exceedingly small timesteps.

The momentum transferred with the particle is taken to be parallel to its total drift velocity, with magnitude given by the larger of the velocities v_o and v_c. The energy transferred is the average energy per particle of the low group, plus an additional amount arranged to come (by suitable terms in the equations of motion) entirely from the drift energy of the low group, to make up the total drift energy of the electron injected into the high group.

The net result is to decrease the drift energy of the low group but leave its temperature unchanged. The effect of the energy and momentum transfers on the high group depends on its energy and momentum at the time of the transfer. Other procedures for transferring electrons to the high group are being evaluated.

3.2.4 Calibration in the High Current Regime

At present there are no comprehensive, first-principle calculations to provide detailed guidance in the development of the three-group model for high current calculations. Yu (Ref. 10) has presented Boltzmann-code calculations for ATA-like parameters, but even these calculations incorporate assumptions which are not always justified in the context of high power beam plasmas. The purpose of the calibration runs discussed below is to check that the relatively simple model described in Section 3.2.3 agrees reasonably well with detailed chemistry codes in regimes where the assumptions of those codes (see Section 3.2.2) are not thought to be seriously in error. Results of calibration at 10 kA have been presented elsewhere (Ref. 8). A similar comparison with the HICHEM (Ref. 4) code at 100 kA and gas density 0.1 normal is given below. The rise time is 5 ns and the Bennett radius is 0.5 cm.

The comparison of electron densities on-axis and at one Bennett radius is shown in Figure 3.2. The agreement is very satisfactory. The effect on the electron density due to the time delay for the three-group model is not large after 2 or 3 ns. The electron density on axis is mainly determined by the close balance between collisional ionization and dissociative recombination after a few ns. The recombination rate itself decreases significantly as the molecules (and molecular ions) are depleted, and as the vibrational temperature increases. After about 6 ns, the continued increase in N_e is determined mainly by the decrease in the recombination rate, with a large part attributable to the vibrational temperature dependence.

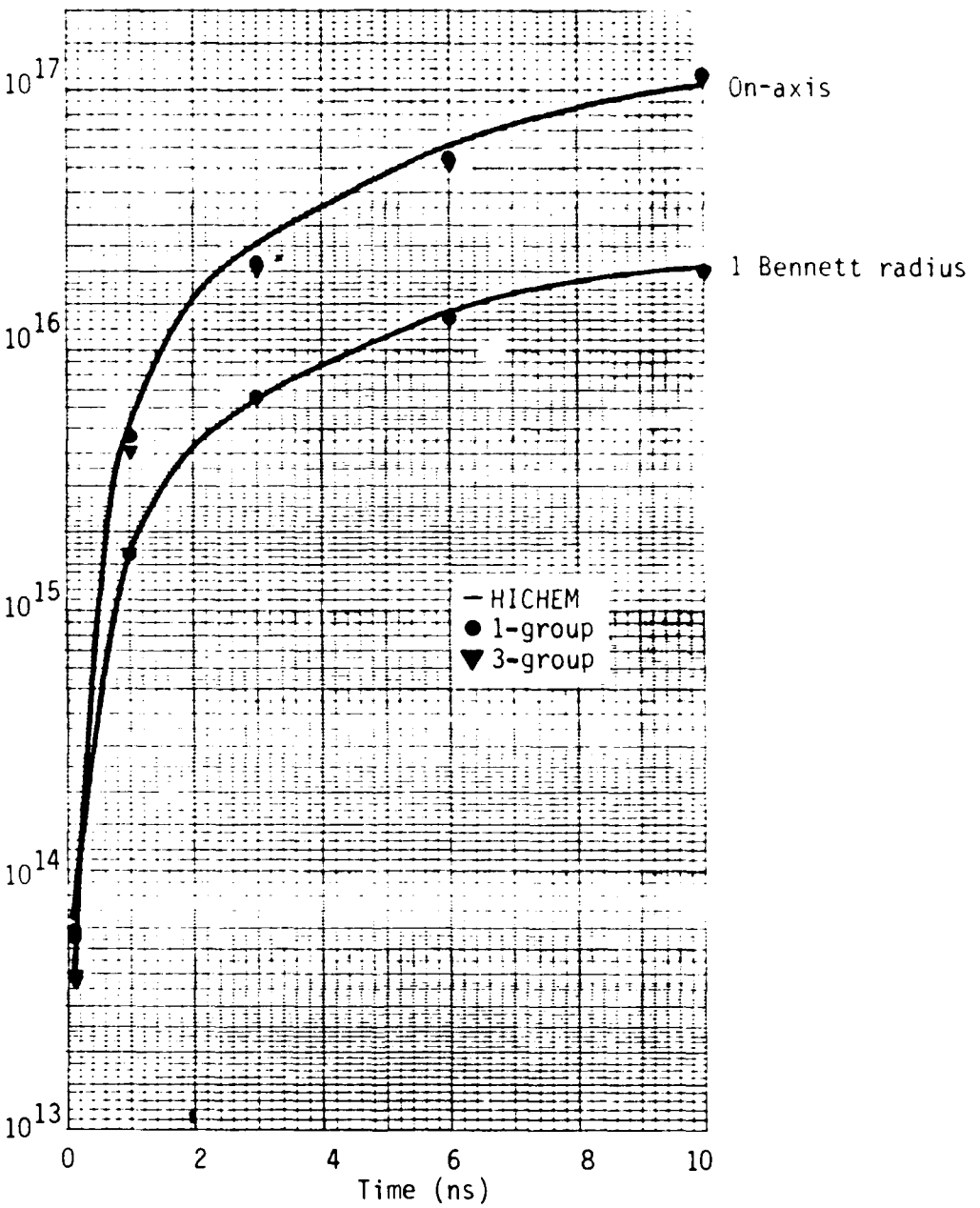

Figure 3.2. Electron Density Comparison at $r/r_0 = 0.1$. 100 kA, 0.5 cm beam radius, 5 nsec current rise time.

A similar comparison of electron temperatures and total currents is shown in Figure 3.3. The temperature agreement is quite good from 1 ns on. At 0.1 ns, HICHEM gives $T_e \sim 18$ volts, compared to the 12 or 13 volts given by the simple models. At such early times the ohmic approximation used in HICHEM is not very good, so the ohmic heating rate is likely to be incorrect; thus it is not clear which values are closer to the truth.

As in the 10 kA comparison (Ref. 8), the agreement between HICHEM and the simple models is not as good for the net current and effective current. This difference is mainly due to the difficulty in matching the momentum transfer frequency calculated in HICHEM by a very simple formula. However, the agreement in currents is still acceptable, particularly since the most interesting sensitivities described below develop before 1 nsec.

Because the results of the HICHEM code are suspect below $\rho/\rho_0 \sim 0.1$, especially for $\xi <$ few ns, it cannot be used for calibration comparisons at lower densities. However, many of the results presented below are differential comparisons or sensitivity studies, and thus can provide useful information in spite of uncertainties in the quantitative results.

3.2.5 Computational Results

3.2.5.1 Introduction

The beam parameters for the calculations described below are:

Current	=	100 kA
Rise time	=	5 ns
Bennett radius	=	0.5 cm
Energy	=	10 MeV

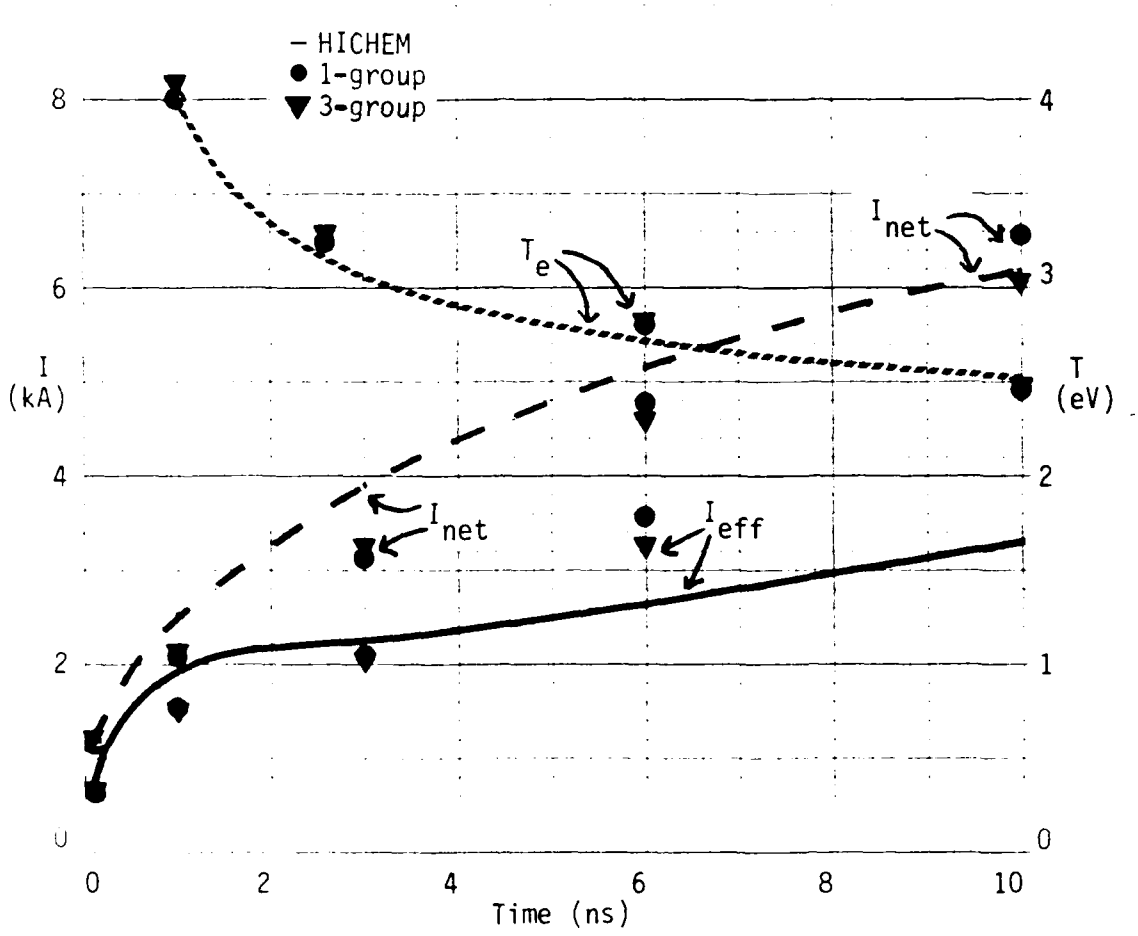

Figure 3.3. Axial Temperature and Current Comparison at ρ/ρ_o = 0.1.

The discussion below is divided into two main sections. The sensitivities to gas density, Hall currents, and pressure terms are described briefly in Section 3.2.5.2, and the remaining sections discuss the calculationa in more detail.

The main conclusions have been stated earlier (Section 3.2.1). In brief, it has been found that the pinch force is strongly dependent on the gas density below some threshold value, and significantly dependent on the presence of Hall currents and pressure terms. The plasma current and electron density radial distributions change dramatically over a very small range of density ratio near $\rho/\rho_0 = .01$, resulting in an increase of pinch force by a factor of 3 or more for a density change of only $\sim$ 20%.

3.2.5.2 Sensitivity Results

Density Sensitivity of Pinch Force

The dependence of $I_{eff}(r)$ on ρ/ρ_0 is shown in Figure 3.4 for the three-group model, and in Figure 3.5 for the one-group model. The sharp onset of current enhancement begins in the range $\rho/\rho_0 \sim .0085$ - .01 for the three-group model, and between .005 - .008 for the one-group model. In both cases, the current enhancement is a factor $\sim$ 3.5 or greater, compared with a base level at $\rho/\rho_0 \sim .01$. These large effects set in when the plasma electrons can be sustained in a state of bulk runaway for several tenths of a nanosecond.

The sharp density threshold results from the sensitivity of the charge neutralization process to gas density. Several effects contribute. The beam production of positive ions is directly proportional to the density; the electrons produced by the beam provide "seed" for the avalanche process of plasma electron collisions. The peak e-folding rate of the avalanche is also proportional to the density. These two processes clearly delay the charge neutralization as the gas density is decreased and allow higher radial electric fields to develop (assuming the rise time is not $\sim$ 1 ns). In order for

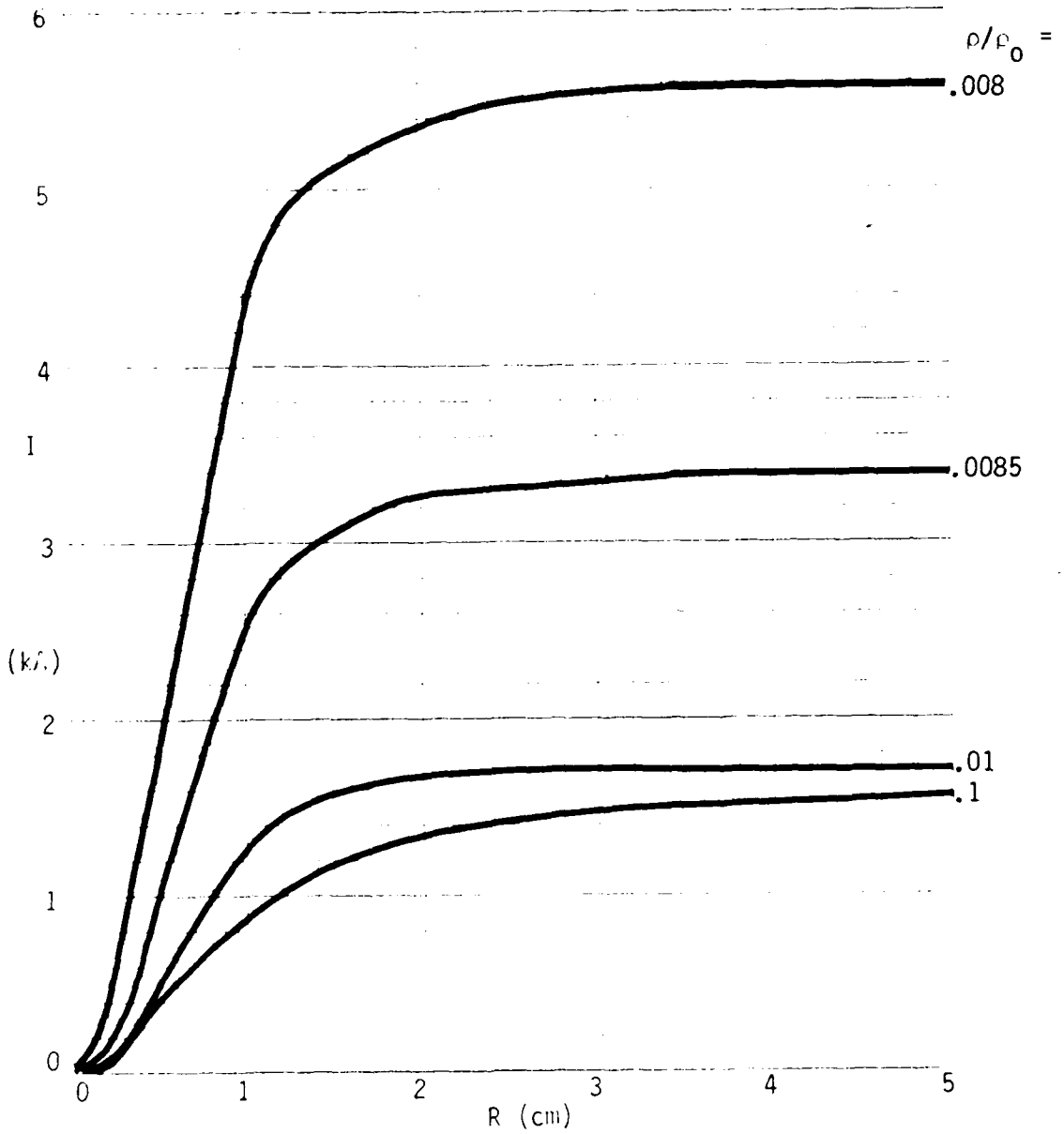

Figure 3.4. I_{eff} Dependence on ρ/ρ_0 at 1 ns (3-Group Model).

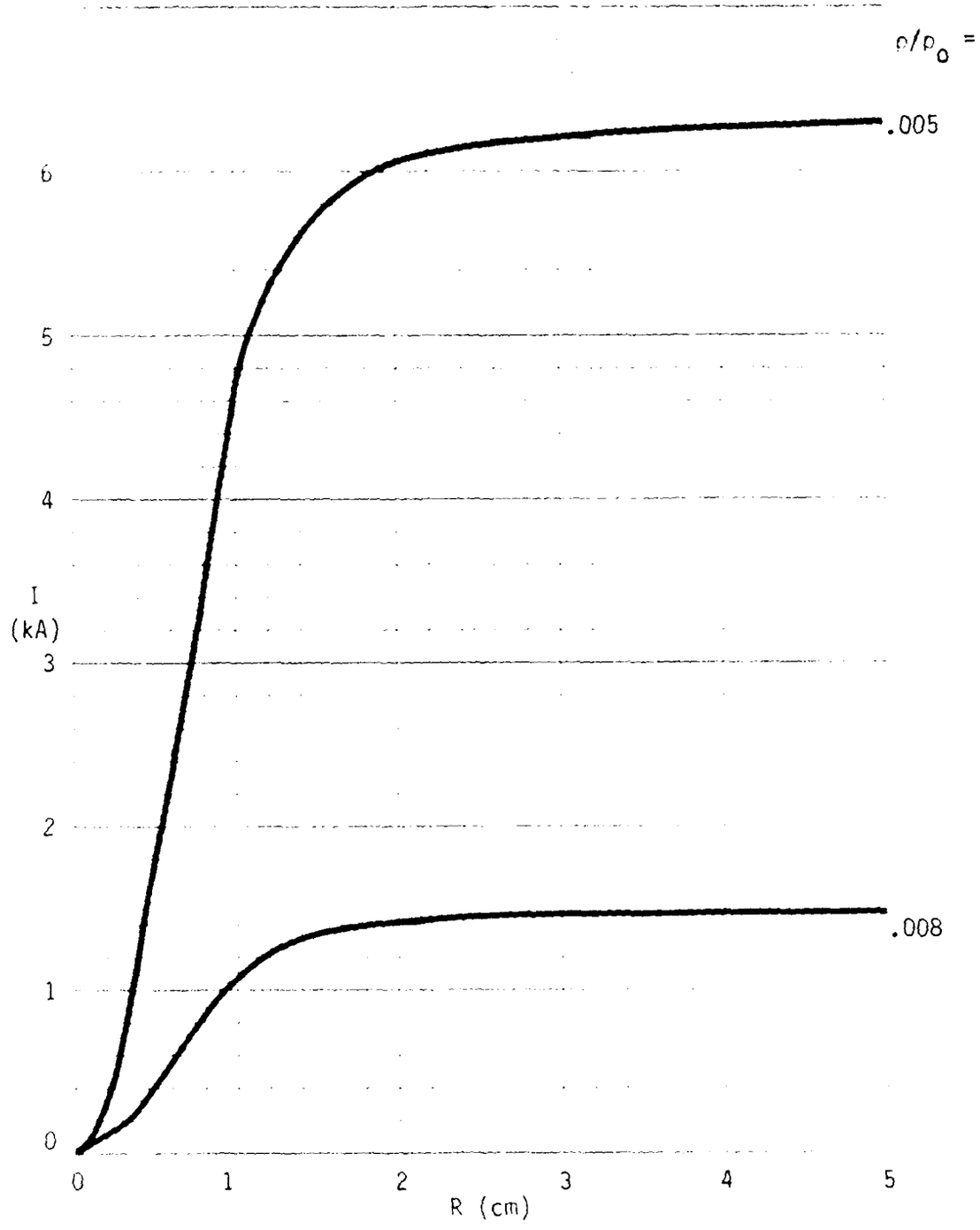

Figure 3.5. I_{eff} Dependence on ρ/ρ_0 at 1 ns (1-Group Model).

neutralization to occur, plasma electrons produced by various processes must move out of the spatial region occupied by the beam, leaving the positive ions to cancel the charge of the beam particles. Higher fields help move the electrons out quickly, but that process dilutes very considerably the avalanche ionization and thus slows the production of the needed positive ions close to the beam axis. In the true IF regime, avalanche is relatively unimportant, and the accumulation rate of beam-generated positive ions determines the neutralization time and the peak fields.

The difference in density threshold between the two models is caused by (1) the time-delay in ionization in the three-group model which reduces the effective beam ionization rate by more than a factor of two; and (2) the effects of the non-Maxwellian high-energy group on the ionization rate and on the movement of plasma electrons away from the beam. It is difficult to assess these separately because beam production of the high-energy and δ-ray groups (which degrade relatively slowly at low densities) is the cause of the time delay. Since qualitatively-similar results occur whether or not the high-energy group is included, it seems that the time-delay is probably most directly responsible.

Sensitivity to Hall Currents and Electron Pressure

The radial pressure gradient in the equations of motion for the high and low energy electrons can drive currents both radially and in the z-direction due to the magnetic part of the Lorentz force (Hall effect). This works in conjunction with the electrically driven currents. The result of deleting either the pressure terms or all Hall effects (by zeroing the magnetic force on the plasma electrons) is shown in Figure 3.6. Clearly, the Hall currents have the largest effect, but the pressure terms are not negligible either. Note that these comparisons show the cumulative effect of removing the terms for the entire calculation, and not simply the contributions to the current at the time shown. A similar calculation was done with only the high group

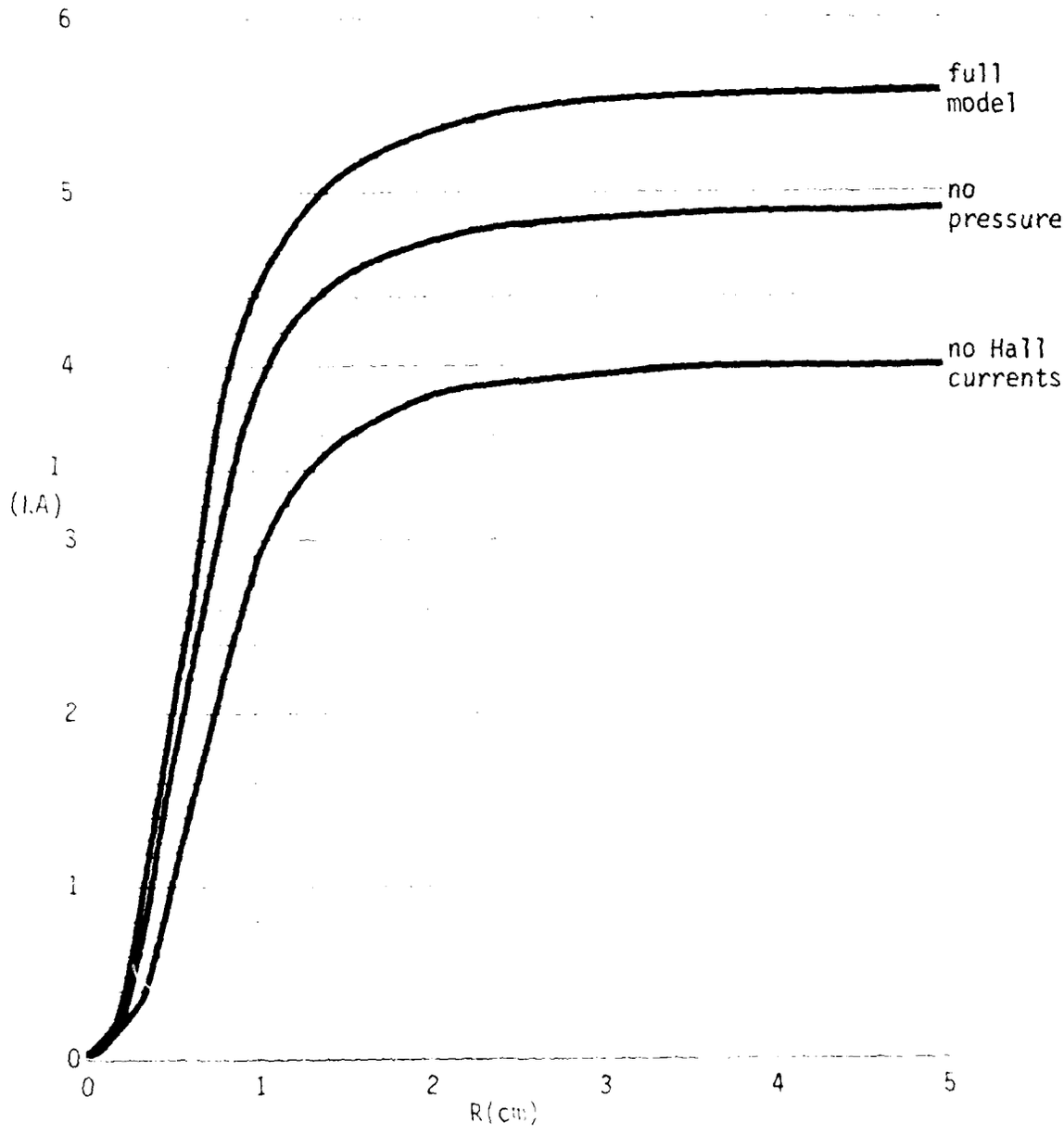

Figure 3.6. I_{eff} at 1 ns with Δ/Δ_0 = .008 (3-Group Model).

pressure turned off. The effect at ξ = 1 ns was considerably smaller than shown in the figure. Low-group pressure contributes dominantly during the bulk runaway because the electrons reach temperatures in excess of a kilovolt and their number density is large. However, it will be shown in later discussion that the high-group pressure-driven Hall current is important.

3.2.5.3 Comparison of 1-Group and 3-Group Calculations at ρ/ρ_0 = .008

The purpose of the following discussion is to provide a more detailed description of the phenomena which lead to the enhanced pinch force. At ρ/ρ_0 = .008, the 3-group model shows a very strong effect, whereas the 1-group model shows very little because its density threshold is somewhat lower.

Effects on Plasma Current Distribution

The net current (including displacement) integrated out to radius r is given by I_{net} = .005 r B(r), where I is in kA, B is in gauss, and r is in cm. The effective current, which measures the pinch force, is the beam-profile-weighted average of .01 r (B(r) - E_r(r)). The value of the effective current integral taken to radius r, and the net current, are shown in Figures 3.7(a) - (h) at various distances from the pulse head. Large differences are apparent by 1 ns and persist to 10 ns.

At 0.1 ns, the net currents for the two calculations are similar, but the effective current is substantially weaker for the 3-group case because the radial electric field is higher (due to slower charge neutralization).

At 1 ns the effective current in the 3-group model is $\sim$ 28% of the beam current at that time, whereas in the 1-group model it is only $\sim$ 7.5%. The net current profiles imply a very much broader plasma current distribution for the 3-group model, although net currents inside 5 cm radius (10 Bennett radii) are $\sim$ .5 to 1 kA in both cases even at 10 ns into the pulse where the beam current is almost 100 kA.

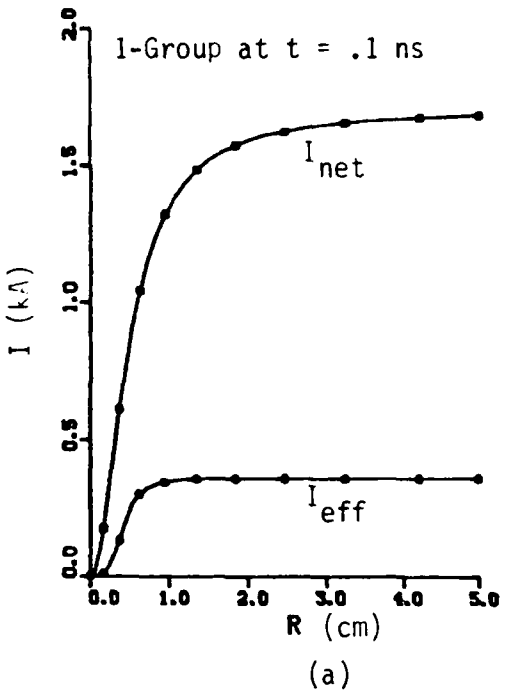

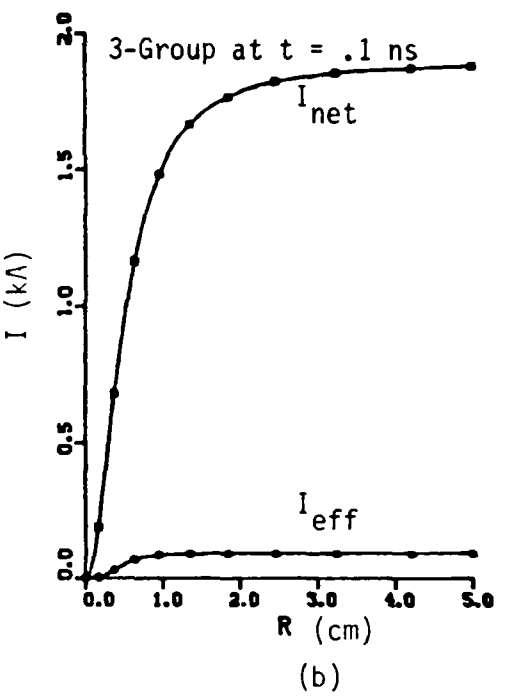

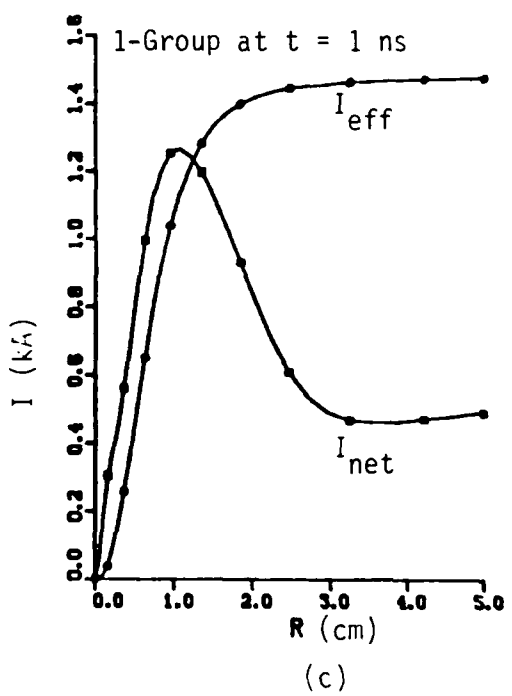

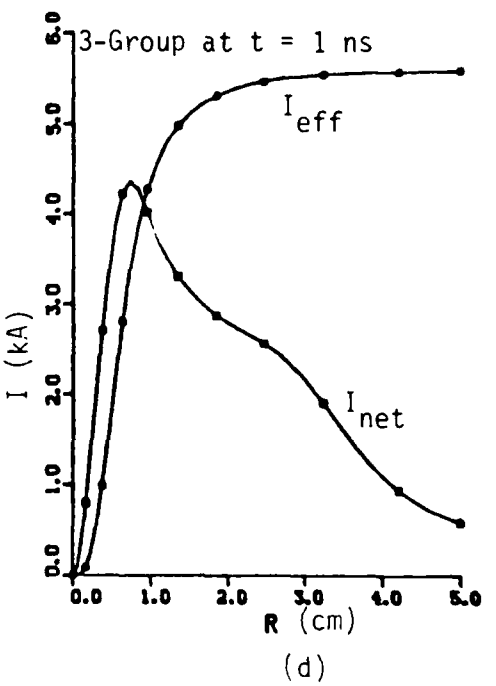

Figure 3.7(a)-(d). I_{net} and I_{eff} (Δ/Δ_0 = .008).

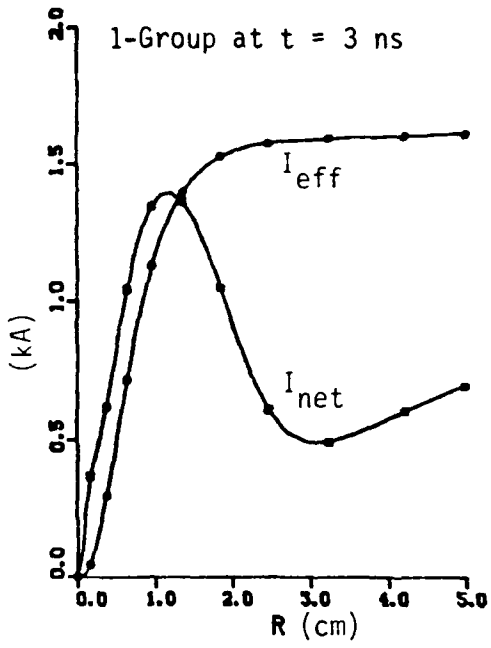

(e)

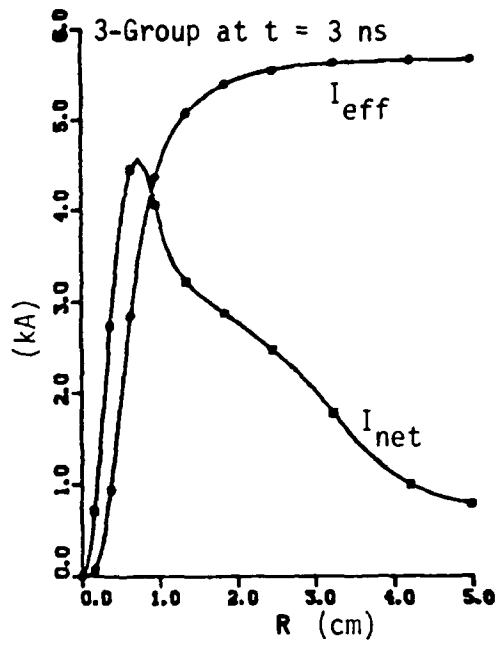

(f)

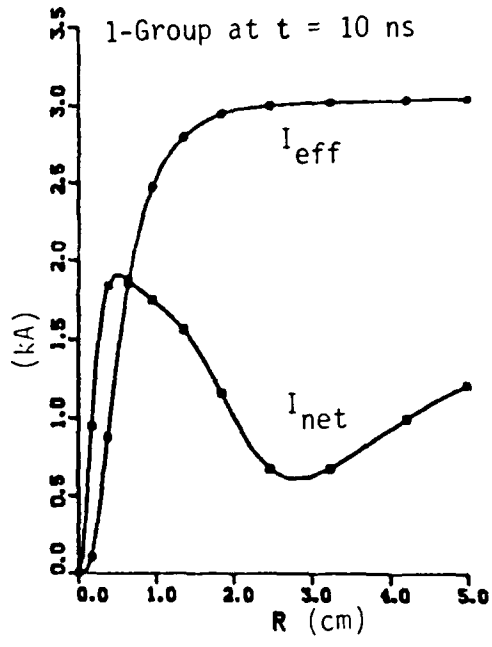

(g)

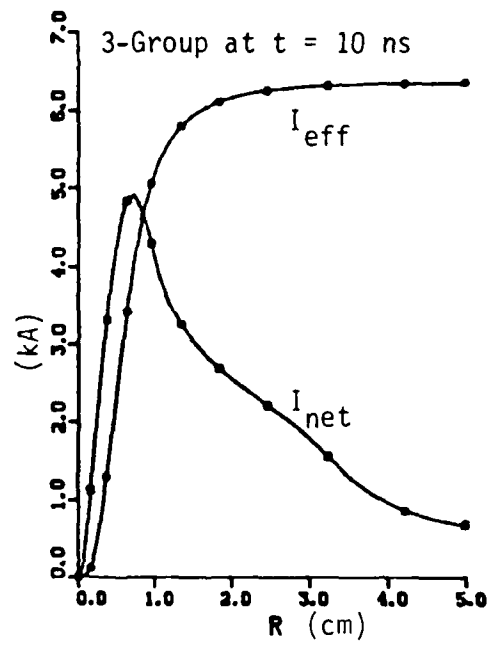

(h)

Figure 3.7(e)-(h). I_{net} and I_{eff} (Δ/Δ_0 = .008).

A comparison of the plasma current (J_z) radial profiles at 1 ns is shown in Figure 3.8. The breakdown of the 3-group profile into contributions from the high and low-energy electron groups is discussed below.

Electron and Ion Density Profiles

Major qualitative differences in the evolution of the electron density are apparent in Figures 3.9(a) - (d). The 1-group calculation shown in Figure 3.9(a) has the usual peak slightly off axis due to the E_r-initiated avalanche and is not unusual. The 3-group calculation for the low group (Figure 3.9(b)) is much more interesting. It shows a large peak well off axis and much higher density at large radius. The high-group density (Figure 3.9(c)) has features which invite interpretation as propagating sound waves. The ridge which appears earliest in time is associated with the rise of the E_r field and the second begins on the axis near the peak of E_z. There is a hint of the first ridge in the low-group density also.

The total positive ion density is shown in Figure 3.9(d). Since the immobile ions show the same gross features as the low-group electron density, it is clear that the large off-axis peak must be interpreted in terms of the history of the ionization rates. However, the weak ridge in the low-group electron density does not appear in the ion density, and thus may be a flow feature. The number of particles in the high group is not large enough for the ridges of Figure 3.9(c) to show up in the ion density (Figure 3.9(d)). It seems likely that they are similar in nature to the ridge in the low-group electron density. Further support for the flow explanation is provided by Figures 3.10(a) and (b). These show the low-group and total ion-densities for the 1-group calculation at $\rho/\rho_0 = .005$, in which there is a large current enhancement compared to $\rho/\rho_0 = .008$ (see Figure 3.7). Here the ridge structures in the electron density are more prominent, but still have no strong counterpart in the ion density.

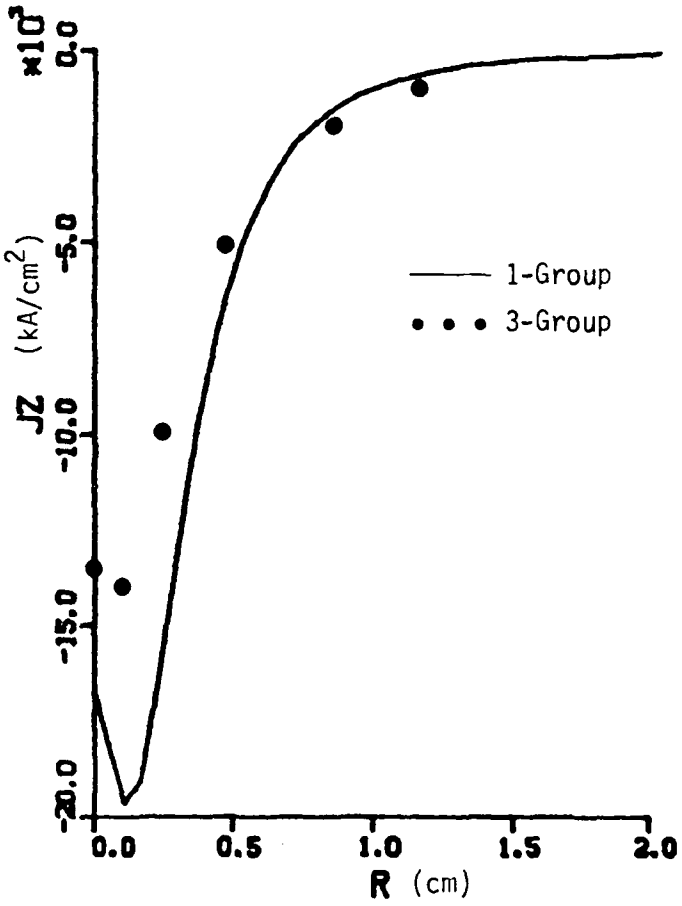

Figure 3.8. Plasma Current Density J_z at 1 ns (ρ/ρ_o = .008).

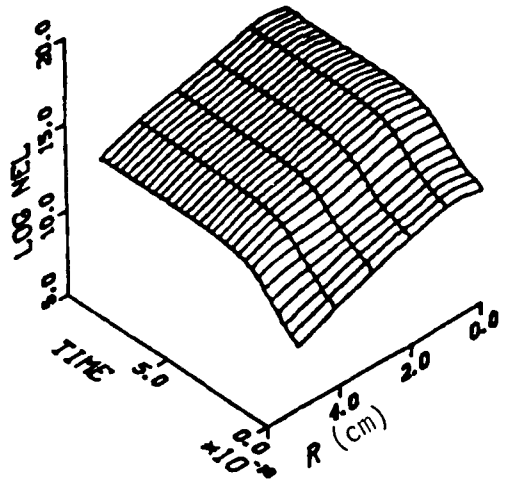

Fig. 3.9(a). Low Energy Group Electron Density (0-1 ns) for 1-Group Model at ρ/ρ_0 = .008.

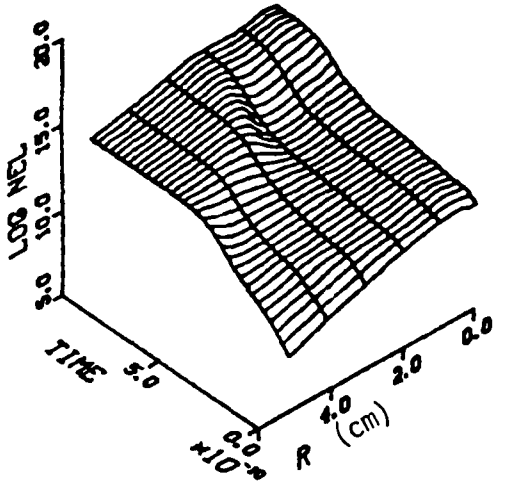

Fig. 3.9(b). Low Energy Group Electron Density (0-1 ns) for 3-Group Model at ρ/ρ_0 = .008.

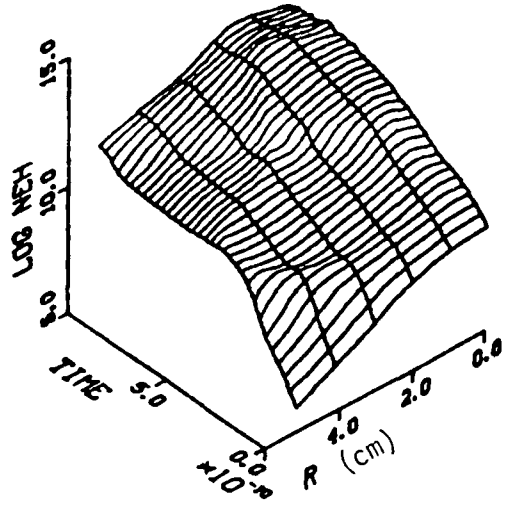

Fig. 3.9(c). High Energy Group Electron Density (0-1 ns) for 3-Group Model at ρ/ρ_0 = .008.

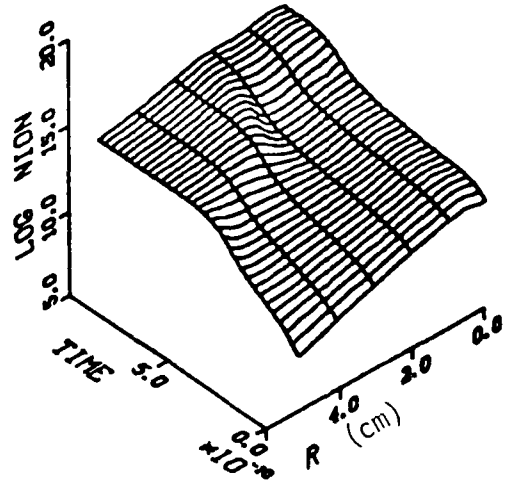

Fig. 3.9(d). Total Positive Ion Density (0-1 ns) for 3-Group Model at ρ/ρ_0 = .008.

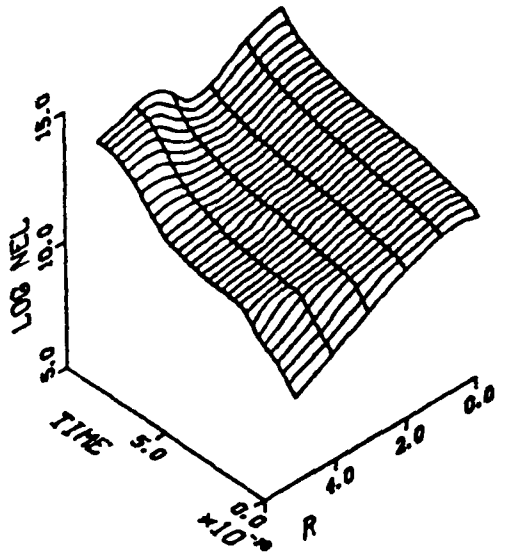

Figure 3.10(a). Electron Density (0-1 ns) for 1-Group Model at ρ/ρ_0 = .005.

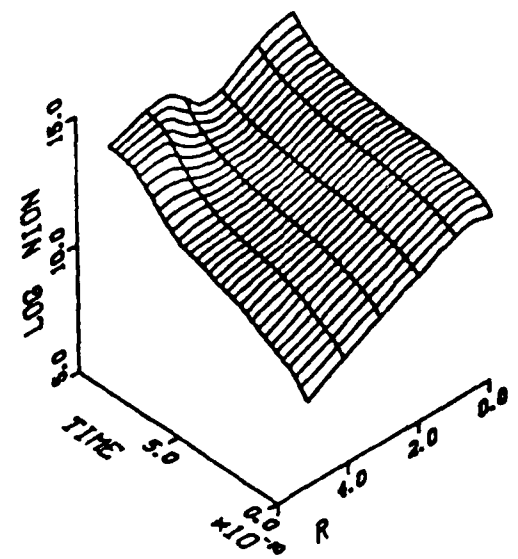

Figure 3.10(b). Positive Ion Density (0-1 ns) for 1-Group Model at ρ/ρ_0 = .005.

The difference in positive ion density radial profiles at 1 ns is shown clearly in Figure 3.11(a). At this time the ion density is much greater than the beam particle density, so these profiles are very close to the electron density in the charge-neutralized state. The effect on the z-component of plasma current was shown earlier (Figure 3.8). Figure 3.11(b) shows how the relatively small difference in ion densities on axis due to time delay before 0.1 ns, becomes very large for a few tenths of ns before coming together again.

For ease of detailed comparison, electron density radial profiles for the 1-group model and for the low and high-energy components of the 3-group model are shown in Figures 3.12(a) - (c). The large temporary off-axis hump in the low-group electrons is very clear at 0.6 ns in Figure 3.12(b). The very much broader density profiles produced by the 3-group model are also very obvious, and persist out to 10 ns from the pulse head.

A summary of electron and ion number density comparisons on axis is given in Table 3-1 below. The first two entries of the third column show the magnitude of the time-delay effect, while subsequent entries show the large differences seen in Figure 3.11(b). The first two columns give an indication of the importance of electron transport. At 0.3 ns for the 3-group model, only 47% of the plasma electrons ever produced on axis remain there.

TABLE 3-1

ELECTRON TRANSPORT EFFECTS

Time (ns)	(N_e/N_i) 1-Group	(N_e/N_i) 3-Group	$\frac{N_i(3\text{-Group})}{N_i(1\text{-Group})}$
.03	.98	.97	.69
.06	.87	.86	.68
.1	.77	.67	.37
.3	.99	.47	.014
.6	.99	.76	.027
1	.99	.99	1.27
3			.82
10			.93

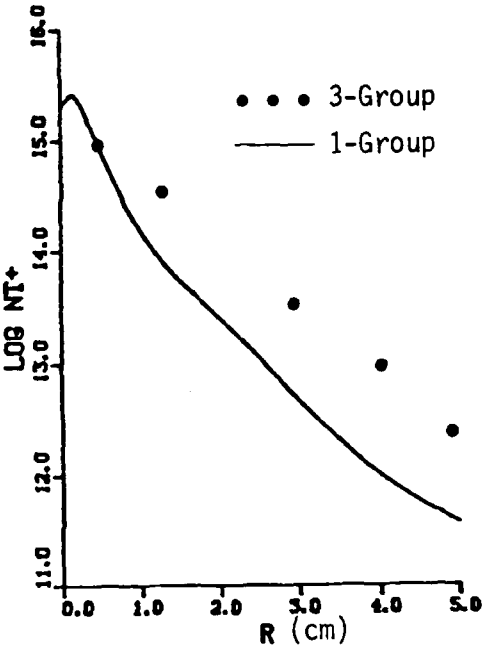

Figure 3.11(a). Positive Ion Radial Profile at 1 ns (ρ/ρ_0 = .008).

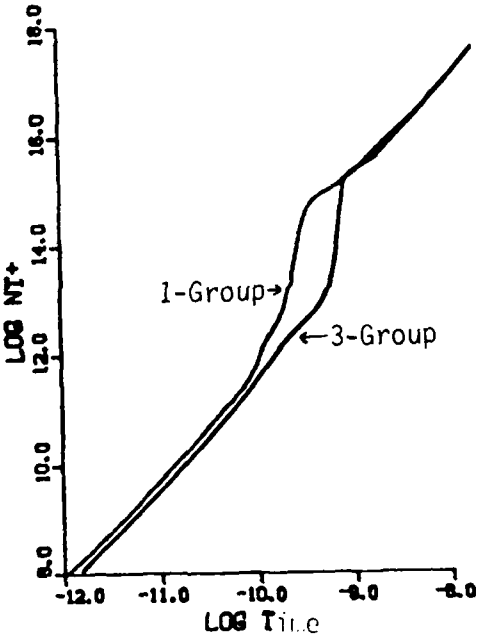

Figure 3.11(b). Positive Ion Density on Axis (ρ/ρ_0 = .008).

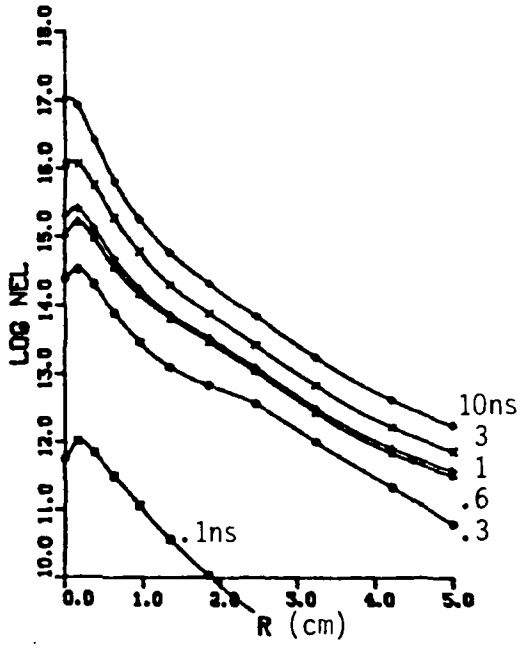

Fig. 3.12(a). Low Energy Group Electron Density Profiles, 1-Group Model (ρ/ρ_o = .008).

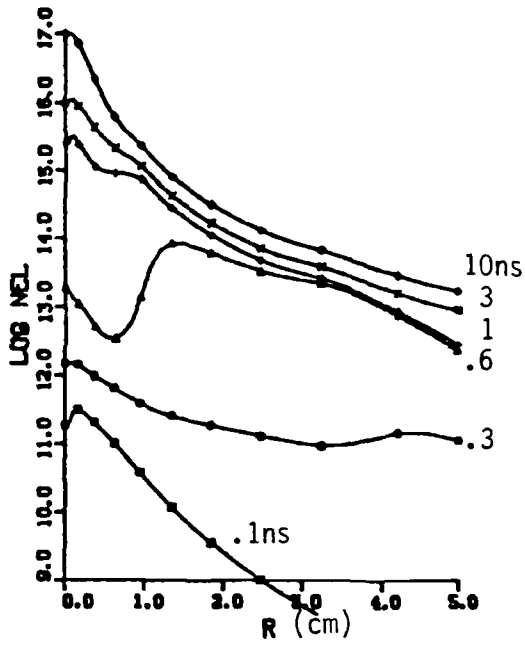

Fig. 3.12(b). Low Energy Group Electron Density Profiles, 3-Group Model (ρ/ρ_o = .008).

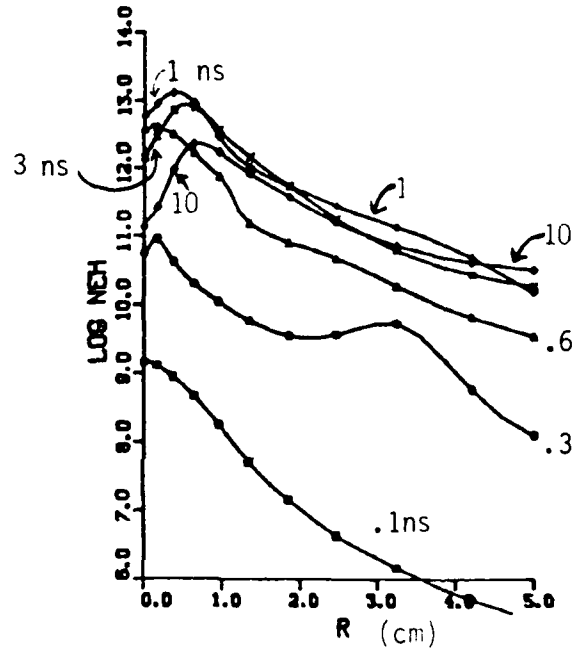

Fig. 3.12(c). High Energy Electron Density Profiles, 3-Group Model (ρ/ρ_o = .008).

Electric Field Effects

Both the E_z spike and the final decay of E_r occur significantly earlier in time for the 1-group model (Figures 3.13(a) - (d)), and the peak field strengths are lower. The large negative oscillation in E_r at 1 Bennett radius is especially prominent in the 3-group calculation, but appears to damp out satisfactorily. The negative spike in E_r in caused by an overshoot of the outward-moving electrons as charge neutralization is finally achieved near the axis. The significant overshoot is consistent with the fact that the electron plasma frequency is much greater than the collision frequency at $\sim$ 0.3 ns. The large off-axis hump in ion density at 0.6 ns (Figure 3.12(b)) seems to be associated with the deceleration of the low-group electrons by the reversed E_r, and by their final cooling through the peak of the ionization cross section. The final cooling occurs considerably earlier off-axis, as shown in Figure 3.14(a). The temperature behavior of the 1-group model is also shown for completeness in Figure 3.14(b).

3.2.5.4 Hall Current Effects

Introduction

Hall currents may be comparable to ordinary currents when the Larmor frequency eB/mc is comparable to or greater than the momentum transfer frequency. This criterion is a strong function of both ambient density and electron energy. The 3-group model allows the possibility of accounting for the energy dependence in a strongly non-Maxwellian plasma. The momentum transfer frequency at 1 eV in N_2 is about the same as that at 200 eV, and decreases with energy beyond 50 or 60 eV. Thus, if a substantial fraction of the electrons have energy in excess of 200 eV, their low momentum transfer frequency may result in a significant Hall current, out of proportion to their fractional number density.

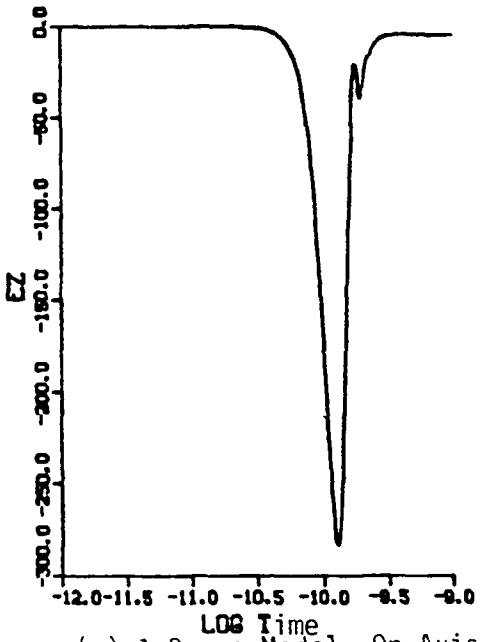

(a) 1-Group Model, On-Axis.

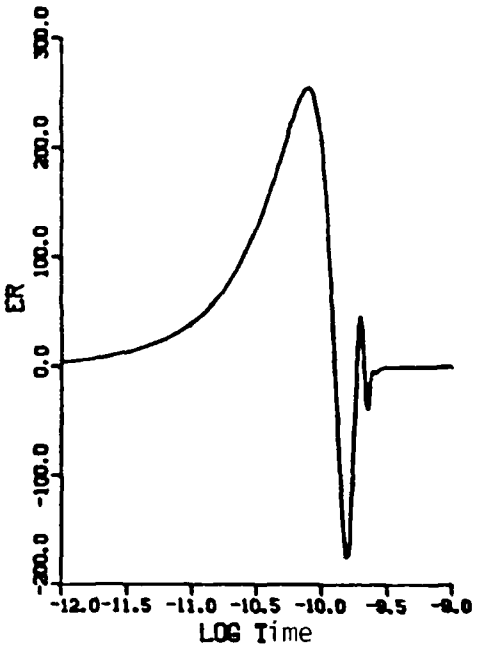

(b) 1-Group Model, 1 BR.

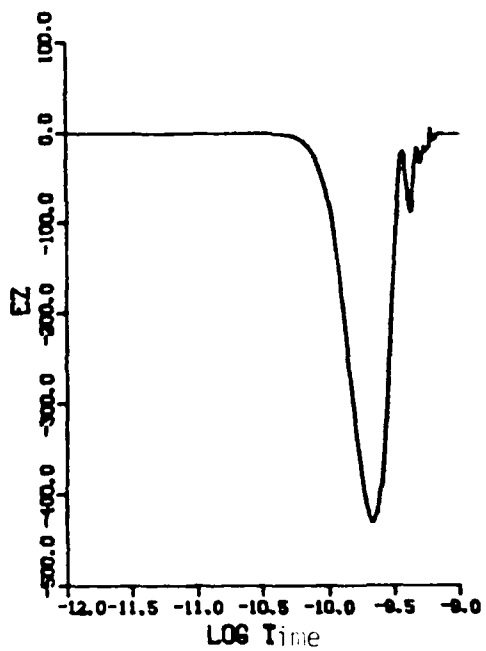

(c) 3-Group Model, On-Axis.

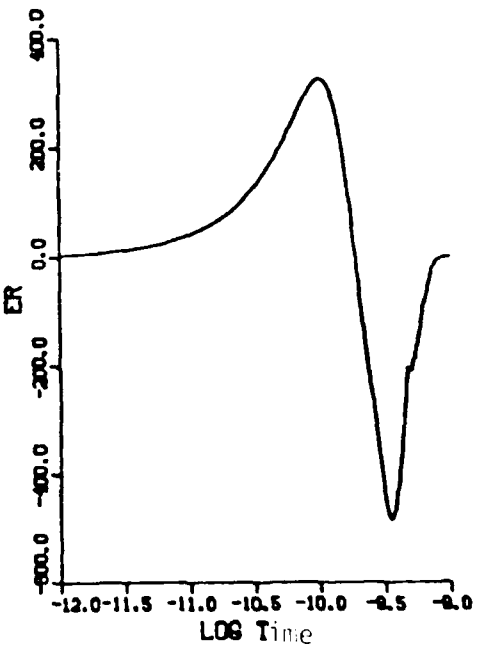

(d) 3-Group Model, 1 BR.

Figure 3.13(a)-(d). Electric Fields (esu) (/ $_0$ = .008).

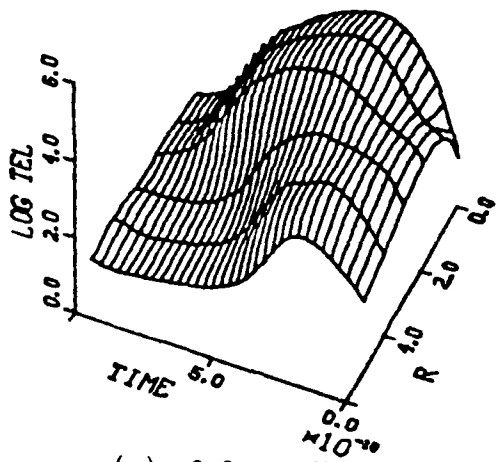

(a) 3-Group Model.

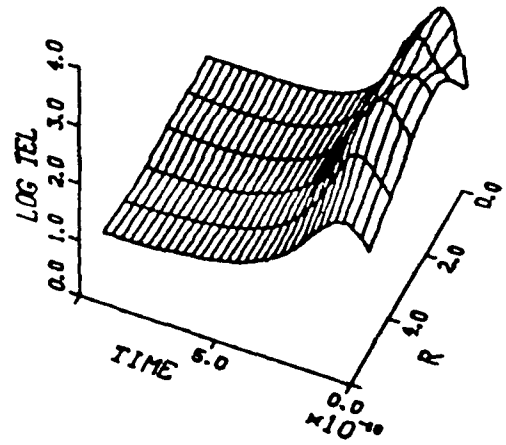

(b) 1-Group Model.

Figure 3.14(a) and (b). Electron Temperature (0-1 ns) λ/λ_0 = .008.

Detailed Discussion

It is clear from Figure 3.6 discussed in Section 3.2.3 above that Hall currents are important to the pinch force. In the calculation at $\rho/\rho_0 = .008$, even the low-energy electron group achieves high velocity for a short time, and contributes substantial Hall current. However, this is generally masked by the E_z-driven return current. In the far wings, however, and at early times near the axis, the radial outflow driven by E_r is turned forward by the magnetic field and the net plasma current density is forward. The amount of current involved, however, is insignificant in magnitude compared to the beam current.

When the high-energy electron group from the 3-group model is examined separately, it shows quite large effects. The z-component of plasma current for the high group is shown at various times in Figure 3.15(a). Beyond about 1.5 Bennett radii it is always directed forward with the beam. Nearer the axis, the strong E_z field keeps the current going backwards, although by 10 ns there is relatively little backward-moving current in the high group. A small part of this forward-going current is due to the fact that high-group electrons produced directly by the beam are injected with forward velocity. However, most of it is due to the Hall force acting on the radial out-flow.

The effect of Hall current in the high energy electron group is shown in Figure 3.15(b). At 1 ns, the forward-going current near 1 Bennett radius amount to almost 2 kA/cm^2, compared to the $\sim$ 5 kA/cm^2 of low group plasma current going backwards at the same radial position. The result is a very significant reduction of the total return current.

It is important to note that at late times $\gtrsim$ 0.5 ns, the radial flow which is turned forward by the magnetic field is driven not primarily by E_r, but by the radial pressure gradient of the high-group particles. Yu (Ref. 10) first recognized this as a possible important component of the total current.

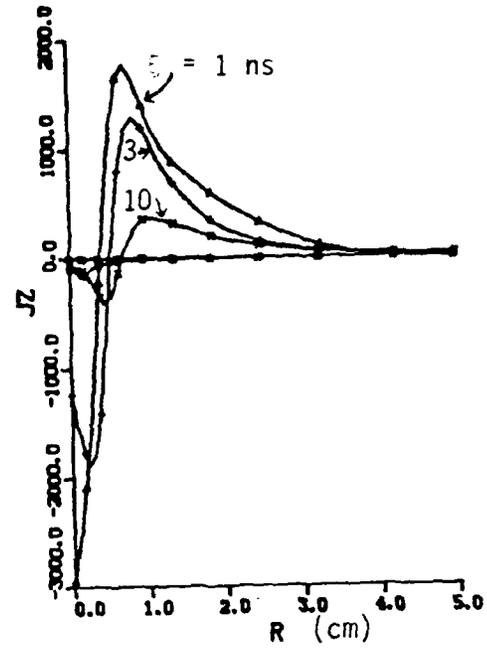

Figure 3.15(a). Current Density J_z of High Energy Electrons (ρ/ρ_o = .008).

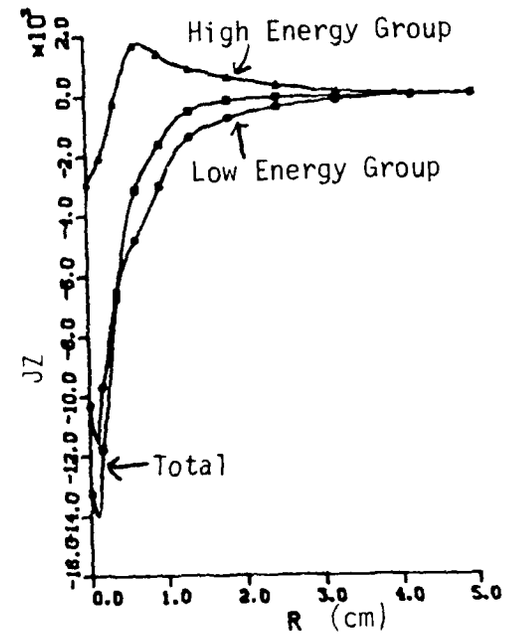

Figure 3.15(b). Effect of High Energy Electrons on Total Plasma Current Density J_z at 1 ns (ρ/ρ_o = .008).

From the equation of motion it is clear that a density gradient is equivalent to a radial electric field of magnitude

$$E_r = - T \frac{\partial \ln N}{\partial r} \text{ volts/cm.}$$

For $T \sim 10$ KeV as suggested by Yu (and used for the high group in these calculations), and a density gradient with scale ~ 1 cm, this corresponds to $E_r \sim 10$ KeV/cm. Assuming that the system as a whole approaches a steady state solution of Maxwell's equations, J_r must $\rightarrow 0$. In the presence of the Hall-force terms, the radial E_r adjusts itself to shut off the net current driven by $v_z B_\theta$, E_r, and the pressure gradient. In the present context it seems that zero net radial current could perhaps be achieved by a balance between an inward flow of very low energy electrons and an outward flow of a much smaller number of fast electrons. Because of the differences in ν_m for the two streams, the corresponding Hall currents would not cancel exactly in this case. Under some conditions such counterflows may be limited by instabilities.

3.2.5.5 Delta Ray Effects at Low Density

Although the steady state δ-ray current is independent of air density, the time required for the current to reach its maximum value depends strongly on the density. There is also a significant dependence on the beam energy if only relativistic particles ($\gtrsim 1$ MeV) are included, as shown in Figure 3.16. The pulse length used in this calculation was 100 ns. (A very steep drop in δ-current at 1 atmosphere on a timescale of 10 ns beginning just before the pulse ends is not shown.) It is clear that at densities as low as .01 atmosphere the δ-current represents a very small increment to the beam current over the first 10 ns considered in the calculations presented above. Before 0.1 ns, the δ-current is comparable to the plasma current in the z-direction, but both are very much smaller than the beam current. It seems unlikely that the relativistic part of the beam secondary cascade can be important at early times for air densities as low as .01 atomsphere. However, for propagation in a density channel, the interaction with the high-density walls may be very important.

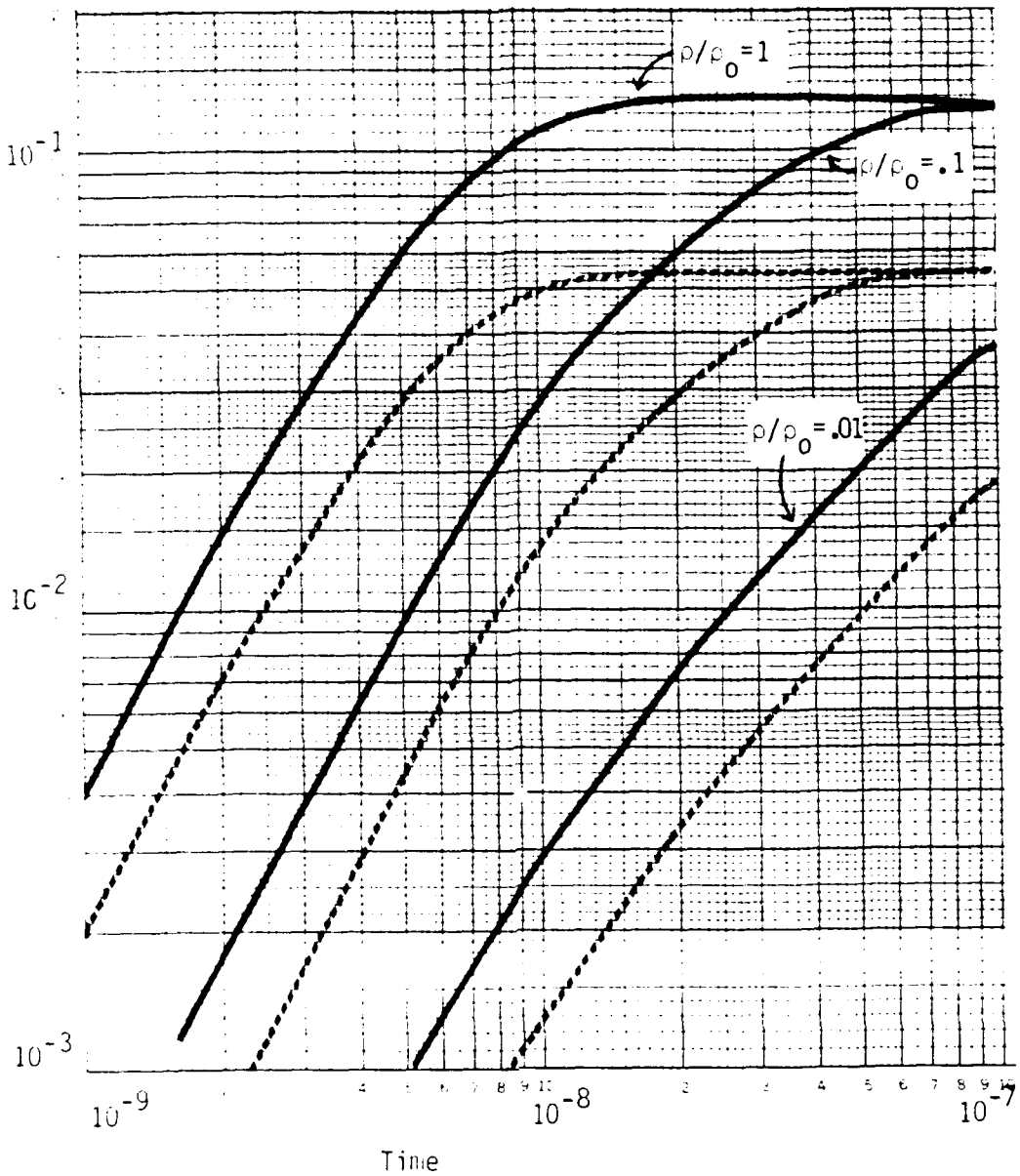

Figure 3.16. (Delta Ray Current)/(Beam Current) at Energy = 1 MeV.
Solid Curves: E_{beam} = 100 MeV
Dashed Curves: E_{beam} = 10 MeV

3.2.5.6 Comparison with Ohm's Law

Both the 1- and 3-group models use equations of motion to describe the electron flows. In general, the difference between the currents calculated this way, and by using an Ohm's law relationship involving only electron density and momentum transfer frequency, is large at early times. The duration of the deviation from Ohm's law increases as the gas density decreases. Figures 3.17(a) and (b) show the actually-computed plasma current compared with what would have been obtained from an ohmic calculation using the instantaneous values of N_e and ν_m. The results are shown for the 1-group calculation at ρ/ρ_o = .008, but comparable effects are present for the 3-group case. At 0.1 ns the ohmic current shows an extremely strong Hall effect due to the large radial field; the current given by the equation of motion is very much smaller, and the Hall effect does not show on the linear scale. At 1 ns, the two methods of calculating the current give virtually identical profiles, as shown in Figure 3.17(b).

3.2.5.7 Concluding Remarks

The calculations discussed above show the magnitude of the effects to be expected when low-density phenomena are taken into account. All the commonly used assumptions listed in Section 3.2.2 above have significant impact on the results at ρ/ρ_o = .01. (The current carried by relativistic beam secondaries is important at low densities only if the pulse is long enough for the full build-up to occur.)

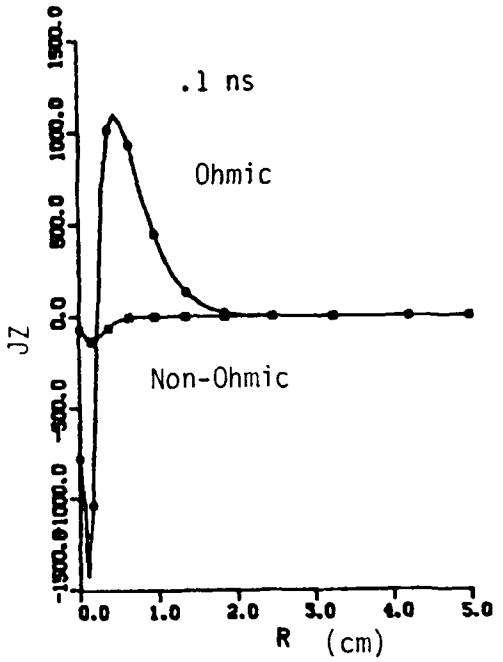

(a)

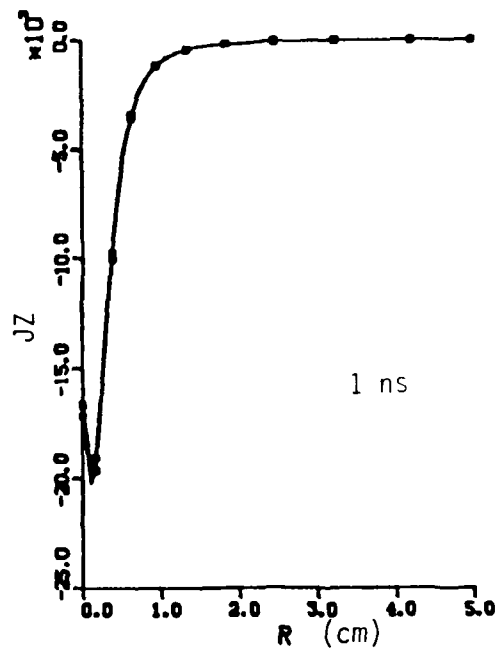

(b)

Figure 3.17(a) and (b). Comparison of Ohmic Calculation of Plasma Current Density with Equation of Motion Calculation.

4.0 NONLINEAR FIELD ALGORITHM DEVELOPMENT

4.1 Outline of the MAHD Approach

The MAHD (for "Moderate Amplitude Hose Displacement") e.m. field algorithms were developed for application to a phenomenological model of electron beam hose dynamics in the nonlinear regime. The value of a phenomenological hose dynamics model in the linear (small hose displacement) regime has been well demonstrated by codes such as PHLAP (Ref. 1); the extension to the nonlinear regime is critical for studying non-linear saturation and propagation in non-uniform ambient density and conductivity channels. PHLAP and other similar models approximate some of the physical details incorporated in elaborate particle simulations, but are fast-running and economical. With careful calibration against comprehensive simulation codes (Ref. 7), phenomenological models make parametric studies over extended ranges of beam characteristics more feasible.

The MAHD electromagnetic (e.m.) field algorithms are required to be fast in execution and sufficiently accurate for the applications of interest. All field solution methods presently in use (DYNASTY, Ref. 14, DYNADISC, Ref. 15, and IPROP, Ref. 7) employ a modal expansion of the beam's fields about some axis of symmetry; MAHD is not an exception. Because an accurate representation of the fields for a beam that is strongly displaced (say, by more than a Bennett radius) from the nominal propagation axis requires an extremely large number of modes, validity for moderate displacements only is claimed for the MAHD algorithms. This limitation is shared, in practical terms, by other schemes using the modal expansion approach as well.

The present study considered two distinct physical approximations in the formulation of the field equations . A first approximation considered was the so-called "frozen approximation". A further approximation, developed by Lee (Ref. 16), neglects the effects of the $\dot{E}_z$- and $\dot{H}_z$-terms that appear in the field equations. One has the further option of considering equations written in terms of potentials or of dealing directly with the electromagnetic fields. In this study, we compare three algorithms as follows:

- o Potential equations in Lee's approximation,
- o Field equations in the frozen approximation, and
- o Field equations in Lee's approximation.

The basic solution technique employed in the MAHD algorithms is as follows: In all formulations of the field (and potential) equations for the modal components, coupling between modes occurs in the field equations because of the angular dependence of σ. For example, the m-th mode of the conduction current, $\{\sigma E\}_m$, is just the coefficient of $\cos(m\theta)$ in the expansion of the product of the two series for σ and for E. Besides contributions from the mode of interest, $\sigma_o E_m$, other terms $\sigma_k E_l$ appear, where $|k \pm l| = m$. This coupling requires, in principle, that the equations for the amplitudes for all modes be solved simultaneously. We have here instead employed a scheme close to that used by Godfrey in IPROP (Ref. 7). In this scheme the modally-resolved set of field equations are solved in mode by mode subsets. Contributions to the current from cross terms other than $\sigma_o E_m$ are regarded as approximately known and fixed for the m-th mode calculation. Cross-term contributions are refined in an iterative procedure involving repeated sweeps through solutions for sequential mode values. The iterative scheme avoids the labor in the alternate approach of solving the very large set of equations generated by solving simultaneously for the field amplitudes in all modes. We have found that only a few passes are required (two to three, at most) for good accuracy; fast computer execution, and a nearly linear increase in execution time with the number of modes carried, result.

The remainder of this section will provide details of the three algorithms studied and of the iterative solution scheme that they all used. A standard test problem, formulated by F. Chambers of LLNL and G. Joyce of NRL, was used for comparison of the three algorithms among themselves and with other solution codes; results of those comparisons will also be given.

4.2 Formulation of the MAHD Algorithms

The MAHD algorithms are formulated with the frozen approximation and the modal expansion as a common basis. Given fields in the laboratory cylindrical coordinates (r', θ', z', t'), we make the usual Galilean transformation to beam coordinates

$$\left.\begin{aligned} r &= r' \\ \theta &= \theta' \\ z &= z' \\ \xi &= t' - z' \end{aligned}\right\} \tag{4.1}$$

where the coordinate ξ measures "beam time", or time elapsed since the head of the beam (at $\xi = 0$) passes an observer at some value of z'. The frozen approximation follows immediately from a transformation of the field equations to beam coordinates and the assumption that, in beam coordinates, fields vary slowly with z; that is:

$$\frac{\partial}{\partial z} << \frac{\partial}{\partial \xi} \tag{4.2}$$

Specific sets of field equations will be shown later in the section.

The modal expansion is simply a Fourier-series representation of the dependence of the various field quantities on the transverse coordinate θ. We have assumed, to simplify initial development work, that the (x,z)-plane is a symmetry plane for the fields, corresponding physically to hose displacements in the x-direction only, and that the θ- and r-components of the beam current can be ignored. With these assumptions, the primary beam current $J_z(r,\theta,\xi)$ is given, for example, by:

$$J_z(r, \theta, \xi) = \sum_{m=0}^{N} J_{zm}(r,\xi) \cos m\theta \tag{4.3}$$

The beam-induced conductivity σ, the e.m. potentials A and ϕ, and the e.m. field quantities E_r, E_z, and H_θ are also even (symmetric) functions of θ, and are given by analogous cosine-series expansions. The remaining field quantities H_r, H_z, and E_θ are odd (antisymmetric) functions of θ, and are given by a sine-series expansion; for example:

$$H_z(r,\theta,\xi) = \sum_{m=1}^{N} H_{zm}(r,\xi) \sin m\theta \tag{4.4}$$

All three algorithms use essentially identical methods to resolve the (r,θ) sources into modes -- as generally required by the algorithms -- and to form the modal amplitudes associated with the products of two modal expansions (as required by the iterative scheme). We briefly summarize those methods next.

The present algorithms all use straightforward Fourier series expansion formulae. It was felt that, for small numbers of modes, the speed advantage of FFT techniques was probably not significant. The modal resolution procedure does in fact typically use only about 5% of the total time spent by the solution algorithms as presently programmed (see Sec. 4.4).

By our convention, an even function $\sigma(\theta)$ is expanded as

$$\sigma(\theta) = \sigma_0 + \sum_{m=1}^{N} \sigma_m \cos m\theta \tag{4.5}$$

where

$$\sigma_0 = \frac{1}{\pi} \int_0^{\pi} \sigma(\theta) d\theta \tag{4.6}$$

and

$$c_m = \frac{2}{\pi} \int_0^{\pi} \sigma(\theta) \cos m\theta \, d\theta \qquad m \geq 1 \qquad (4.7)$$

(The integrals in the above equations are evaluated using Simpson's (3-point) rule in a direct numerical integration. If N is the highest mode number to be used, 2N+1 points in the interval $[0,\pi]$ are typically used in the integration.)

All of the MAHD algorithms require re-expanding the products of two modal series into modes. Assume that $a(\theta)$ and $b(\theta)$ are even functions representable by a finite cosine series (maximum mode number N), and that $c(\theta)$ and $d(\theta)$ are odd functions given by sine series of the same length N. We ignore modes of higher order than N in the product.

Even-Even Products. The product $a(\theta)b(\theta)$ is also even, and the cosine series coefficients are as follows:

$m = 0$:

$$\{ab\}_0 = a_0 b_0 + \frac{1}{2} \sum_{\ell=1}^{N} a_\ell b_\ell \qquad (4.8a)$$

$m \geq 1$:

$$\{ab\}_m = a_0 b_m + a_m b_0 + \frac{1}{2} \sum_{\ell=1}^{m-1} a_\ell b_{m-\ell} + \frac{1}{2} \sum_{\ell=1}^{N-m} (a_\ell b_{m+\ell} + a_{m+\ell} b_\ell) \qquad (4.8b)$$

The first summation on the right is dropped if $m \leq 1$, and the second is dropped if $m = N$.

Odd-Odd Products. The product $c(\theta)d(\theta)$ is even, and the cosine series coefficients of cd are as follows:

$m = 0$:

$$\{cd\}_o = \frac{1}{2} \sum_{\ell=1}^{N} c_\ell d_\ell \tag{4.9a}$$

$m > 1$:

$$\{cd\}_m = -\frac{1}{2} \sum_{\ell=1}^{m-1} c_\ell d_{m-\ell} + \frac{1}{2} \sum_{\ell=1}^{N-m} (c_\ell d_{m+\ell} + c_{m+\ell} d_\ell) \tag{4.9b}$$

As before, the first summation on the right is dropped if $m \leq 1$, and the second is dropped if $m = N$.

Even-Odd Products. The product $a(\theta)c(\theta)$ is odd, and the sine-series coefficients for $m \geq 1$ are as follows:

$$\{ac\}_m = a_o c_m + \frac{1}{2} \sum_{\ell=1}^{m-1} a_\ell c_{m-\ell} + \frac{1}{2} \sum_{\ell=1}^{N-m} (a_\ell c_{m+\ell} - a_{m+\ell} c_\ell) \tag{4.10}$$

Summations are dropped for $m = 1$ and $m = N$ as in the previous cases.

As indicated earlier, we employ iteration schemes in which (for example) conduction current in a particular mode, $\{\sigma E\}_m$, is separated into the principal contribution from the mode of interest, $\sigma_o E_m$ and other contributions. We thus define the function $P_{cc}(a,b,m)$ as representing the summed

terms in the m-th mode of the product of the two cosine series for the even functions $a(\theta)$ and $b(\theta)$, except for the term $a_o b_m$:

$$P_{cc}(a,b,m) = \{ab\}_m - a_o b_m \tag{4.11}$$

Inspection of Eq. (4.8) above shows that $P_{cc}(a,b,m)$ as defined may contain the high-order term $\sigma_{2m} b_m$, but contains no other low-order terms involving b_m. We also define the analogous function $P_{cs}(a,c,m)$ to separate $a_o c_m$ and other contributions to the m-th mode of the product of the cosine series $a(\theta)$ and the sine series $c(\theta)$. Note that in this case, $a(\theta)c(\theta)$ is an odd function of θ, and is expanded in a sine series; there is no m=0 component in the product expansion:

$$P_{cs}(a,c,m) = \{ac\}_m - a_o c_m \quad (m \geq 1) \tag{4.12}$$

Finally, simply define $P_{ss}(c,d,m)$ as the m-th mode amplitude in the (cosine) series expansion of the product of the odd functions $c(\theta)$ and $d(\theta)$.

$$P_{ss}(c,d,m) = \{cd\}_m \tag{4.13}$$

Explicit expressions for P_{cc}, P_{cs}, and P_{ss} follow immediately from Eqs. (4.8) - (4.10).

4.2.1 Reduced-Potential Algorithm MAHD1

The first algorithm we will consider is based on Lee's simplification (Ref. 16) of the frozen approximation for the e.m. potential equations. The assumptions leading to the final set of equations are equivalent to neglecting beam-time derivatives of E_z and H_z in the e.m. field equations. It is unnecessary to find the transverse component of the vector potential, $A_\perp$. It is convenient to define the remaining two potential components of interest as A and :, where : is the usual scalar potential, and

$$A = A_z - \phi \tag{4.14}$$

where A_z is the axial component of the usual vector potential.

In RMKS units, Lee's equations for A and ϕ are

$$\nabla_\perp^2 (A + \phi) = Z_o \sigma \frac{\partial A}{\partial \xi} - Z_o J_z \tag{4.15}$$

$$\nabla_\perp^2 \frac{\partial A}{\partial \xi} = (\vec{\nabla}_\perp Z_o \sigma) \cdot (\vec{\nabla}_\perp \phi) + Z_o \sigma \nabla_\perp^2 \phi \tag{4.16}$$

(A and ϕ in the above equations are expressed in units of volts; the beam-time coordinate ξ is expressed in meters. Z_o is the free-space impedance of 376.7 ohms, and the units of the conductivity, σ, are mho/m.) The e.m. fields are found from the potentials via the following relations:

$$\left.\begin{aligned} E_z &= - \frac{\partial A}{\partial \xi} & \vec{H}_z &= \vec{\nabla}_\perp \times \vec{A}_\perp \\ \vec{E}_\perp &= - \vec{\nabla}_\perp \phi & \vec{H}_\perp &= - \vec{u}_z \times \vec{\nabla}_\perp A_z \end{aligned}\right\} \tag{4.17}$$

(The units of E and H in the RMKS form above and to be used hereafter are volts/meter; the more usual RMKS H-field differs from our usage by a factor of Z_o.) As noted earlier, $\vec{A}_\perp$ and H_z are not calculated in this formulation.)

Equations (4.15) and (4.16) are recast into finite-difference form by resolving them into m-th modes ($0 \leq m \leq N$). Potential quantities are defined on a set of radial grid points r_j ($1 \leq j \leq N_R$) and at the beam-time points ξ_i ($i = 1, 2, \ldots$). The differencing is centered at $(i+1/2, j)$, i.e., on the radial gridpoints, but midway between ξ_i and ξ_{i+1}. An arbitrary radial grid structure (in terms of spacing) is assumed, and 3-point Lagrange differentiation formulae are used generally to evaluate first- and second-radial derivatives at r_j.

Equation (4.15) is readily differenced. The lefthand term is represented as follows: for the m-th mode,

$$\left\{\nabla_\perp^2 (A + \phi)\right\}_m = \left(\frac{\partial^2}{\partial r^2} + \frac{1}{r}\frac{\partial}{\partial r} - \frac{m^2}{r^2} \right) (A_m + \phi_m) \qquad (4.18)$$

Radial derivatives centered at r_j in the above equation are simply expressed in terms of potentials at the points r_{j-1}, r_j, and r_{j+1}.

The first term on the r.h.s. of Eq. (4.15) is separated (as suggested at the beginning of 4.2) into two portions:

$$\left\{ Z_o \sigma \frac{\partial A}{\partial \xi} \right\}_m = Z_o \sigma_o \frac{\partial A_m}{\partial \xi} + P_{cc}\left(Z_o \sigma, \frac{\partial A}{\partial \xi}, m\right) \qquad (4.19)$$

The quantity $Z_o \sigma_o (\partial A_m / \partial \xi)$ is represented as a simple difference, centered at (i+1/2,j). The function P_{cc} (a,b,m) represents the summed terms in the m-th mode of the product of the cosine series for the functions a and b, except for the term $a_o b_m$. P_{cc} contains no other low-order b_m mode terms, and is considered a known quantity in the solution of the m-th mode difference equations derived here. Specific expressions for P_{cc} and other related product expansions are found from Eqs. (4.8) - (4.13).

Collecting the m-th mode fields on the left, Eq. (4.15) finally yields

$$d_m^2 (A_m + \phi_m) - Z_o \sigma_o \frac{\partial A_m}{\partial \xi} = P_{cc}\left(Z_o \sigma, \frac{\partial A}{\partial \xi}, m\right) - Z_o J_{zm} \qquad (4.20)$$

where

AD-A170 363 STUDIES IN HIGH CURRENT BEAM PROPAGATION AT REDUCED PRESSURES..(U) SCIENCE APPLICATIONS INTERNATIONAL CORP LOS ALTOS CA E R PARKINSON ET AL. 31 JAN 85 2/2

UNCLASSIFIED SAIC-U-75-PA AFOSR-TR-86-0494 F/G 20/9 NL

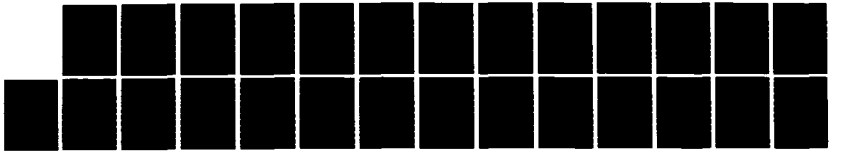

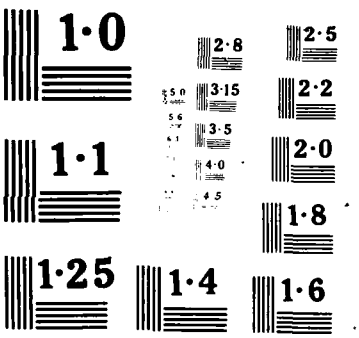
1·0
1·1
1·25
2·8
3·15
3·5
4·0
4·5
5·0
5·6
6·3
1·4
2·5
2·2
2·0
1·8
1·6

$$d_m^2 \equiv \frac{\partial^2}{\partial r^2} + \frac{1}{r}\frac{\partial}{\partial r} - \frac{m^2}{r^2} \qquad (4.21)$$

The finite-difference representation of Eq. (4.16) is obtained in an analogous manner to Eq. (4.15). The lefthand term of Eq. (4.16) is written (see Eq. (4.18))

$$\left\{\nabla_\perp^2 \frac{\partial A}{\partial \xi}\right\}_m = \left(\frac{\partial^2}{\partial r^2} + \frac{1}{r}\frac{\partial}{\partial r} - \frac{m^2}{r^2}\right)\frac{\partial A_m}{\partial \xi} \qquad (4.22)$$

with finite-difference repesentations of the derivatives centered as explained above.

The first term on the r.h.s. of Eq. (4.16) is a vector product:

$$\vec{\nabla}_\perp (Z_o\sigma) \cdot \vec{\nabla}_\perp (\phi) = Z_o \frac{\partial\sigma}{\partial r}\frac{\partial\phi}{\partial r} + \frac{1}{r}\frac{\partial\sigma}{\partial\theta} \cdot \frac{1}{r}\frac{\partial\phi}{\partial\theta} \qquad (4.23)$$

The radial derivative product is a product of cosine series, and is handled as before:

$$\left\{Z_o \frac{\partial\sigma}{\partial r}\frac{\partial\phi}{\partial r}\right\}_m = Z_o\sigma_o \frac{\partial\phi_m}{\partial r} + P_{cc}\left(Z_o\frac{\partial\sigma}{\partial r}, \frac{\partial\phi}{\partial r}, m\right) \qquad (4.24)$$

The θ-derivatives in Eq. (4.23) generate a Fourier sine series for each factor in their product; for example

$$-\frac{\partial\sigma}{\partial\theta} = \sum_{m=1}^{N} m\sigma_m \sin m\theta \qquad (4.25)$$

Because the sine series does not include a monopole term, b_m does not contribute in low order to the m-th mode of the sine-series product.

The rightmost term in Eq. (4.16) is handled as the previous cosine-series products:

$$\left\{ Z_o \sigma \nabla_\perp^2 \phi \right\} = Z_o \sigma_o \; d_m^2 \phi_m + P_{cc} \left(Z_o \sigma_o, \nabla_\perp^2 \phi, m \right) \tag{4.26}$$

Collecting the m-th mode fields on the left, Eq. (4.16) finally yields

$$\begin{aligned} d_m^2 \frac{\partial A_m}{\partial \xi} - Z_o \sigma_o \, d_m^2 \phi_m - Z_o \frac{\partial \sigma_o}{\partial r} \frac{\partial \phi_m}{\partial r} \\ = P_{cc} \left(Z_o \sigma, \frac{\partial \phi}{\partial r}, m \right) + P_{ss} \left(\frac{Z_o}{r} \frac{\partial \sigma}{\partial \theta}, \frac{1}{r} \frac{\partial \phi}{\partial \theta}, m \right) \\ + P_{cc} \left(Z_o \sigma, \nabla_\perp^2 \phi, m \right) \end{aligned} \tag{4.27}$$

The finite-difference forms of Eqs. (4.20) and (4.27) are applied to each of the interior gridpoints r_j $(2 \le j \le N_{R-1})$. Two inner and two outer boundary conditions must be imposed to complete the set of equations for the N_R unknown values of A and ϕ. We adopt the standard boundary conditions,

$$\begin{aligned} \underline{\text{at } r = 0}: \quad & \frac{\partial A_o(o)}{\partial r} = 0, \quad \frac{\partial \phi_o(o)}{\partial r} = 0; \\ & A_m(o) = 0, \quad \phi_m(o) = 0, \text{ for } m \geqslant 1; \end{aligned} \tag{4.28}$$

$$\underline{\text{at } r = R_{max}}: \; A_m(R_{max}) = 0; \; \phi_m(R_{max}) = 0, \text{ for all } m$$

The band matrix representing the set of 2 N_R equations for the A's and ϕ's has a bi-tridiagonal structure; the equations can be solved readily via any of several schemes, including straightforward Gaussian elimination.

The computational cycle for a particular field timestep is illustrated in Fig. 4.1, which outlines the major aspects of the iterative approach. Equations (4.20) and (4.27) (with the boundary conditions of Eq. (4.28)) are solved for potential amplitudes at successive m-values. At a given point in a pass through the m-values, the arrays from which the P_{cc} and P_{ss} terms are calculated involve recently-updated mode amplitudes for m-values less than the mode of current interest, and "last-pass" amplitudes for modes equal to and higher than the current mode. Updated amplitudes are entered for use in the P_{cc} and P_{ss} computations as they are generated. Only a few iterations (two to three passes at most, for the test case considered) appear to be required for accurate results. (A discussion of comparisons will be given in Sec. 4.4).

4.2.2 Frozen-field Algorithm MAHD2

The next algorithm to be considered is a calculation that treats e.m. fields directly (rather than through potential functions) and with no simplifications beyond the frozen approximation. Inserting the transformations (4.1) and the frozen approximation (4.2) into Maxwell's equations immediately yields the basic field equations treated in MAHD2 and (with further approximations) MAHD3:

$$
\begin{aligned}
\hat{u}_z \cdot (\vec{\nabla}_\perp \times \vec{E}_\perp) &= -\frac{\partial H_z}{\partial t} \\
\hat{u}_z \cdot (\vec{\nabla}_\perp E_z + \frac{\partial \vec{E}_\perp}{\partial z}) &= -\frac{\partial \vec{H}_\perp}{\partial t} \\
\hat{u}_z \cdot (\vec{\nabla}_\perp \times \vec{H}_\perp) &= Z_0 J_z + \frac{\partial E_z}{\partial t} \\
\hat{u}_z \cdot (\vec{\nabla}_\perp H_z + \frac{\partial \vec{H}_\perp}{\partial z}) &= Z_0 \vec{J}_\perp + \frac{\partial \vec{E}_\perp}{\partial t}
\end{aligned}
\qquad (4.29)
$$

Figure 4.1. Iterative computation cycle.

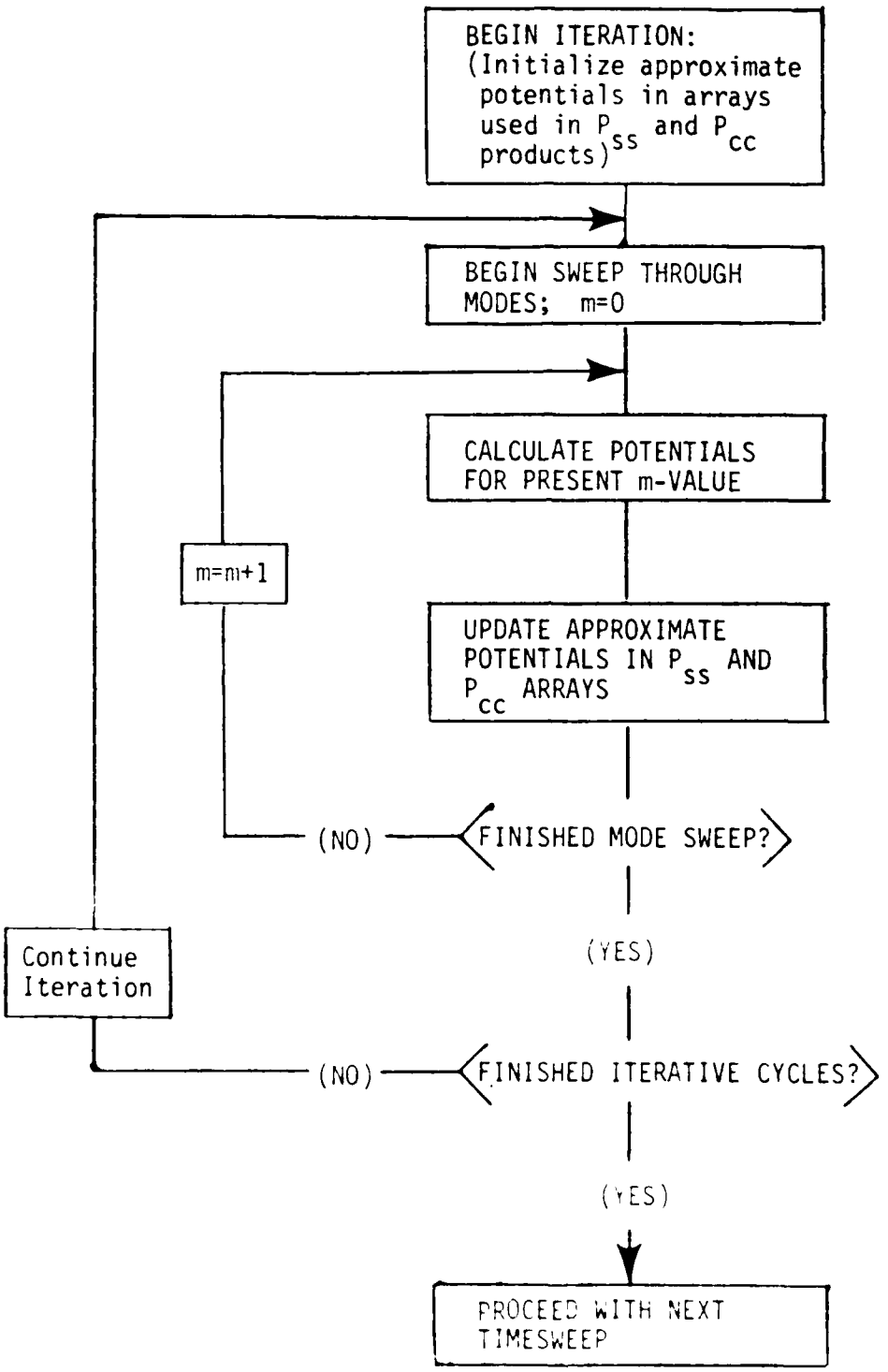

The RMKS Maxwell equations are readily decomposed into modal equations; maintaining the symmetry assumptions outlined at the beginning of the Section (<u>even</u> angular symmetry for σ, J_z, E_z, E_r, and H_θ; <u>odd</u> angular symmetry for H_z, H_r, and E_θ), we find:

$$\frac{1}{r}\frac{\partial}{\partial r}(rE_{\theta m}) + \frac{m}{r}E_{rm} = -\frac{\partial H_{zm}}{\partial \xi} \tag{4.30a}$$

$$-\frac{\partial E_{rm}}{\partial \xi} - \frac{\partial E_{zm}}{\partial r} = -\frac{\partial H_{\theta m}}{\partial \xi} \tag{4.30b}$$

$$\frac{\partial E_{\theta m}}{\partial \xi} - \frac{m}{r}E_{zm} = -\frac{\partial H_{rm}}{\partial \xi} \tag{4.30c}$$

$$\frac{1}{r}\frac{\partial}{\partial r}(rH_{\theta m}) - \frac{m}{r}H_{rm} = \frac{\partial E_{zm}}{\partial \xi} + Z_o\left\{J_z + \sigma E_z\right\}_m \tag{4.30d}$$

$$-\frac{\partial H_{rm}}{\partial \xi} - \frac{\partial H_{zm}}{\partial r} = \frac{\partial E_{\theta m}}{\partial \xi} + Z_o\left\{\sigma E_\theta\right\}_m \tag{4.30e}$$

$$+\frac{\partial H_{\theta m}}{\partial \xi} + \frac{m}{r}H_z = \frac{\partial E_{rm}}{\partial \xi} + Z_o\left\{\sigma E_r\right\}_m \tag{4.30f}$$

Note that the mode amplitude $\{\sigma E_\theta\}_m$ in Eq. (4.30e) is for an odd-symmetry mode; the adjacent equations are for even-symmetry modes.

Because we have not included any components of the beam current but J_z, the monopole-case ($m=0$) fields collapse to the TM set E_z, E_r, and H_θ. Solutions for this axisymmetric case are quite standard, and will not be considered in detail here. We will concentrate on the ($m \geq 1$)-modes in the following discussion.

Equations (4.30a-e) are differenced in a straightforward fashion. First, note that Eqs. (4.30c) and (4.30f) are local equations in the sense that they do not involve spatial derivatives. Finite-difference representations of the "c" and "f" equations are thus centered at (i+1/2,j) and written for each of the N_R radial gridpoints. For one boundary condition treatment, special forms of "c" and "f" are required at $r_1=0$, and will be discussed in connection with boundary conditions on the fields, below.

Equation (4.30c), differenced with the indicated centering, leads to a relation for $E_{zm}(i+1,j)$ in terms of $E_{\theta m}(i+1,j)$ and $H_{rm}(i+1,j)$:

$$E_{zm}(i+1,j) = C_{1j}\left[E_{\theta m}(i+1,j) + H_{rm}(i+1,j)\right] - C_{2j} \qquad (4.31)$$

where

$$C_{1j} = \frac{2r_j}{m\Delta\xi}$$

$$C_{2j} = E_{zm}(i,j) + C_{1j}\left[E_{\theta m}(i,j) + H_{rm}(i,j)\right] \qquad (4.32)$$

Equation (4.30f) is formally integrated in time to obtain a relation for $H_{zm}(i+1,j)$ in terms of $E_{rm}(i+1,j)$ and $H_{\theta m}(i+1,j)$:

$$E_{rm}(i+\tfrac{1}{2},j) = \alpha E_{rm}(i,j) + \frac{1-\alpha}{Z_o\sigma_o}\left[\frac{\partial H_{\theta m}}{\partial \tau} + \frac{m}{r}H_z - Z_o P_{cc}(\sigma, E_r, m)\right]_{i+\frac{1}{2},j} \quad (4.33)$$

yielding

$$H_{Zm}(i+1,j) = F_1 E_{rm}(i+1,j) - F_2 H_{\theta m}(i+1,j) + F_3 \quad (4.34)$$

where

$$\alpha_j = \exp(-Z_o\sigma_o\Delta\xi)$$

$$\beta_j = \frac{1-\alpha_j}{Z_o\sigma\Delta\xi}$$

$$F_{1j} = \frac{2r_j}{m\Delta\xi\beta_j} \quad (4.35)$$

$$F_{2j} = \frac{2r_j}{m\Delta\xi}$$

$$F_{3j} = F_{2j}(H_z(i,j) + P_{cc}(Z_o\sigma\Delta\xi, E_r, m)) - \alpha_j F_{1j} E_r(i,j) - H_z(i,j)$$

The remaining equations, which involve radial derivatives, are cast into finite-difference forms centered at (i+1/2,j+1/2). (Again, special forms of Eqs. (4.30a, b, d, and e) are written at (1+1/2,3/2), the first radial differencing cell, in connection with field boundary conditions; they will be discussed later.) Equations (4.30a) and (4.30b) are differenced in analogy with Eq. (4.30c) (see Eq. (4.31) above), while Eqs. (4.30d) and (4.30e) are formally integrated in analogy to Eq. (4.30f). The differenced form of Eq. (4.30a) (dropping the subscript "m" and the index "i+1") is thus:

$$A_1 E(j+1) - A_2 E(j) + A_3(E_r(j+1) + E_r(j)) + H_z(j+1) + H_z(j) \quad (4.36)$$

$$= rhs_A$$

where

$$A_1 = \frac{r_{j+1}\,\Delta\xi}{r_{j+\frac{1}{2}}\,\Delta r}$$

$$A_2 = \frac{r_j\,\Delta\xi}{r_{j+\frac{1}{2}}\,\Delta r} \tag{4.37}$$

$$A_3 = \frac{m\,\Delta\xi}{r_{j+\frac{1}{2}}}$$

$$rhs_A = H_z(i,j+1) + H_z(i,j) - A_1 E_\xi(i,j+1) + A_2 E_\xi(i,j) - A_3(E_r(i,j) + E_r(i,j+1))$$

Equation (4.30b) is differenced analogously to (4.30a), resulting in an equation of the form:

$$E_r(j+1) + E_r(j) - H_\xi(j+1) - H_\xi(j) + B_1(E_z(j+1) - E_z(j)) = rhs_B \tag{4.38}$$

The differenced form of Eq. (4.30d) is obtained by a formal integration

$$E_z(i+1,\, j+\tfrac{1}{2}) = \alpha E_z(i,j+\tfrac{1}{2}) + \frac{(1-\alpha)}{Z_o\sigma_o}\left[\frac{1}{r}\frac{\partial}{\partial r}(rH_\xi) - \frac{m}{r}H_r - Z_o J_{zm} - P_{cs}(Z_o\sigma,\, E_z,\, m)\right] \tag{4.39}$$

where the quantities enclosed in square brackets are evaluated in ordinary difference form, centered by (i+1/2,j+1/2). Expansion of this equation leads to

$$E_z^2(j+1) + E_z^2(j) - \beta(j+\tfrac{1}{2})A_1 H_\theta(j+1) + \beta(j+\tfrac{1}{2})A_2 H_\theta(j) + \beta(j+\tfrac{1}{2})A_3(H_r(j+1) + H_r(j)) = rhs_D \tag{4.40}$$

where

$$rhs_D = \alpha(j+\tfrac{1}{2})(E_z(i,j+1) + E_z(i,j)) + \beta(j+\tfrac{1}{2})A_1 H_\theta(i,j+1) - \beta(j+\tfrac{1}{2})A_2 H_\theta(i,j) - \beta(j+\tfrac{1}{2})A_3(H_r(i,j+1) + H_r(i,j)) - 2\beta(j+\tfrac{1}{2})(Z_o \Delta\xi J_z + P_{cc}(Z_o\sigma, E_z, m)) \tag{4.41}$$

A precisely analogous procedure is applied to Eq. (4.30c), beginning with a formal integration:

$$E_\theta(i+1,\, j+\tfrac{1}{2}) = \alpha E_\theta(i, j+\tfrac{1}{2}) - \frac{(1-\alpha)}{Z_o \sigma_o}\left[\frac{\partial H_r}{\partial z} + \frac{\partial H_z}{\partial r} + P_{cs}(Z_o \sigma, E_\theta, m)\right] \tag{4.42}$$

We finally obtain from (4.42) and equation of a form analogous to (4.38), involving H_r, E_θ, and H_z.

Equations (4.31) and (4.34) are used to eliminate E_z and H_z from (4.36) - (4.39), generating in principle an incomplete set of $4(N_R-1)$ equations in the $4N_R$ unknown fields $E_{rm}(i+1,j)$, $E_{\theta m}(i+1,j)$, $H_{rm}(i+1,j)$, and $H_{\theta m}(i+1,j)$. Two outer boundary conditions and two inner boundary conditions are required to complete the set of equations and make it soluble.

Simple conducting-boundary conditions are always imposed at the outer wall at $r_{NR} = R_{max}$, namely

$$E_\xi(R_{max}) = 0$$
$$H_r(R_{max}) = 0 \qquad (4.43)$$

At the inner boundary, several sets of boundary conditions have been tried. A satisfactory set appears to be

$$E_\xi - E_r = 0$$
$$H_\xi + H_r = 0$$
$$E_z = 0 \qquad (4.44)$$
$$H_z = 0$$

with the latter two equations replacing "c" and "f". As an alternative procedure, a more complicated procedure can be followed at the inner boundary, $r_1 = 0$. Because of the 1/r-factors in Eqs. (4.30c) and (4.30f), it is necessary to look more closely at the behavior of the fields as r approaches zero. We find that, near r = 0, $E_{zm} \sim r^m$, $H_{zm} \sim r^m$; and the transverse fields E_{rm}, $E_{\xi m}$, H_{rm}, and $H_{\xi m}$ all vary as r^{m-1}. Within the first radial grid cell, we thus assume

$$E_{zm}(r,\xi) = r^m e_{zm}(r,\xi)$$
$$E_{rm}(r,\xi) = r^{m-1} e_{rm}(r,\xi) \qquad (4.45)$$

and so on, for the remaining field quantities. We find that, at r = 0, the field equations (4 30c) and (4.30f) are replaced by equivalent relations between the e's and h's:

$$\frac{\partial e_z}{\partial \xi} - m e_z = - \frac{\partial h_r}{\partial \xi} \tag{4.46}$$

$$\frac{\partial e_r}{\partial \xi} + Z_o \sigma_o e_r = \frac{\partial h_z}{\partial \xi} + m h_z - Z_o j_r \tag{4.47}$$

and that the remaining field equations yield the two independent boundary conditions

$$\begin{aligned} e_z + e_r &= 0 \\ h_z + h_r &= 0 \end{aligned} \tag{4.48}$$

The remaining equations (4.30a, b, d, and e) are written for the interval $r_1 \leq r \leq r_2$ in terms of the e's and h's, but are otherwise expressed in finite-difference form with the handling and centering described above for the "usual" situation of the differencing cells between r_2 and R_{max}. We thus obtain a set of $4N_R$ equations for the $4(N_R-1)$ fields at rr = r_2, r_3, ... r_{NR} and e_r, e_θ, h_r, and h_θ defined at r_1. The axial fields E_z, H_z, e_z, and h_z are found by back-substitution in Eqs. (4.31), (4.34), and their analogues, obtained from Eq. (4.46) and (4.47), once the solution for the transverse fields is complete.

The MAHD2 calculational cycle is carried out exactly as the MAHD1 scheme discussed in connection with Fig. 4.1. Arrays used to determine the conduction current appearing in the various modes are assumed known (except, of course, for the $\sigma_o E_m$ contribution separated from the remainder) and updated as the sequential solutions for mode amplitudes proceed. The solution to the monopole-mode (m=0) equations simplifies to the usual axisymmetric field equation solution, and is carried out in a separate algorithm. The monopole solution is integrated into the iteration procedure, however; the contributions to the monopole conduction currents $\{\sigma E_r\}_o$ and $\{\sigma E_z\}_o$ are evaluated from the yet-to-be corrected higher-order mode fields, and solutions for $m \geq 1$ follow the monopole solution in the iterative cycle, as they do in the MAHD1 calculation.

4.2.3 Simplified Field Algorithm MAHD3

In order to extend the range of comparisons possible, a variation of MAHD2 was also constructed. The physical assumptions that led to the further simplifications of the frozen approximation used in the Lee potential formulation algorithm, MAHD1, amount, in field language, to neglect of the terms $\partial H_z/\partial \xi$ and $\partial E_z/\partial \xi$ that appear in Eqs. (4.30a) and (4.30d) above.

The finite difference equations solved in the MAHD3 algorithm were derived by modifying the Eqs. (4.30a) and (4.30d) as noted above. In programming terms, the modifications are quite small. The differenced form of Eq. (4.30a) shown in Eq. (4.36) is replaced by:

$$A_1 E_z(j+1) + A_2 E_z(j) + A_3(E_r(j+1) + E_r(j)) = rhs'_A \qquad (4.49)$$

Since H_z no longer occurs in the above equation, it is used directly in the equation set to be solved.

Equation (4.30d) is no longer formally integrated, and Eq. (4.39) is replaced by:

$$\left[\frac{1}{r}\frac{\partial}{\partial r}(rH_z) - \frac{m}{r}H_r - \sigma_0 E_z - \sigma_{cc}(E_z + E_{z_{ind}})\right]_{i+\frac{1}{2},j+\frac{1}{2}} \qquad (4.50)$$

Boundary conditions and the handling of the (r=0)-versions of Eq. (4.30c) and (4.30f) (shown in Eqs. (4.46) and (4.47), respectively) are identical to MAHD2.

4.3 Auxiliary Models and Methods

The algorithms discussed in Sec. 4.2 above are intended to interface in a reasonably tidy way with other portions of a complete hose dynamics model. The principal inputs to the field algorithm are thus quite simply the two-dimensional field source arrays of primary beam current density and conductivity that reflect the spatial (r,θ) variation of those quantities at the currently interesting ξ-step. Such field source arrays may be defined in any way that suits the physics of the desired model (e.g., analytic formulae, particle simulation results, or phenomenological models). The field sources are then passed on to the field-advancement scheme, which operates independently of the details of their origin. At present only simple analytic prescriptions for J_z and σ have been used to exercise the algorithms. Details of those prescriptions for a standard test problem will be considered in the following section.

4.4 Test Calculations and Comparisons

The algorithms described above were programmed in detail for actual machine execution. Since intercomparison of the algorithms (vis a vis their accuracy, speed, the effects of further simplification of the frozen approximation, and differences between field- and potential- formulations of the e.m. equations) was of most interest, a simple prescribed model of beam current and conductivity was used in exercising the MAHD algorithms.

4.4.1 NRL Standard Nonlinear Test Problem

The beam model used in the test calculations was a prescription developed by F. Chambers of LLNL and G. Joyce of NRL as a standard test problem for nonlinear field algorithms. The beam current density distribution is assumed to have a Bennett profile characterized by a ξ-independent Bennett radius parameter, r_B. The total primary beam current $I_b(\xi)$ is given by the analytic form

$$I_b(\xi) = I_{b\text{-}pk} \tanh\left(\frac{\xi}{\xi_r}\right) \tag{4.51}$$

characterized by the peak-current parameter I_{b-pk} and risetime parameter $\xi_r = c\tau_r$. The beam displacement is modeled as a Gaussian "kink" of width ξ_w and centered at ξ_o; the peak displacement is X_o.

$$X(\xi) = X_o \exp\left[-(\xi-\xi_o)^2/\xi_w^2\right] \tag{4.52}$$

The conductivity is characterized by an initial ambient background conductivity σ_{bkg}, and a rate of increase directly proportional to the local primary beam current density:

$$\frac{d\sigma}{d\xi} = \alpha_\sigma J_z(r,\theta,\xi) \tag{4.53}$$

Specific parameters for the Standard Test Case (STC) are summarized in Table 4-1.

4.4.2 Results of Calculations

The Standard Test Case (STC) problem was run for each of the three algorithms described above. Identical radial gridding schemes (60 gridpoints on an expanding mesh to R_{wall} = 10 cm) and timestep intervals ($\Delta\xi = 2\times10^{-11}$ sec) were used. Five radial modes (m = 0, 1, 2, 3, 4) were used, and three iterations per timestep (probably one more than necessary, see below) carried out. In calculations run to ξ = 1 nsec, typical elapsed CDC-7600 cpu times were between about 4 and 6 seconds, for all of the algorithms. The MAHD1 algorithm was also reprogrammed to take some advantage of the vectorization capabilities of the Cray-1. Calculations to ξ = 2 nsec with MAHD1 on a Cray-1 used a total of 3.2 sec, with about 1 sec used in the output routine. Of the time not consumed in output operations, most of the time was used in solving the 120-row band matrix (240-row for MAHD2 and MAHD3) representing the differenced equations for the unknown potentials/fields. The algorithms appear quite fast in

TABLE 4-1

SUMMARY OF STANDARD TEST CASE PARAMETERS

Beam Current

I_{b-pk} = 10,000 amperes
τ_r = 1 nsec
($\xi r \approx$ 30 cm)

Beam Current Density

r_B = 1 cm

Beam Displacement

X_o = 1 cm
τ_o = 1 nsec
($\xi_o \approx$ 30 cm)
τ_w = .25 nsec
($\xi_w \approx$ 7.5 cm)

Conductivity

$\sigma_{bkg} = 1.113 \times 10^{-2}$ mho/m (10^8 sec^{-1})
α_σ = 350 mho/amp

---

comparison with the time (over two minutes) required for the same problem, using the full-mode-set-inversion approach.

Elapsed time for the MAHD algorithms should scale with the product of separate linear dependence with time and space grid size, number of modes, and number of iterations. In the STC problem, differences between 1 and 2 iterations led typically to differences of about .5% in the calculational results at ξ = 1 nsec; differences between 2 and 3 iterations were less than .05%.

Detailed comparison of the results of the three calculations showed nearly identical field profiles for MAHD1 and MAHD3. Individual field values compared to better than 2% everywhere, with comparison to better than .5% for most fields and locations. This agreement is encouraging from a programming standpoint, since the MAHD1 and MAHD3 algorithms, although containing the same (or equivalent) physical assumptions, are quite different in analytic and programming details. Comparisons with a few data points available from DYNASTY results for the STC, as quoted in Ref. 15 , are also encouraging. The results concern field/potential profiles along the beam-displacement (X-)axis at ξ = 1 nsec, the time of maximum beam displacement in the STC (see Table 4-1). Values at r = 0 and maximum/minimum values along the outgoing radius at θ = 0 are tabulated for comparison in Table 4-2. Differences, which are not large, may probably be attributed to differences in time- and space-gridding and details of the source (current and conductivity) algorithms in DYNASTY and the MAHD codes. More detailed comparisons with the DYNASTY-like field solver in the DYNADISC code are anticipated.

Detailed MAHD2/MAHD3 comparisons are shown in Figs. 4.2 through 4.6. The figures show STC results at ξ = .5 nsec and ξ = 1 nsec for E_r- and H_θ-fields. Monopole and dipole modes are plotted separately, together with the "cumulative" values representing actual radial profiles along the direction of beam displacement, θ = 0.

Radial E-fields are compared in Fig. 4.2 at ξ = 0.5 nsec. The monopole fields are essentially identical from MAHD2 and MAHD3, but differences in the dipole modes are fairly large and significant inside the beam. A similar comparison at ξ = 1 nsec is shown in Figs. 4.3 and 4.4. Sizeable

TABLE 4-2

COMPARISONS WITH STC*

	NRL		MAHD1 (A,σ;Lee)	MAHD3 (E,H;Lee)	MAHD2 (E,H;full)
$E_z(0)$	-6.23 (5)	v/m	-6.57 (5)	-6.58 (5)	-6.07 (5)
$E_z(max)$	-2.73 (6)		-2.60 (6)	-2.60 (6)	-3.00 (6)
$E_r(min)$	-5.67 (5)		-4.69 (5)	-4.75 (5)	-8.01 (5)
$E_r(max)$	+2.91 (6)		+3.05 (6)	+2.97 (6)	+3.31 (6)
$J_B(0)$	6.04 (6)	a/m^2	6.05 (6)		
$J_B(max)$	2.39 (7)		2.26 (7)		
$Z_o\sigma(0)$	1365	m^{-1}	1359		
$Z_o\sigma(max)$	1471		1460		

*Freeman & Wagner, SAND84-1785 (RMKS units)

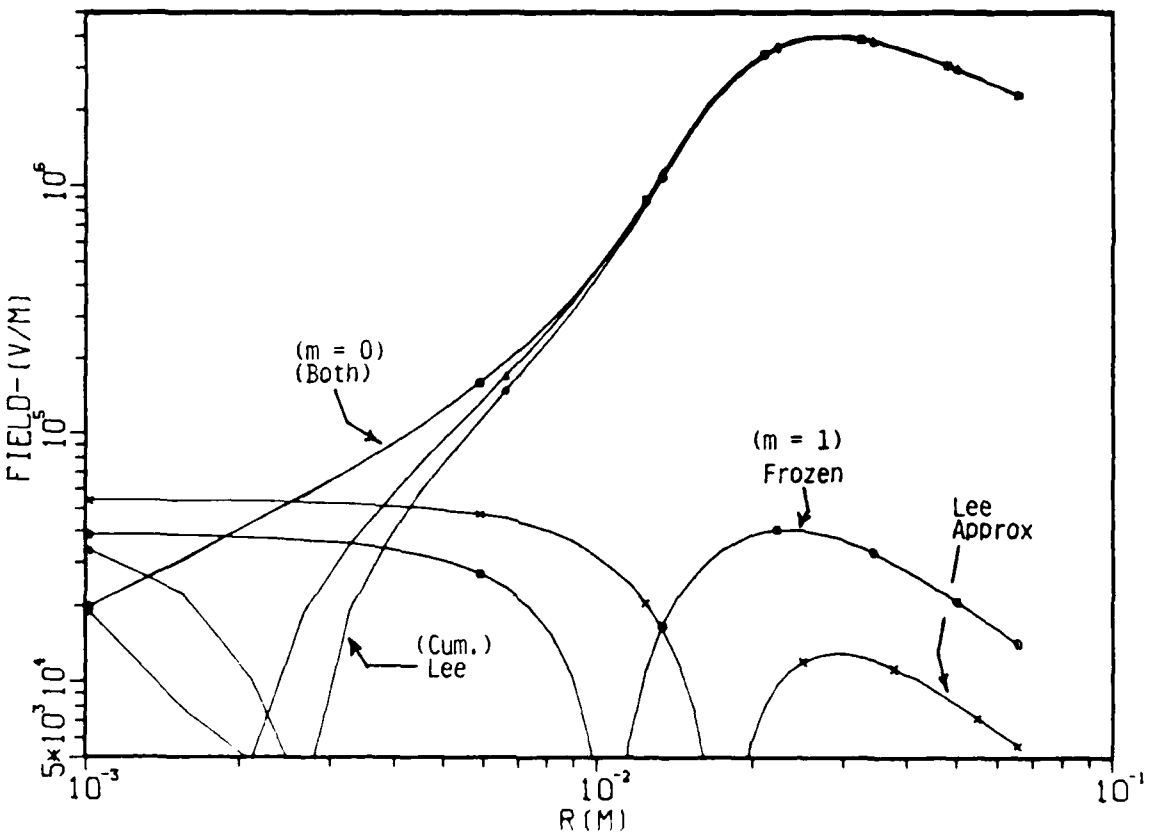

Figure 4.2. STC E_r profiles at ξ = .5 nsec. The m=0 fields for both frozen and Lee approximation are almost identical. Differences in the m=1 modes do affect the cumulative-field comparison inside the beam, however.

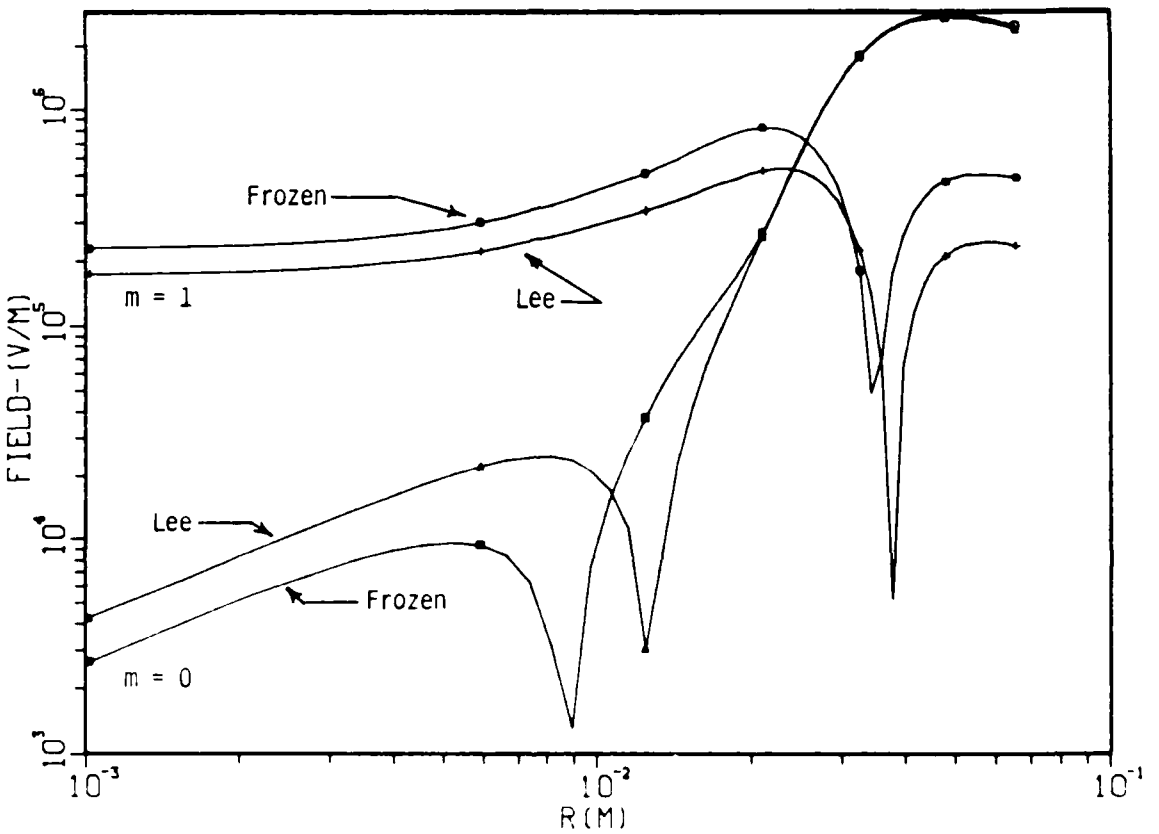

Figure 4.3. Comparison of monopole and dipole amplitudes. E_r amplitudes vs. radius at ξ = 1 nsec.

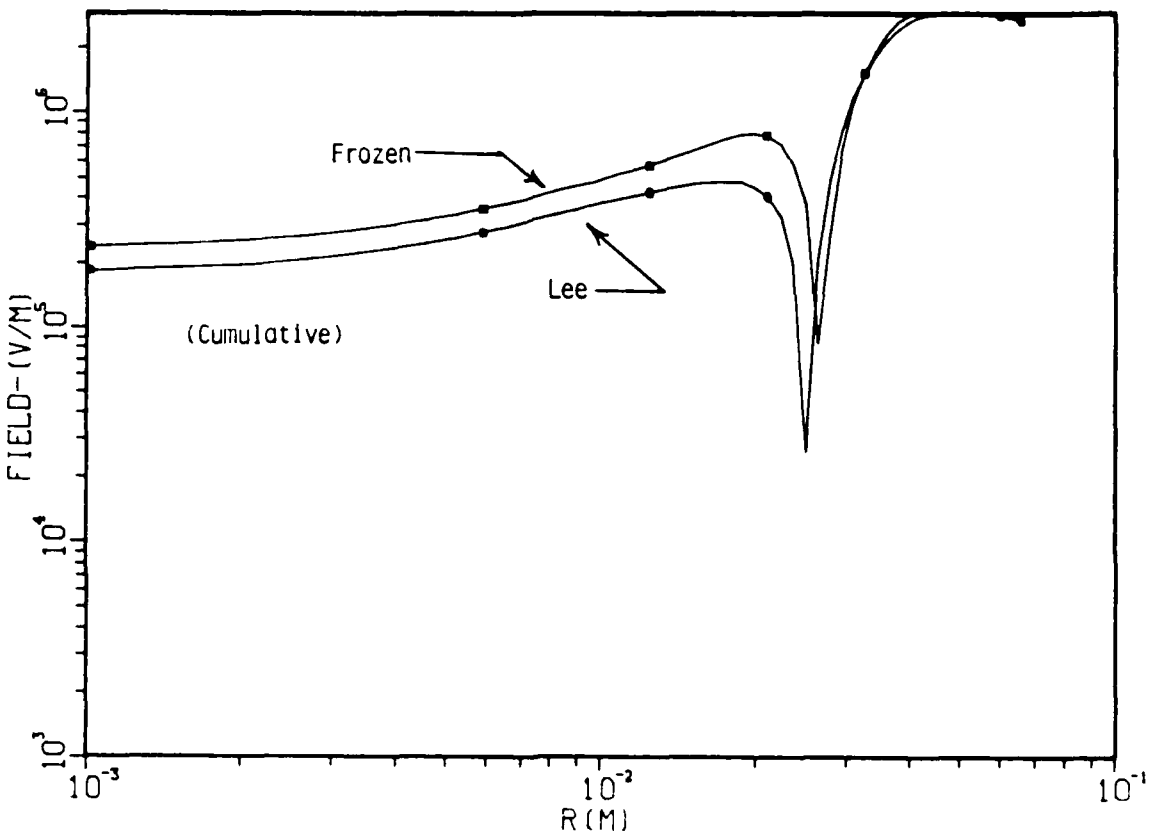

Figure 4.4. Comparison of cumulative fields (θ=0) at t = 1 nsec. (Monopole and dipole components were compared in Fig. 4.3.)

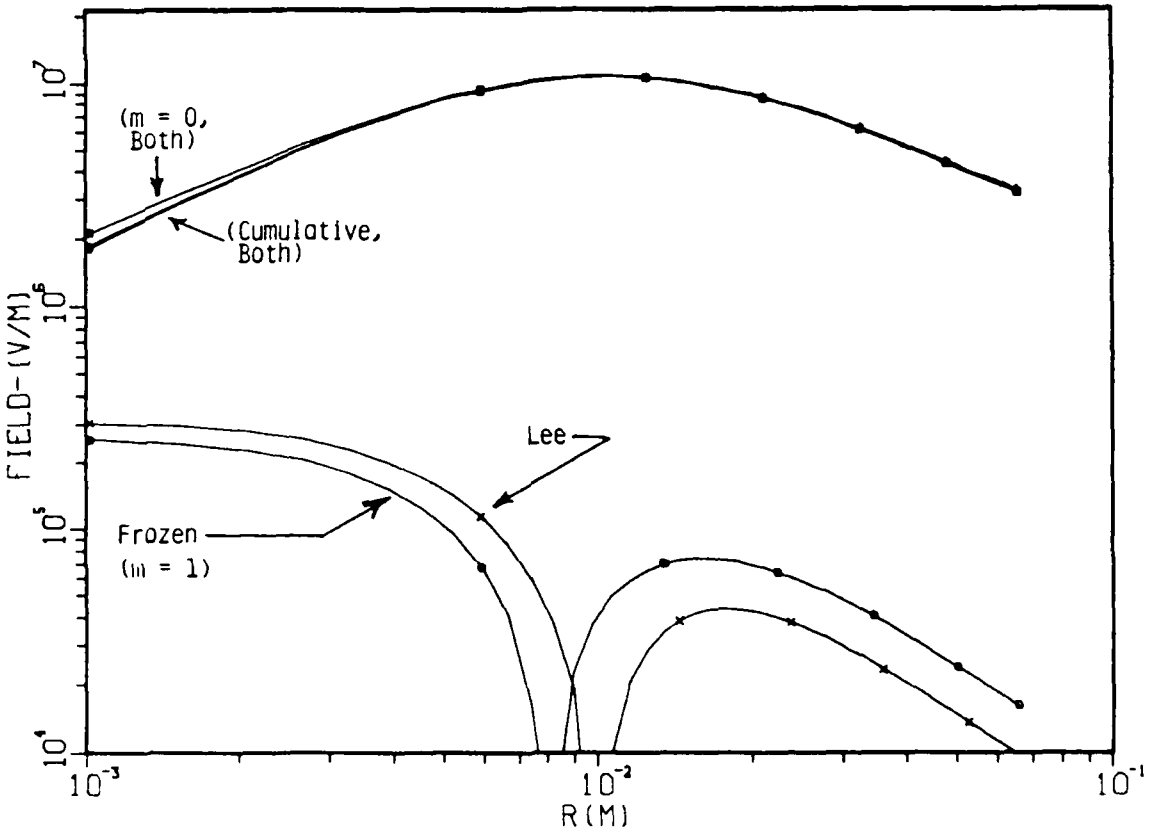

Figure 4.5. STC H_ϕ-profile at ξ = .5 nsec. Monopole components dominate the fields, and differences in the m=1 fields have little effect on the cumulative profiles.

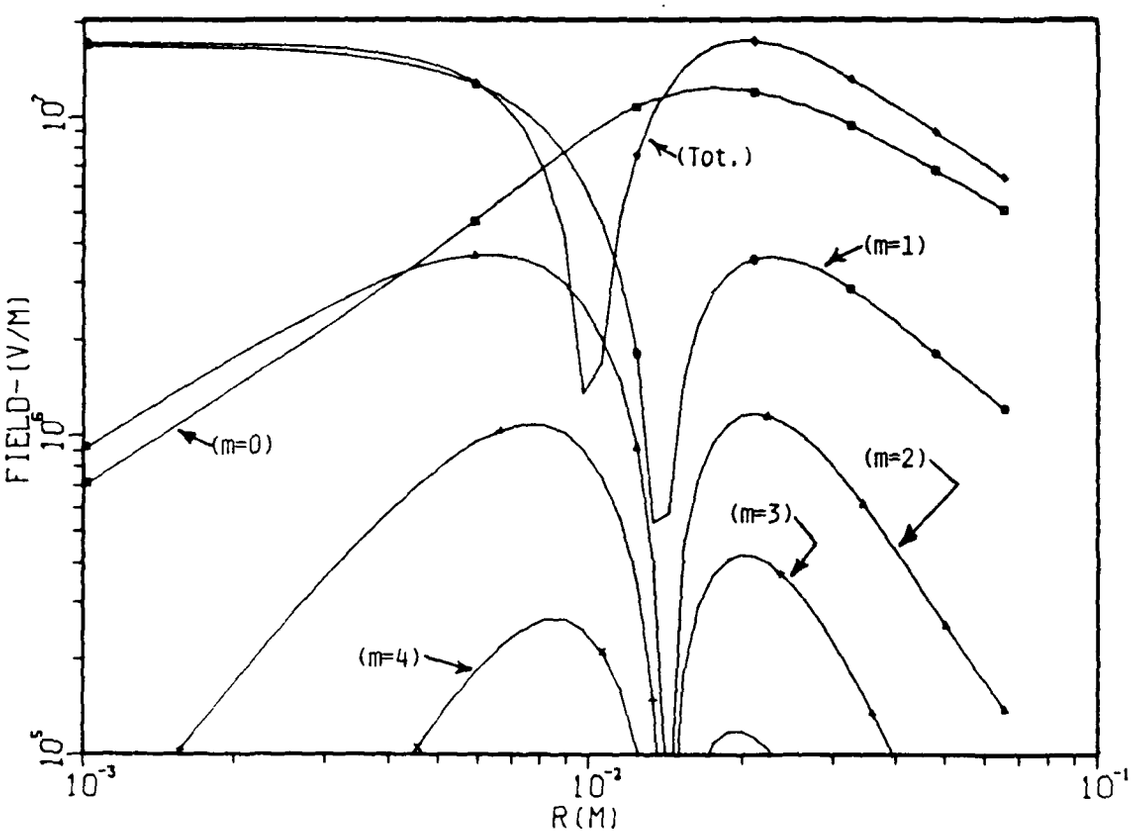

Figure 4.6. Contributions to H_ϕ at ξ = 1 nsec. The frozen-field and Lee approximations give essentially identical results here; separate and cumulative contributions to radial profiles are shown for the frozen-field algorithm.

differences appear there, both in the monopole and dipole modes, and therefore again in the cumulative fields (plotted separately for clarity in Fig. 4.4) as well. Outside of the beam (here, beyond about 2 cm), the fields again are similar.

Comparisons for the magnetic fields are typically closer. Figure 4.5 shows H_θ-profiles for the STC at ξ = .5 nsec. The relatively small differences in the dipole-mode fields do not significantly affect the cumulative fields. At ξ = 1 nsec, there is essentially no difference between the MAHD2 and MAHD3 results; only the results for MAHD2 are shown in Fig. 4.6, which shows the relative amplitude for all five modes carried, as well as the summed profile.

Since the magnetic fields dominate the particle dynamics of the beam, the E-field differences shown in the calculational results may not be critical. On the other hand, breakdown effects in the beam (not modelled in the STC) may differ. Further, the higher-mode differences are more important for dynamics effects than the (m=0)-fields, so that further comparison calculations would be of interest.

4.5 Summary

Three alternative formulations of the nonlinear e.m. field solution were developed and programmed. Two formulations, one based on Lee's approximate potential equations, and another using an equivalent treatment explicitly considering e.m. fields, compared extremely closely with one another, and quite well with a few data points available from a DYNASTY calculation. The third calculation contained the unsimplified frozen-field assumption as a physical basis for the solution formulation. Moderate differences in the fields found with this model and with the previous two appear to exist. All of the models use iteration to find a satisfactory solution to the coupled-mode aspects of the problem; the iteration appears accurate and extremely fast.

5.0 REFERENCES

1. R.L. Feinstein, D.A. Keeley, H. Kirch, and E. Simpson, "Propagation Physics of High Current Beams", SAI-C-42-PA, 23 October 1980 (SECRET).

2. M. Lampe, W. Sharp, R.F. Hubbard, E.P. Lee, and R.J. Briggs, Phys. Fluids 27, 2921 (1984).

3. R.K. Landshoff, Phys. Review 76, 904 (1949).

4. D.A. Keeley, "Beam Conductivity Code HICHEM,", SAI-C-49-PA, 30 June 1981 (CONFIDENTIAL).

5. R.R. Johnston, R.L. Feinstein, D.E. Maxwell, E.R. Parkinson, and E.E. Simpson, "Topics in the Respose of a Gas to Charged Particle Beams, II", SAI-C-10-PA, 15 January 1978 (SECRET).

6. R.R. Johnston, R.L. Feinstein, and D.A. Keeley, "Theoretical Studies in Charged Particle Beam Propagation", SAI-C-51-PA, 31 December 1981 (SECRET).

7. R.R. Johnston, R.L. Feinstein, D.A. Keeley, C.L. Yee, B.B. Godfrey, L. Wright, D. Mitrovich, and T.P. Hughes, "Studies in Charged Particle Beam Propagation", SAIC-C-73-PA, 31 January 1985 (SECRET).

8. D.A. Keeley and R.L. Feinstein, "Consequences of Non-Ohmic Currents and Non-Local Energy Deposition for Electron Beam Propagation in Reduced-Density Air", presented at the Fifth International Conference on High-Power Particle Beams in San Francisco, CA, 12-14 September 1983 (UNCLASSIFIED).

9. D.A. Keeley and C.L. Yee, "Low-Density Conductivity Models", presented at the DARPA/Services Propagation Review Meeting in Monterey, CA, 20-23 June 1983 (UNCLASSIFIED).

10. S.S. Yu and R.E. Melendez (LLNL), "Dynamics of Electron-Beam-Generated Plasma ... 100 Torr", presented at the APS Meeting, New Orleans, LA, 5 November 1982 (UNCLASSIFIED).

11. R.R. Johnston and E.E. Simpson, "Studies in Beam Propagation Physics", SAI-C-38-PA, 9 August 1980 (SECRET).

12. R.S. Briggs and S.S. Yu (LLNL), "Modeling Beam Front Dynamics at Low Gas Pressures", 13 May 1982 (UNCLASSIFIED).

13. R.L. Feinstein, D.A. Keeley, E. Cornet and W. Rienstra, "High Current Beam Propagation Studies: Theory and Experiment", SAI-C-56-PA, February 1983 (UNCLASSIFIED).

14. B. Hui and M. Lample, "DYNASTY II, A Nonlinear Implicit Code for Relativistic Electron Beam Tracking Studies", NRL Memorandum Report 5138 (July 1983).

15. J.R. Freeman and J.S. Wagner, "Field Solver Comparisons Between the 3-D Non-Linear Electron Beam Propagation Code DYNADISC and the Linearized Code (OOSIK)", SAND84-1785 (November 1984).

16. E.P. Lee, "The New Field Equations", UCID-17286, October 1976.

END

DTIC

8-86